THEORY OF NEAR INFRA-RED GERMANIUM LASERS

OSAMAH ABDULRAHMAN N ALDAGHRI

Submitted in accordance with the requirements for the degree of

Doctor of Philosophy

The University of Leeds

School of Electronic and Electrical Engineering

June 2014

The candidate confirms that the work submitted is his/her own, except where work which has formed part of jointly authored publications has been included. The contribution of the candidate and the other authors to this work has been explicitly indicated below. The candidate confirms that appropriate credit has been given within the thesis where reference has been made to the work of others.

The work in Chapter 3 of the thesis has appeared in publications as follows:

1. O. Aldaghri, Z. Ikonić, R. W. Kelsall; ''*The effects of tensile-strain conditions on doping density requirements for Ge-based injection lasers*'', P1.32, 151-153, The 8th IEEE International Conference on Group IV Photonics, London, 2011.
2. O. Aldaghri, Z Ikonić and R W Kelsall; ''*Optimum strain configurations for carrier injection in near infrared Ge lasers*'', J. Appl. Phys. 111(5), 053106, 2012.

In both works, I wrote the original text and produced the results. Co-authors are responsible for the result discussion and revision and finalized the text.

To my parents
Abdulrahman and Aljawharah,
to my wife Huda and to my kids Shahd and Abdulrahman.

ACKNOWLEDGMENTS

First and foremost, I praise Allah the Almighty the Merciful for his blessings and guidance throughout my PhD journey and my life. No words of gratitude are sufficient to acknowledge his favour on me.

I would like to acknowledge and thank my supervisors, Prof. Robert W. Kelsall and Dr. Zoran Ikonić for their support, input and guidance during my doctoral studies.

Special appreciation to Dr. Leon Lever for the discussion, answering my questions and for his numerous help in the beginning of my PhD study.

I am grateful to Prof. Robert W. Kelsall and Dr. Zoran Ikonić for their exceptional work of reading this thesis and offering their valuable comments. I am also thankful to my colleagues: Miss Helen Rafferty, Mr. Andrew Grier and Mr. Andrew Sills for proof reading this thesis.

I would like also to acknowledge the fellow colleagues and researchers at IMP: Dr. Leon Lever, Dr. Neil Pilgrim, Dr. Pavlo Ivanov, Dr. Viet Than Dinh, Dr. Alex Valavanis, Dr. Raed Alhathlool, Dr. Sami Aldalahmeh, Dr. Jonny Cooper, Mr. N Prodanovic, Dr. Roney Thomas, Miss Helen Rafferty, Mr. Andrew Grier and Mr. Andrew Sills. Many thanks to Miss Louise Redmonds and Mrs. Susan Hobson for their administrative support.

During my studies I was lucky to attend UK Silicon Photonics Project meetings and to witness the strategic planning, discussion and collaboration at very high level between different research groups to improve different aspects of optoelectronic devices.

For financial support throughout the course of my studies, I would like to acknowledge my Scholarship sponsor, Al Imam University (Riyadh, Saudi Arabia). Thanks are due also to the Royal Embassy of Saudi Arabia and the Saudi Cultural Bureau in London for their supportive scholarship administration.

I shall always be indebted to both Prof. Robert W. Kelsall and Dr. Zoran Ikonić for the motivation, enthusiasm and the unconditional support they provided which I will not forget.

On a personal note, I would like to express my gratitude to my father Dr. Abdulrahman and my mother Aljawharah for their love, endless support and moral encouragement. My brothers, sisters, my father and mother in law deserve my wholehearted thanks as well. I'm forever grateful to my small family: my wife Huda and my kids Shahd and Abdulrahman for coping with me and for all of the sacrifices that you have made on my behalf, their presence has been the keystone of my work.

ABSTRACT

Due to major advances in silicon photonics technology and the importance of having a silicon-compatible laser operating in the 1.3 - 1.55 micron communications wavelength window. There is currently an intense interest in the optical properties of germanium, which has a direct band gap transition in this wavelength range. The Ge band structure can be engineered using biaxial or uniaxial strain in order to achieve optical gain. Recently, both optically pumped and electrical injection pumped lasing have been reported in Ge-on-Si devices. This work aims to perform gain modeling in a germanium laser grown on a silicon substrate which operates in the near infrared wavelength communications band.

A description of the background theory of the variation of the relevant electronic band structure properties of Ge with the applied strain is given. Shifts of the conduction and valence band edges with strain (biaxial and uniaxial) applied to Ge grown on substrates of different orientations has been investigated using the linear deformation potential and $\mathbf{k}.\mathbf{p}$ methods.

In order to make Ge behave as a direct band gap material, and to have a good electron injection efficiency, an investigation of the combination of the applied strain and doping density on direct band gap and injected carrier efficiency were carried out at 0 K, for both bulk Ge and Ge quantum wells.

At finite temperatures, the $\mathbf{k}.\mathbf{p}$ method and effective mass approximation were used to calculate the energy bands for [001] bulk Ge, the quasi-Fermi levels for given values of carrier densities, and then the interband gain and IVBA were calculated for biaxially tensile strained [001] bulk Ge. Furthermore, a detailed description of the free carrier absorption coefficient calcu-

lation, accounting for both intervalley and intravalley scattering in strained [001] Ge is given. The effect of unequal electron and hole densities, which are required to achieve the interband gain and reduce the absorption coefficient due to IVBA and FCA in order to obtain the net gain, has been investigated for strained bulk n^+ Ge at room and typical device temperatures.

LIST OF PUBLICATIONS AND CONFERENCES:

1. Osamah Aldaghri, Zoran Ikonić, and Robert W. Kelsall; ''*Effects of various tensile-strain conditions on doping density requirements for Ge-based injection lasers*'', UK Semiconductors conference, 2011.
2. O. Aldaghri, Z. Ikonić, R. W. Kelsall; ''*The effects of tensile-strain conditions on doping density requirements for Ge-based injection lasers*'', P1.32, 151-153, The 8th IEEE International Conference on Group IV Photonics, London, 2011.
3. O. Aldaghri, Z. Ikonić and R. W. Kelsall; ''*Electronic structure and optoelectronic properties of strained Ge nanowires with different orientations*'', Institute of Physics Photon 12 Conference, Durham, 2012.
4. O. Aldaghri, Z Ikonić and R W Kelsall; ''*Optimum strain configurations for carrier injection in near infrared Ge lasers*'', J. Appl. Phys. 111(5), 053106, 2012.
5. O. Aldaghri, Z. Ikonić and R. W. Kelsall; ''*Temperature and carrier density dependent gain and inter-valence band absorption in strained bulk Ge*'', UK Semiconductors Conference, Sheffield, 2013.
6. O. Aldaghri, Z. Ikonic and R. W. Kelsall; ''*Numerical investigation of optical gain in tensile strained germanium layers for near infra-red lasers*'', The NUSOD 14th International Conference, Spain, 2014.
7. O. Aldaghri, Z. Ikonic and R. W. Kelsall; "*Optical gain calculation in tensile-strained n-doped Ge*", E-MRS 2014 FALL MEETING Poland, 2014.

CONTENTS

LIST OF FIGURES

LIST OF TABLES

ACRONYMS

CVD	chemical vapour deposition
LEDs	light emitting diodes
CW	continuous wavelength
MBE	molecular beam epitaxy
UHV	ultra high vacuum
LP	low pressure
PL	photoluminescence
EL	electroluminescence
CMP	chemical-mechanical polishing
C.B.	conduction band
V.B.	valence band
HH	heavy hole
LH	light hole
SO	spin-orbit split-off
IVBA	intervalence band absorption
FCA	free carrier absorption
BZ	Brillouin zone
B	biaxial strain
U	Uniaxial strain
FWHM	Full-width at half-maximum

LIST OF SYMBOLS

$c = 3.00 \times 10^{8}\mathrm{m/s}$	Speed of light in vacuum
$e = 1.60 \times 10^{-19}\mathrm{C}$	Elementary charge
$\varepsilon_0 = 8.85 \times 10^{-12}\mathrm{F/m}$	Vacuum permittivity
$\hbar = 1.05 \times 10^{-34}\mathrm{Js}$	Reduced Planck constant
$k_B = 1.38 \times 10^{-23}\mathrm{J/K}$	Boltzmann constant
$m_0 = 9.11 \times 10^{-31}\mathrm{kg}$	Rest mass of free electron
a_l	Lattice constant
Ξ_d,Ξ_u	Conduction band deformation potentials (dilation, shear)
$C_{\alpha\beta}$	Elastic constant
Δ	Spin-orbit splitting
$E^{\mathrm{c,k}_i}$	Conduction bad energy of k_i valley
E^{v}	Valence band energy
E^{g}	Bandgap energy
E	Energy
ΔE^{k_i}	k_i valley energy shift
E_F,$E_{Fc/v}$	Fermi level and quasi Fermi level for C.B. and V.B.
k, k_α, q	Wavevector
$\mathcal{H}$	Hamiltonian with spin-orbit interaction
$\mathcal{H}_s$	Strain-dependant Hamiltonian
a,b,d	deformation potential constants
$\epsilon_{\alpha\beta}$	deformation coefficients

$\sigma_{\alpha\beta}$	Stress component
ε,$\varepsilon_{\alpha\beta}$	Strain tensor and components
$\boldsymbol{a}_{\mathrm{k}_i}$	Unit vector
U	Coordinate transformation matrix $R \rightarrow R'$
m_ℓ, m_t	Effective mass along longitudinal/transverse axis of valley
n^{k}_{3D}, n^{k}_{2D}	Bulk and quantum well electron density in valley
N_{3D}, N_{2D}	The electron density for bulk and quantum well
$\sigma^{\Gamma}_{\text{bulk, q.w}}$	Injection efficiency for bulk/quantum well
f_{state}	Fermi-Dirac occupation probability for that state
ψ	Wavefunction
t	Time
ω_t, ω_q	photon and phonon angular frequency
n, p	Total electron and hole density
n_{inj}, p_{inj}	injected electron and hole density
$W_{ij,}W_{ij\rightarrow fg}$	Scattering rate
L	Lorentzian Half-width at half maximum (linewidth)
z	Position normal to interfaces
T_L, T_c	Lattice and carrier temperature
λ	Wavelength
n_r	Refractive index
N_q	Bose-Einstein phonon distribution function
α , g	Absorption, Gain coefficient
v_s	Speed of sound
$\left\|M_q\right\|^2$	Carrier-phonon interaction
D_{if}	intervalley deformation potential
D_{opt},D_A	Optical and acoustic phonon deformation potential

1

INTRODUCTION

Silicon and germanium are indirect band gap semiconductor materials. For indirect band gap materials, it is not possible to have a light transition without a photon-assisted process, due to the difference in momentum between the electron in conduction band and holes in the valence band, which gives rise to inefficient radiative recombination from the indirect valleys, fig. (1.1). However, the direct band transition in Ge, which is possible, has an important feature because the emitted light has a wavelength within the 1550 nm communications band at room temperature [25]. Also, the direct band transition in Ge has a fast recombination rate as efficient as in III-V semiconductor materials, and Ge is thus expected to be the primary candidate for laser operation, fully compatible with Si technology [26]. The Ge (or SiGe alloy) layers maybe grown epitaxially on a Si substrate to make photonic devices [27, 28]. The III-V semiconductors laser on Si, which has been demonstrated, has has its limitation for technical growth issues, the large-scale electronic–photonic integration and system temperature [29]. The CMOS integration of III-V on Si is difficult due to a thick buffer layer is required to epitaxial grow III-V semiconductors on Si. Also the chip bounding method to integrate III-V lasers on Si is another issue due to the small III-V wafer diameter comparing to the Si wafers that used in CMOS electronics [29].

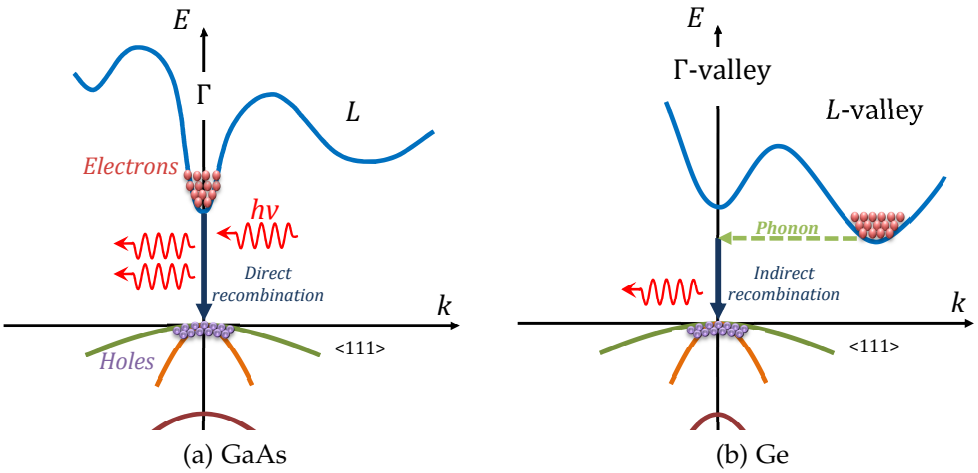

Figure 1.1: Schematic of electron-hole recombination in the electronic band structure for (a) GaAs as direct band gap, and (b) Ge as indirect band gap semiconductor materials, after Refs. [1, 2, 3].

1.1 SILICON PHOTONICS

The term photonics covers the phenomena and applications in which photons are used to transmit or process information. This includes fibre optics, optical data storage, optical sensors, photon emitters and receivers. The light wavelengths involved normally belong to the range between near ultraviolet and near the infrared part of the spectrum. Silicon photonics tends to combine the photonics concepts with silicon technology. Silicon is the dominant material for semiconductor electronics and has become the preferred material for photonics, because of its high thermal conductivity, abundance, availability of a good oxide and low cost compared to other semiconductor materials [30]. The possibility of integrating electronic and optical components on the same silicon chip is the principal advantage of Si photonics. Si-based modulators and photodetectors have undergone substantial development in recent years, see refs. [31, 32, 33, 34]. At room temperature, a monolithically integrated continuous wavelength (CW) III-V (GaAs/AlGaAs) quantum well laser on a Si substrate has been demonstrated, where the Si substrate was grown on relaxed graded GeSi buffer

layers [29]. Fang *et.al.* also demonstrated an electrically pumped hybrid III-V laser on a silicon substrate [35].

1.2 SI-BASED LASER

A Si-based laser is the missing part in electronic-photonic integrated circuits, considering the domination of Si in the semiconductor industry. Such devices would have a smaller fabrication cost than III-V lasers on a Si substrate, due to the possibility of monolithic integration [8, 36].

High stacking density of Si nanocrystals embedded in a layer of SiO_2 to obtain light amplification has been demonstrated [37]. Further optimization of highly luminescent light emitting diodes (LEDs) fabricated from Si nanocrystals embedded in SiO_2 has been modelled and photoluminescence (PL) measurements has been demonstrated [38].

A gain medium of a Si waveguide was used to demonstrated a pulsed Si Raman laser at 1675 nm, and this is the first Si laser [39, 40]. The pulsed pumping overcame two photon absorption, which is the main loss due to the free carrier accumulation in the case of CW pumping if used [41].

1.3 TECHNIQUES OF GROWING GE AND SIGE ON SI

The word "Epitaxy" means organized crystal growth. The two mostly used technologies for growing a new crystal of one material epitaxially on a Si substrate to make layers or films for a semiconductor device are molecular beam epitaxy (MBE), which was originally used to grow epitaxial SiGe layers, and chemical vapour deposition (CVD) [30]. In the MBE technique, crystal growth on the surface of a Si substrate proceeds from the interaction of molecular or atomic beams that comes from evaporation effusion

cells which contain the solid source materials. The (Si) substrate is heated to the required temperature and rotated continuously to achieve homogeneous growth in an ultra high vacuum (UHV) environment. Using this technique gives very thin layers with precise compositions at low temperatures ($600 - 800\,^{\circ}\mathrm{C}$), but with low growth rates. On the other hand, CVD needs high temperatures ($1000\,^{\circ}\mathrm{C}$), which is a disadvantage, but the growth rate is high, with easier composition control. UHV CVD and low pressure (LP) CVD have been developed to reduce the growth temperature in CVD, with pressures of around 10 Pa and from 10 to 100 Pa, respectively [30, 42]. The low-energy plasma-enhanced CVD were used as an epitaxial growth of $Ge/Si_{0.15}Ge_{0.85}$ multiple quantum wells on (111) Si substrates, to obtain moderate threading dislocation density comparing to Ge-rich heterostructures grown on (001) Si through a much thicker graded virtual substrate [43].

1.4 EFFECTS OF DIFFERENT STRAIN CONDITIONS ON THE GE DIRECT TRANSITION

The applied biaxial tensile strain on semiconductor material moves the conduction band (C.B.) minima at Γ and L points downward with respect to the vacuum level [44], and this reduction can be calculated using deformation potential theory [45]. Furthermore, under tensile strain the valence band (V.B.) top splits into heavy hole (HH) and light hole (LH) bands [26] and the $\mathbf{k}.\mathbf{p}$ method is used to calculate the top of the valence band [19, 46]. It has been proved theoretically (using deformation potential and 6×6 $\mathbf{k}.\mathbf{p}$ methods) and experimentally that the direct PL of (100) Ge under biaxial tensile strain is enhanced due to the reduction in energy difference between the Γ and indirect (L) valleys, and the enhancement factor is 1.8 for 0.37 % biaxial tensile strain [47]. Fischetti *et.al.* presented theoretical work in 1996

on strained Ge which shows that [001] Ge becomes a direct band gap material with about 1.75 % biaxial tensile strain [48]. El Kurdi *et. al.* used a 30 band **k**.**p** method to calculate the band structure which shows that Ge becomes a direct bandgap semiconductor with around 1.9 % tensile strain and the bandgap shrinks to 530 meV [49]. On a tensile strained nanomembranes, PL of Ge the direct band gap was observed for different values of applied strain values [50].

Experimentally, biaxial and uniaxial strains enhance the carrier mobility in bulk MOSFETs grown in different orientations owing to highly altered band structures [51]. Selective ion implantation was used to introduce uniaxial strain in various Si/Ge heterostructures [52]. Yu *et.al.* used four-point bending structures to achieve uniaxial tensile and compressive strain in the <110> direction in a Ge p-i-n photodiode integrated on Si, which showed an increase of the responsivity at the direct bandgap with the tensile strain, toward longer wavelengths, and a decrease with the compressive strain, towards shorter wavelengths [53] . The fracture strengths of Si and Ge are large, for the crystalline <100> direction the maximum and uniaxial tensile strains and stresses are reported to be 20.6 % and 21.4 GPa in Si and 18.3 % and 14.7 GPa in Ge, respectively, [54]. While for corresponding <111> tensile strain the maximum values are 17 % at 22 GPa stress for Si and 20 % at 14 GPa stress for Ge [55]. Theoretical study predicted that a GeSn alloy can become a direct band gap material due to the lattice mismatch [56]. A top-down fabrication approach to obtain 3.1 % uniaxial tensile strain on Ge microbridges structure has been modelled and demonstrated [57].

A Silicon-Nitride (Si_3N_4) film stressor was deposited on a Ge wire to produce 0.4 % tensile strain [58]. With a 120 nm shift from bulk Ge, an enhanced room temperature luminescence using CW optical pumping source was exhibited. A biaxial tensile strain larger than 0.6 % was achieved using a thin (1μm) Ge membrane fabricated using Ge that is epitaxially grown on a Si substrate [59]. Up to 1.13 % biaxial tensile strain has been measured

using Raman spectroscopy, for an integrated thin layer Ge membrane on a Si substrate. A large enhancement in PL was observed with 100 meV reduction in the direct band gap [60]. Recently, even higher value of tensile strain has been demonstrated, about 1 and 1.5 % biaxial tensile strain on Ge microdisks using an all-around deposition Si_3N_4 stresser [61, 62].

1.5 DIRECT GAP EMISSION AND PHOTOLUMINESCENCE IN GE

Despite the indirect bandgap in Ge, the efficiency of the direct band transition can be increased using tensile strain and heavy doping [63]. Theoretically, with 0.25 % tensile-strained and an n^+ (phosphorous) doping density of $7.6 \times 10^{19}\,\mathrm{cm}^{-3}$, it has been predicted that Ge can achieve an efficient light emission with a significant net gain of $\sim 400\,\mathrm{cm}^{-1}$[8] and the PL is 50 times larger than in undoped strained Ge [64]. The probability of direct PL increases because the energy difference between the direct and indirect bandgaps reduces with tensile strain [44, 65]. In addition, with heavy n-type doping the Fermi level increases due to higher concentration of electrons , the excess electrons in the conduction band first fill the indirect L band and then fill the direct Γ band of Ge. With higher temperature, there is more possibility for electrons to thermally distribute in the Γ valley of the conduction band [26]. Due to the high free carrier absorption and the low internal quantum efficiency achieve an electrically pump laser is difficult [26].

Experiments have been performed to obtain direct PL from heavily doped strained Ge-on-Si using an optical pumping source to achieve population inversion and to investigate the net gain of strained Ge-on-Si [66, 67]. At room temperature, an optical pumping source has been used to study the photoluminescence of n^+-type in-plane biaxially 0.22 % tensile-strained epitaxial Ge-on-Si (in 110 growth direction), and the photoluminescence peak

was observed at 1590 nm. The direct PL of n-type tensile-strained Ge-on-Si increases with doping density (from 10^{17} to $10^{19}\,\mathrm{cm}^{-3}$), and with the temperature increase from 221 to 300 K; PL could not be observed under 200 K [26]. Lan *et. al.* have observed an enhancement of direct PL transition on n-type (100), (110), and p-type (111) Ge under 0.315 % biaxial tensile strain [68]. Experimentally, room temperature PL intensity (at $\sim$ 1590 nm) in n^+ bulk Ge and Ge-on-insulator increases with doping, using a gas immersion laser doping process, and a redshift is observed due to the impurities. The direct transition in low-resistivity Ge is stronger than in high-resistivity Ge due to increase of the electron concentration in the Γ-valley with respect to the L-valleys [69]. The direct and indirect photoluminescence increases with laser pumping power, but only the direct PL was enhanced at elevated temperature (and near room temperature) in a [100] Ge n^+-p junction [70]. On InGaAs/GaAs buffer layers, MBE was used to grow biaxially tensile-strained Ge layers up to 2.3 %, which showed a dramatic increase in direct PL but at much larger λ for tensile strain greater than 2 % at low-temperature [71].

El Kurdi *et. al.* reported that for 3 % tensile-strained Ge the optical gain increases with the injected carrier density ($4 \times 10^{18}\,\mathrm{cm}^{-3}$) up to $3000\,\mathrm{cm}^{-1}$ at low-temperatures (4 and 80 K). The experiments showed that the PL of Ge on insulator was enhanced by factor of 20 with heavy electron doping ($4 \times 10^{19}\,\mathrm{cm}^{-3}$) at room temperature [49]. Recent study of the PL of direct gap gain of optically pumped Ge-on-Si shows that the optical amplification is not possible due to the carrier absorption, which is not the case of parallel demonstration of III-V layers [72]. The life time of the excess carrier is depending on the doping profile, which can be increased by using Ge on insulator substrate or built-in fields to keep them away from the interface [73].

1.6 DIRECT GAP EMISSION AND ELECTROLUMINESCENCE IN GE

Doped Germanium is capable of behaving like a direct band gap material [8]. In this approach, Ge was grown on Si in a CVD system, and 0.2 % tensile strain was achieved due to the different thermal expansion coefficient of germanium compared to that of silicon. Different in-situ doping and ion implantation techniques were applied to provide n^+ doping in the Ge layer. Room temperature LEDs have been demonstrated with an internal quantum efficiency of 10^{-3} [74]. Calculations have been performed to study the direct optical gain and net gain relative to n-type doping density, the injected carrier density on relaxed Ge and 0.25 % tensile strained Ge. Furthermore, calculations of the dependence of the net gain on the excess carrier density of n^+ Ge showed a decrease in the net gain for $> 10^{19}\,\mathrm{cm}^{-3}$ carrier density. The internal quantum efficiency of a Si-Ge p-i-n heterojunction has been calculated and it was pointed out that it can be enhanced by doping the Si-Ge heterojunction to become p^+-n^+-n^+. The optical loss can be reduced by controlling the doping concentration of both p and n Si without affecting the properties of the emitted light [66]. It has been reported that a Ge metal-insulator semiconductor light-emitting diode under 0.32 % biaxial tensile strain has shown an electroluminescence peak at 1813 nm at 65 K [75], and the direct bandgap narrowing reported in ref. [76]. The direct bandgap electroluminescence in the communication band from SiGe heterojunction LED at room temperature was reported where Ge was under 0.2 % tensile biaxial strain. Experimentally, the Interband electroluminescence (EL) of the tensile strained Ge/Si p-i-n diode increases with the applied electrical current, Higher EL is obtained at higher temperatures [63]. At forward bias, the direct and indirect electroluminescence both increase with current injection level. The enhancement of direct transition peak is prominent at $> 400\,\mathrm{mA}$ and the redshift and spectral broadening are mainly due to the junction temperature [70].

1.7 GE LASER

Liu *et. al.* modelled $\sim 400\,\mathrm{cm}^{-1}$ gain from the direct transition in 0.25 % tensile strained heavily doped Ge ($7.9 \times 10^{19}\mathrm{cm}^{-3}$) with $\sim 6\,\mathrm{kA}$ threshold current density for an edge-emitting double heterojunction (n-Si/n-Ge/p-Si) laser device structure [8]. Experimentally, lasing at room temperature has been produced using a coupled laser source from highly n^+ doped Ge with moderate tensile strain, epitaxially grown on Si [77].

An optical gain coefficient of $\sim 50\,\mathrm{cm}^{-1}$ at 1605 nm has been reported in n^+ ($10^{19}\,\mathrm{cm}^{-3}$) tensile strained (0.25 %) Ge (with an area of 500 μm^{-2}) on Si under steady-state optical pumping at room temperature. The maximum gain coefficient of $56 \pm 25\,\mathrm{cm}^{-1}$ was observed at 1605 nm, ($> 100\,\mathrm{dB\,cm}^{-1}$) which is much greater than the waveguide loss in Si photonics [25].

Liu *et.al.* demonstrated experimentally lasing spectrum with gain at 1590 – 1610 nm from an optically pumped edge-emitting multimode Ge-on-Si laser operating, at room temperature [67]. Using a Fabry-Perot (F.P.) cavity a 1 mW gain around $200\,\mathrm{cm}^{-1}$ from an electrically pumped Ge on Si laser at room temperature was observed [78], where the emission wavelength was around 1520 nm. The Ge layers were n-type doped using a delta doping process and chemical-mechanical polishing (CMP) to achieve a density of $> 4 \times 10^{19}\,\mathrm{cm}^{-3}$ [79, 80]. Such high n-type doping lead to band gap energy narrowing which will redshift the optical gain peak and affect its value as well [81].

1.8 THESIS STRUCTURE

Following an introduction to Ge as semiconductor material and background theory about the electronic band structure, two methods to obtain the band structure are described. Then, the theory of the effect of strain and differ-

ently grown crystal orientations is described. Chapter 3 investigates the effect of different strain conditions on the direct band gap energy, and the doping requirements, of bulk Ge and Ge quantum wells grown on [001], [110] and [111] oriented substrates and subjected to different types of tensile strain to achieve a direct band gap. Also, the fraction of the injected carriers (the injection efficiency) is calculated in order to find optimum strain conditions, suitable for bulk or quantum well active layers of near infrared Ge lasers. Chapter 4 demonstrates the difference between the inter-band gain and the intervalence band absorption (IVBA). Then the effect of carrier density and temperature for strained bulk Ge material is studied. Chapter 5 investigates the effect of different free carrier absorption (FCA) processes on bulk Ge and then presents their effect on the net gain. Chapter 6 summarises the results of previous chapters together and lists possible research directions for future work.

2

GERMANIUM

Germanium is one of the important semiconductor materials with an indirect band gap. For indirect band gap materials, it is not possible to have a light transition without phonon-assisted process, due to the difference in momentum between the electron in the lowest indirect conduction band and holes in the valence band, which gives rise to inefficient radiative recombination from the indirect valleys. However, the direct band transition in Ge, which is possible, has an important feature because the emitted light has 1550 nm wavelength, which is within the communications band at room temperature [25]. Also, the direct band transition in Ge has a fast recombination rate, as efficient as in III-V semiconductor materials, and Ge is thus expected to be a possible candidate for laser operation, fully compatible with Si technology [26].

This chapter will give an introduction to Ge as a semiconductor material, background theory about the electronic band structure, and two methods to obtain the $E - k$ diagram. This is followed by the theory of the effect of strain and different grown crystal orientations on the energy of the conduction bands minima and valence band top.

2.1 GE PROPERTIES

Germanium has a face-centred cubic (fcc) Bravais lattice structure, with a lattice constant a_l. An extra atom is placed at $\frac{1}{4}(\mathbf{a_1} + \mathbf{a_2} + \mathbf{a_3})$ from each atom of the fcc. For such structure if all atoms are of the same material, like in Germanium, it is called the diamond crystal structure, fig. (2.1).

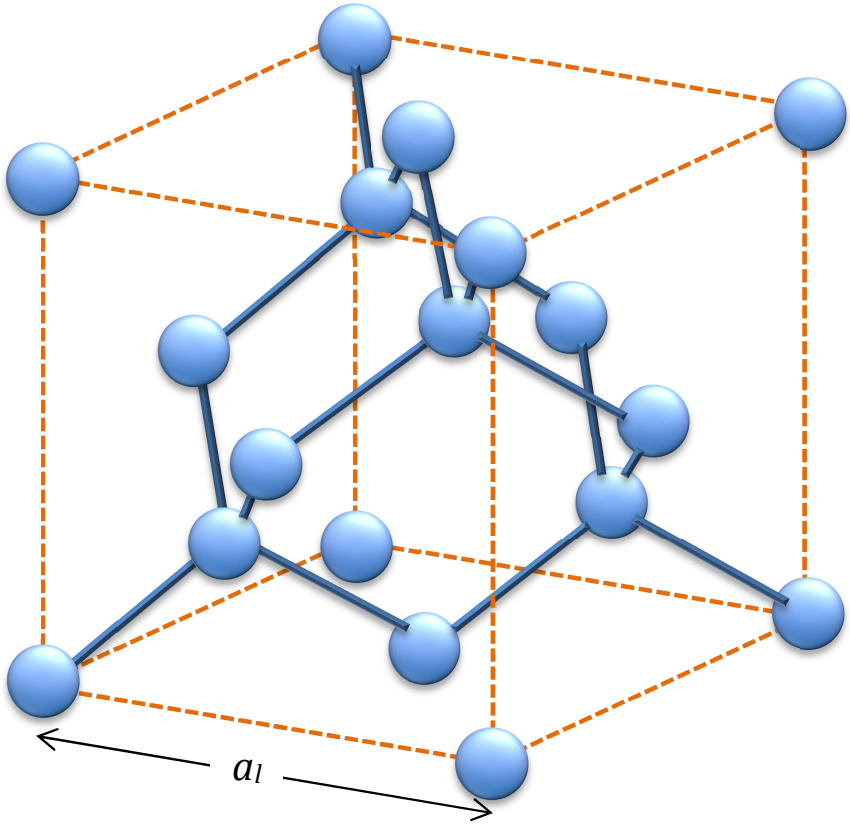

Figure 2.1: The diamond crystal lattice structure with a_l as the lattice constant [4].

Table (2.1) gives some of basic material parameters for Germanium, like the lattice and elastic constants, the deformation potentials and the spin orbit splitting.

Table 2.1: List of some basic material parameters for Germanium and their units. The lattice constant a_l; the elastic constant C_{11}, C_{12} and C_{44}; the deformation potentials Ξ_d^k and Ξ_u^k for valley k; the spin-orbit splitting Δ [6, 16, 17].

Constant	value	Unit
a_l	5.65	Å
C_{11}	1.315	$\times 10^{12}\ \frac{\text{dyn}}{\text{cm}^2}$
C_{12}	0.494	
C_{44}	0.684	
Δ	0.296	eV

Constant	value	Unit
Ξ_d^Γ	-8.24	eV
Ξ_d^L	-6.58	
Ξ_d^X	-0.59	
Ξ_u^L	15.13	
Ξ_u^X	9.42	

2.1.1 *Brillouin zone for diamond crystal structure*

The reciprocal lattice for an fcc real-space lattice has a body centred cubic (bcc) structure and the first Brillouin zone (BZ) has a truncated octahedron shape. This shape has a number of important symmetry points and directions. Figure (2.2) shows the Brillouin zone of the fcc Bravais lattice. In the Ge case there are three important symmetry points: the Γ point which is located at $(0,0,0)$, eight L points located at $\left(\frac{\pi}{a_l}, \frac{\pi}{a_l}, \frac{\pi}{a_l}\right)$, and six points labelled as X at $\frac{2\pi}{a_l}(1,0,0)$ in k-space [5].

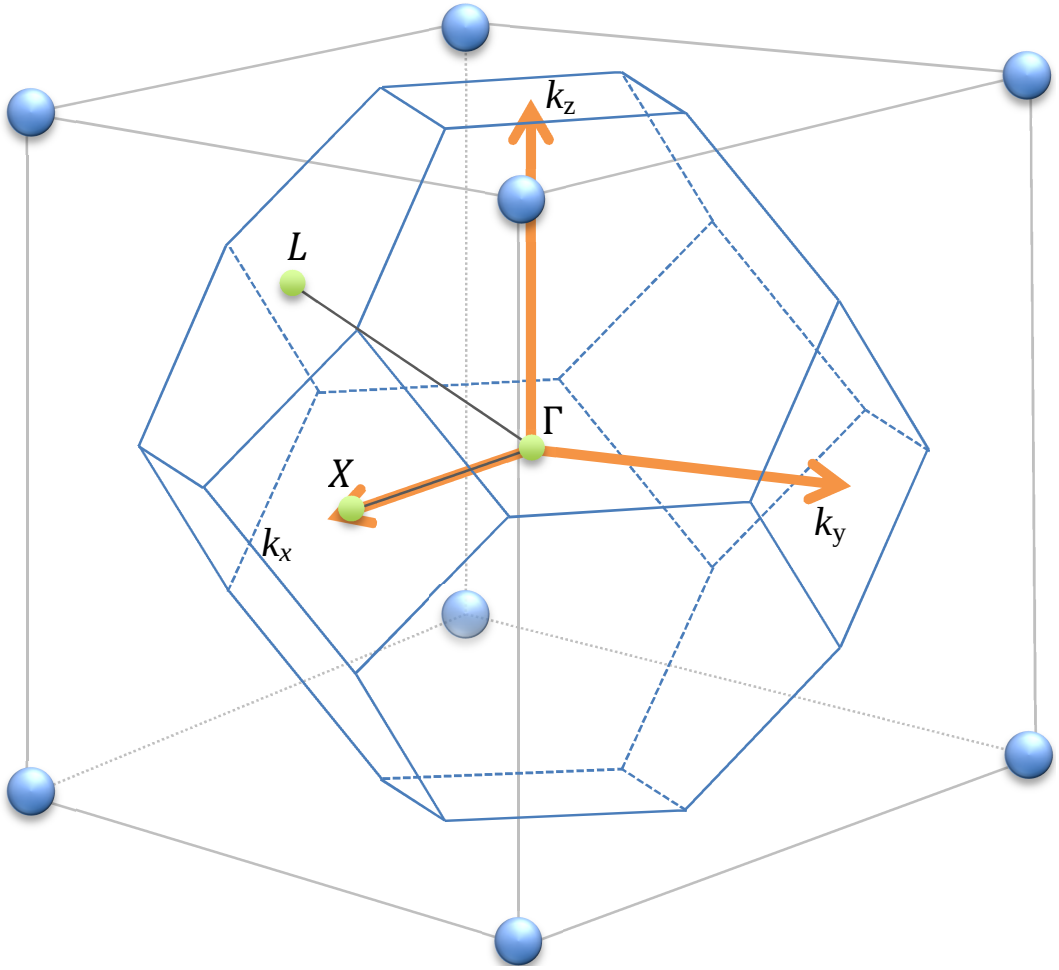

Figure 2.2: The *fcc* lattice first Brillouin zone in the reciprocal space, and three important symmetry points (Γ, *L* and *X*) in Ge After ref. [5].

2.2 BULK GE BAND STRUCTURE

In solid state physics, the electronic energy levels are generally determined by solving the time-dependent Schrodinger equation:

$$\left[\frac{-\hbar^2}{2m}\nabla^2 + V(\vec{r})\right]\psi_{\vec{k}}(\vec{r}) = E\left(\vec{k}\right)\psi_{\vec{k}}(\vec{r}), \tag{2.1}$$

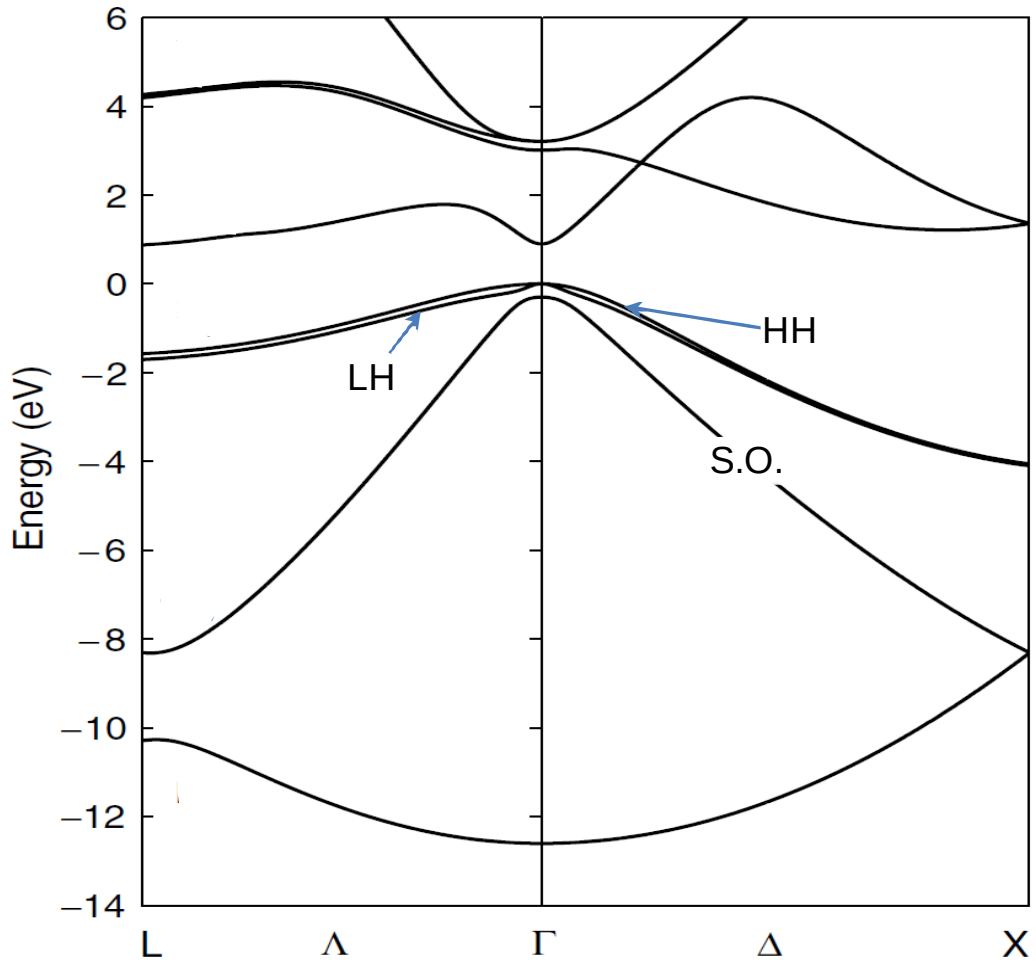

Figure 2.3: The electronic band structure of intrinsic bulk Ge, where energy is a function of wavevector between the important symmetry points in the reciprocal space. Adapted from ref. [6].

where $V(\vec{r})$ is the periodic potential of the atoms, $\vec{k}$ is the Bloch wavevector in the first B.Z., and $\psi_{\vec{k}}(\vec{r})$ is the eigenfunction (Bloch function) [82].

For any bulk semiconductor crystal the electron energy as a function of wavevector can be determined using methods like the **k**.**p** method [6] or the non local pseudo-potential method [83]. Figure (2.3) shows the energy band structure of intrinsic bulk Ge, where the energy of electrons (in eV unit) is shown as a function of the wavevector between the previously mentioned symmetry points in the reciprocal space.

At absolute zero (0 K) temperature, every electronic band higher than the valence band is entirely empty, these bands are called conduction bands (C.B.). The lower electronic bands are completely filled with electrons, they are called the valence bands (V.B.).

Germanium is an indirect band gap semiconductor material. The maximum energy of the valence band is located at the Γ point, and the minimum energy of the conduction band is located at the L point for Ge. Since electrons tend to populate the lowest conduction band valley the direct transition (light emission) in Ge is difficult.

2.2.1 *The valence band*

At finite temperature, the valence bands are highly occupied by electrons. For Ge, the three highest valence bands are: the heavy-hole (HH), the light-hole (LH), and the spin-orbit split-off (SO) band. At the Γ-point, where the maximum of the V.B. is located, the HH and the LH bands are both degenerate, but the SO band has a lower energy, fig. (2.3) [83]. The energy of the valence band maximum is:

$$E^{\mathrm{v}} = E^{\mathrm{v}}_{avg} + \frac{\Delta}{3}, \tag{2.2}$$

where E^{v}_{avg} is the average energy of the three valence bands and Δ is the spin-orbit splitting [20].

2.2.2 *The conduction band*

The minimum of the conduction band energy ($E^{\mathrm{c},\mathrm{k}_i}$) of a particular symmetry - Γ, L or X - point, called a valley, (k) is calculated with reference to the maximum of the valence band energy E^{v} from:

$$E^{c,k_i} = E^{g,k_i} + E^{v}, \tag{2.3}$$

where i is the index of the conduction band minimum at that k-point [20]. At the bulk Ge, the conduction band minima (L-points) only half of the eight valleys are inside the first Brillouin zone, since they are located at the Brillouin zone edge, unlike the six valleys near the X-points [5].

The band structure can be determined by solving the Schrodinger equation. The effective mass method gives a good approximation to the relation of the energy-momentum of around that band bottom. While with more than one band with close energy to each other such approximation is not good. Because the envelope wave function does not contain the true wavefunction. So in this work, near the Γ-point the **k**.**p** method is used to calculate the band structure for the conduction and valence bands, and the effective mass method is used to calculate the band structure for the conduction band for indirect valleys. These two methods will be described in the following sections [84].

2.3 THE EFFECTIVE MASS METHOD

In a periodic crystal, when an electric field ξ applied the electron accelerates as

$$\frac{dv}{dt} = -\frac{e\xi}{m^*}, \tag{2.4}$$

where e is the electron charge and m_e is the electron mass [82]. So the electron behaves like its mass is different from the free electron mass m_0. The kinetic energy (E) of a free electron as a function of the electron momentum (p) is

$$E = \frac{p^2}{2m^*} = \frac{\hbar^2 k^2}{2m^*}. \tag{2.5}$$

Therefore, the energy-momentum ($E - p$) relationship has a parabolic dependence such as that of a classical free electron [82].

When an external force is applied, the electron acceleration can be interpreted in the Newton equation form, the effective mass principle may be presented:

$$m^* = \hbar^2 \frac{1}{\frac{d^2E}{dk^2}}. \tag{2.6}$$

2.3.1 *The effective mass tensor*

In a three dimensional crystal the effective mass tensor is defined as

$$\frac{1}{m^*} = \begin{pmatrix} m_{xx}^{-1} & m_{xy}^{-1} & m_{xz}^{-1} \\ m_{yx}^{-1} & m_{yy}^{-1} & m_{yz}^{-1} \\ m_{zx}^{-1} & m_{zy}^{-1} & m_{zz}^{-1} \end{pmatrix}, \tag{2.7}$$

$$E = k^T \left(\frac{1}{m^*}\right) k. \tag{2.8}$$

For a parabolic $E - k$ dependence all non-diagonal elements in the tensor will vanish, and the effective mass for a conduction band becomes a scalar m^* in this approximation [15, 85].

2.3.2 *The parabolic band approximation model*

In this approximation model for parabolic bands, the electron moves as a free particle with mass m^*, which is related to the curvature of the band. For non-parabolic bands, the electron effective mass is not constant and the slope at some point of the E–k curvature relationship must be used to obtain the velocity and acceleration of the particle with energy E.

For a single band and near the valley bottom (top) for conduction (valence) bands, the E–k dependence can be approximated by parabola that results in a constant effective mass value. The valence band energy in eq. (2.2) will be used to obtain the valence band E–k diagram

$$E^{\mathrm{v}}(k) = E^{\mathrm{v}}(0) + \frac{\hbar^2 k^{2,}}{2m_h} \tag{2.9}$$

where m_h here is negative, and the conduction band from eq. (2.3) also will be used to determine E–k relation for k-valley as

$$E^{c,\mathrm{k}_i}(k) = E^{c,\mathrm{k}_i}(0) + \frac{\hbar^2 k^2}{2m_e}. \tag{2.10}$$

2.4 THE **k.p** METHOD

The valence band energy shifts under the strain, and can be calculated using the **k.p** method. This involves finding the eigenvalues (Ψ) and the eigenvectors (E) of the 8×8 Luttinger-Kohn Hamiltonian with spin-orbit interaction ($\mathcal{H}$) and with no strain, then by adding the strain-dependant Hamiltonian ($\mathcal{H}_s$):

$$(\mathcal{H} + \mathcal{H}_s(r))\,\Psi(r) = E\Psi(r), \tag{2.11}$$

where $\mathcal{H}$ is

$\mathcal{H}_{8\times 8} =$

$$\begin{bmatrix}
A & 0 & T^*+V^* & 0 \\
0 & A & \sqrt{2}(W-U) & -\sqrt{3}(T^*+V^*) \\
T+V & \sqrt{2}(W^*-U) & -P+Q & -S^* \\
0 & -\sqrt{3}(T+V) & -S & -P-Q \\
-\sqrt{3}(T^*-V^*) & 0 & R^* & 0 \\
\sqrt{2}(W^*-U) & T^*-V^* & 0 & R^* \\
W^*-U & -\sqrt{2}(T^*-V^*) & \sqrt{\tfrac{3}{2}}S^* & -\sqrt{2}R^* \\
\sqrt{2}(T+V) & W+U & -\sqrt{2}Q & S^*/\sqrt{2}
\end{bmatrix}$$

$$\begin{bmatrix}
-\sqrt{3}(T-V) & \sqrt{2}(W-U) & W-U & \sqrt{2}(T^*-V^*) \\
0 & T-V & -\sqrt{2}(T-V) & W^*+U \\
R & 0 & \sqrt{\tfrac{3}{2}}S & -\sqrt{2}Q \\
0 & R & -\sqrt{2}R & S/\sqrt{2} \\
-P-Q & S^* & S^*/\sqrt{2} & \sqrt{2}R^* \\
S & -P+Q & \sqrt{2}Q & \sqrt{\tfrac{3}{2}}S^* \\
S/\sqrt{2} & \sqrt{2}R & -P-\Delta & 0 \\
-\sqrt{2}R & \sqrt{\tfrac{3}{2}}S & 0 & -P-\Delta
\end{bmatrix}, \tag{2.12}$$

where:

$$A = E^{c,k_i} + \left[A' + \tfrac{\hbar^2}{2m_0}\right]\left(k_x^2+k_y^2+k_z^2\right),$$

$$T = \tfrac{1}{\sqrt{6}}Bk_z\left(k_x+ik_y\right),$$

$$V = \tfrac{1}{\sqrt{6}}P_0\left(k_x-ik_y\right),$$

$$W = i\tfrac{1}{\sqrt{3}}Bk_xk_y,$$

$$U = \tfrac{1}{\sqrt{3}}P_0k_z,$$

$$P = -E^v + \tfrac{\hbar^2}{2m_0}\gamma_1\left(k_x^2+k_y^2+k_z^2\right),$$

$Q = \frac{\hbar^2}{2m_0}\gamma_2\left(k_x^2 + k_y^2 - 2k_z^2\right)$,

$S = \frac{\sqrt{3}\hbar^2}{m_0}\gamma_3 k_z\left(k_x - ik_y\right)$,

$R = -\frac{\sqrt{3}}{2}\frac{\hbar^2}{m_0}\left[\gamma_2\left(k_x^2 + k_y^2\right) - 2i\gamma_3 k_x k_y\right]$ [86, 18].

The strain-dependent Hamiltonian ($\mathcal{H}_{s_{8\times8}}$) is

$\mathcal{H}_{s_{8\times8}} =$

$$\begin{bmatrix}
a'\varepsilon & 0 & t^* - v^* & 0 \\
0 & a'\varepsilon & \sqrt{2}\,(w+u) & -\sqrt{3}\,(t^* - v^*) \\
t - v & \sqrt{2}\,(w^* + u) & -p + q & -s^* \\
0 & -\sqrt{3}\,(t - v) & -s & -p - q \\
-\sqrt{3}\,(t^* + v^*) & 0 & r^* & 0 \\
\sqrt{2}\,(w^* + u) & t^* + v^* & 0 & r^* \\
w^* + u & -\sqrt{3}\,(t^* + v^*) & \sqrt{\tfrac{3}{2}}s^* & -\sqrt{2}r^* \\
\sqrt{2}\,(t - v) & w - u & -\sqrt{2}q & s^*/\sqrt{2}
\end{bmatrix}$$

$$\begin{bmatrix}
-\sqrt{3}\,(t + v) & \sqrt{2}\,(w+u) & w + u & \sqrt{2}\,(t^* - v^*) \\
0 & t + v & -\sqrt{2}\,(t + v) & w^* - u \\
r & 0 & \sqrt{\tfrac{3}{2}}s & -\sqrt{2}q \\
0 & r & -\sqrt{2}r & s/\sqrt{2} \\
-p - q & s^* & s^*/\sqrt{2} & \sqrt{2}r^* \\
s & -p + q & \sqrt{2}q & \sqrt{\tfrac{3}{2}}s^* \\
s/\sqrt{2} & \sqrt{2}r & -p & 0 \\
-\sqrt{2}r & \sqrt{\tfrac{3}{2}}s & 0 & -p
\end{bmatrix}, \tag{2.13}$$

where:

$\varepsilon = \varepsilon_{xx} + \varepsilon_{yy} + \varepsilon_{zz}$,

$t = \frac{1}{\sqrt{6}}b'\left(\varepsilon_{xz} + i\varepsilon_{yz}\right)$,

$v = \frac{1}{\sqrt{6}}P_0\sum_j\left(\varepsilon_{xj} - i\varepsilon_{yj}\right)k_j$,

$$w = i\frac{1}{\sqrt{3}}b'\varepsilon_{xy},$$

$$u = \frac{1}{\sqrt{3}}P_0 \sum_j \varepsilon_{zj}k_j,$$

$$p = a\varepsilon,$$

$$q = b\left[\varepsilon_{zz} - \frac{1}{2}\left(\varepsilon_{xx} + \varepsilon_{yy}\right)\right],$$

$$s = -d\left(\varepsilon_{xz} - i\varepsilon_{yz}\right),$$

$$r = \frac{\sqrt{3}}{2}b\left(\varepsilon_{xx} + \varepsilon_{yy}\right) - id\varepsilon_{xy},$$

and A', B are the Kane parameters ($= 0$ for diamond crystal structure), a,b,d, a' and b' are the deformation potential constants, γ_1,γ_2,γ_3 are the Luttinger parameters [86, 18].

The modified Luttinger parameters can be calculated form

$$\gamma_1 = \gamma_1^L - \frac{E_P}{3E^g + \Delta},$$

$$\gamma_{2,3} = \gamma_{2,3}^L - \frac{1}{2}\frac{E_P}{3E^g + \Delta},$$

where E^g is the direct band gap, $E_P = \frac{2m_0}{\hbar^2}P_0^2$ [18].

Table (2.2) lists the constant values for Ge which were used in the calculations.

Table 2.2: The values of deformation potentials a,b,d and a', b' in (eV), the modified Luttinger parameters γ_1^L,γ_2^L,γ_3^L [18, 19, 20] .

Constant	a	b	d	a'	b'	γ_1^L	γ_2^L	γ_3^L
value	1.24	−2.90	−5.30	−8.24	0.0	13.38	4.24	5.69

2.5 STRAIN EFFECT

To obtain any semiconductor device, a semiconductor material or alloy will be grown on another layer. If their lattice constants are different, the mismatch between the two layers will induce stress in the top material. In an elastic solid, the strain is directly proportional to the stress, as given by Hooke's law. Consider a mechanical force acting on a crystal lattice and changing the positions of the atoms, which leads to changing of the primitive cell size and shape [5]. When a semiconductor material is grown on another semiconductor substrate, such as Ge or SiGe alloy layer on Si substrate, there will be a lattice mismatch between these two materials [5, 87]. In this part, the physics of strain will be introduced, which will then it affect the band structure.

2.5.1 *Strain tensor*

When the lattice is under stress it becomes strained. The deformation is described as elastic if the primitive cell returns to its original status after the force is removed. When an elastic deformation of a primitive cell takes place then new axes $\mathbf{x}'$, $\mathbf{y}'$and $\mathbf{z}'$ describe the new positions of the deformed primitive cell in terms of the original three orthogonal vectors of unit length in the Cartesian coordinate system $\hat{\mathbf{x}}$, $\hat{\mathbf{y}}$ and $\hat{\mathbf{z}}$ as follows:

$$\mathbf{x}' = (1 + \epsilon_{xx})\hat{\mathbf{x}} + \epsilon_{xy}\hat{\mathbf{y}} + \epsilon_{xz}\hat{\mathbf{z}}, \tag{2.14}$$

$$\mathbf{y}' = \epsilon_{yx}\hat{\mathbf{x}} + (1 + \epsilon_{yy})\hat{\mathbf{y}} + \epsilon_{yz}\hat{\mathbf{z}}, \tag{2.15}$$

$$\mathbf{z}' = \epsilon_{zx}\hat{\mathbf{x}} + \epsilon_{zy}\hat{\mathbf{y}} + (1 + \epsilon_{zz})\hat{\mathbf{z}}, \tag{2.16}$$

where $\epsilon_{\alpha\beta}$ are dimensionless coefficients of the deformation and have values $\ll 1$ for elastic strain [87]. If the original position of an atom located at $\mathbf{r} = x\hat{\mathbf{x}} + y\hat{\mathbf{y}} + z\hat{\mathbf{z}}$ becomes after deformation, $\mathbf{r}' = x\mathbf{x}' + y\mathbf{y}' + z\mathbf{z}'$, then the deformation $\mathbf{R}$ is defined by

$$\mathbf{R}(r) = \mathbf{r}' - \mathbf{r} = u(\mathbf{r})\,\hat{\mathbf{x}} + v(\mathbf{r})\,\hat{\mathbf{y}} + w(\mathbf{r})\,\hat{\mathbf{z}}, \tag{2.17}$$

where

$$u(r) = \epsilon_{xx} + \epsilon_{xy} + \epsilon_{xz},$$

$$v(r) = \epsilon_{yx} + \epsilon_{yy} + \epsilon_{yz},$$

$$w(r) = \epsilon_{zx} + \epsilon_{zy} + \epsilon_{zz},$$

Using the Taylor series expansion of $\mathbf{R}$ the strain components are defined as [5]:

$$\varepsilon_{xx} \equiv \epsilon_{xx} = \frac{\partial u}{\partial x}; \quad \varepsilon_{yy} \equiv \epsilon_{yy} = \frac{\partial v}{\partial y}; \quad \varepsilon_{zz} \equiv \epsilon_{zz} = \frac{\partial w}{\partial z}. \tag{2.18}$$

The rest of strain components represent the angles between the deformed axes:

$$\varepsilon_{\alpha\beta} \equiv \alpha' \cdot \beta' \cong \epsilon_{\beta\alpha} + \epsilon_{\beta y} = \frac{\partial u_\alpha}{\partial \beta} + \frac{\partial u_\beta}{\partial \alpha}, \qquad \alpha,\beta = \mathbf{x}', \mathbf{y}' \text{ and } \mathbf{z}', \tag{2.19}$$

and $\varepsilon_{\alpha\beta} = \varepsilon_{\beta\alpha}$ and they are dimensionless. The dilation δ (the fractional increase of volume of the cube) [5] can be written as

$$\delta \equiv \frac{V' - V}{V} \cong \varepsilon_{xx} + \varepsilon_{yy} + \varepsilon_{zz}. \tag{2.20}$$

Nine stress components ($\sigma_{\alpha\beta}$) represent the applied force acting on unit area of the cube. They are σ_{xx} , σ_{xy} , σ_{xz}, σ_{yx} , σ_{yy} , σ_{yz} , σ_{zx}, σ_{zy} and σ_{zz}, with α indicating the direction of the force and β indicating the axis perpendicular to the plane which the force acts on. Because the body is in static

equilibrium, the sum of the forces in any direction is zero, so there are only six independent stress components, listed below, which are related to the strain components as:

$$\begin{bmatrix} \sigma_{xx} \\ \sigma_{yy} \\ \sigma_{zz} \\ \sigma_{yz} \\ \sigma_{zx} \\ \sigma_{xy} \end{bmatrix} = \begin{bmatrix} C_{11} & C_{12} & C_{13} & C_{14} & C_{15} & C_{16} \\ C_{21} & C_{22} & C_{23} & C_{24} & C_{25} & C_{26} \\ C_{31} & C_{32} & C_{33} & C_{34} & C_{35} & C_{36} \\ C_{41} & C_{42} & C_{43} & C_{44} & C_{45} & C_{46} \\ C_{51} & C_{52} & C_{53} & C_{54} & C_{55} & C_{56} \\ C_{61} & C_{62} & C_{63} & C_{64} & C_{65} & C_{66} \end{bmatrix} \begin{bmatrix} \varepsilon_{xx} \\ \varepsilon_{yy} \\ \varepsilon_{zz} \\ \varepsilon_{yz} \\ \varepsilon_{zx} \\ \varepsilon_{xy} \end{bmatrix}. \tag{2.21}$$

The quantities C_{mn} are the elastic stiffness constants [87]. The elastic stiffness (C) matrix is represented by [5]:

$$C_{6\times6} = \begin{bmatrix} C_{11} & C_{12} & C_{12} & 0 & 0 & 0 \\ C_{12} & C_{11} & C_{12} & 0 & 0 & 0 \\ C_{12} & C_{12} & C_{11} & 0 & 0 & 0 \\ 0 & 0 & 0 & C_{44} & 0 & 0 \\ 0 & 0 & 0 & 0 & C_{44} & 0 \\ 0 & 0 & 0 & 0 & 0 & C_{44} \end{bmatrix}. \tag{2.22}$$

There are only three independent stiffness constants C_{11}, C_{12} and C_{44} due to the crystal symmetry. the C_{44} is defined as a link between the "engineering" shear strain with the stress components [where the engineering shear strain ($2\varepsilon_{\alpha\beta}$) is the change of the angle between previously orthogonal axes], so the 6×1 representations of strain ($\varepsilon_{6\times1}$) and stress($\sigma_{6\times1}$) are used and linked with the conventional $C_{6\times6}$ matrix. However, the 3×3 representation of $\varepsilon_{3\times3}$ which would contain these $2\varepsilon_{\alpha\beta}$ terms is not a tensor, so rotations of coordinate system cannot be applied to it. Instead, the 3×3 representation

of epsilon, which contains just $\varepsilon_{\alpha\beta}$ off the main diagonal, is a tensor, and rotations can be applied to this form [88].

Therefore, the strain (ε) matrix in the crystal coordinate system can be written as:

$$\varepsilon_{3\times3} = \begin{bmatrix} \varepsilon_{xx} & \varepsilon_{xy} & \varepsilon_{xz} \\ \varepsilon_{xy} & \varepsilon_{yy} & \varepsilon_{yz} \\ \varepsilon_{xz} & \varepsilon_{yz} & \varepsilon_{zz} \end{bmatrix}, \tag{2.23}$$

where the diagonal strain elements are the relative displacements in the three coordinate directions $\hat{\mathbf{x}}$, $\hat{\mathbf{y}}$, $\hat{\mathbf{z}}$ and the other elements are one-half of the changes in the angle between the two perpendicular axes [87]. Also, the strain can be represented in 6×1 matrix form as:

$$\varepsilon_{6\times1} = \begin{bmatrix} \varepsilon_{xx} & \varepsilon_{yy} & \varepsilon_{zz} & 2\varepsilon_{xy} & 2\varepsilon_{yz} & 2\varepsilon_{xz} \end{bmatrix}^T. \tag{2.24}$$

The stress component matrix for a cubic crystal as in eq.(2.21) can be written as

$$\sigma_{6\times1} = C_{6\times6} \cdot \varepsilon_{6\times1}, \tag{2.25}$$

where the stress matrix in (6×1) form and in (3×3) form in the crystal coordinate system are [87]:

$$\sigma_{6\times1} = \begin{bmatrix} \sigma_{xx} & \sigma_{yy} & \sigma_{zz} & \sigma_{xy} & \sigma_{yz} & \sigma_{xz} \end{bmatrix}^T, \tag{2.26}$$

$$\sigma_{3\times3} = \begin{bmatrix} \sigma_{xx} & \sigma_{xy} & \sigma_{xz} \\ \sigma_{xy} & \sigma_{yy} & \sigma_{yz} \\ \sigma_{xz} & \sigma_{yz} & \sigma_{zz} \end{bmatrix}, \tag{2.27}$$

The grown layer with lattice constant (a_l) undergoes a compressive or tensile strain in order to match the lattice constant of the substrate (a_s). The compressive or tensile strain depends on whether the lattice constant of the grown material is larger or smaller than the lattice constant of the substrate. The substrate remains unstrained owing to its large thickness. Furthermore, if, during growth the lattice undergoes tensile strain in the in-plane direction, there will be an orthogonal compressive strain and vice versa [89]. The in-plane strain $\varepsilon_{||}$is calculated from:

$$\varepsilon_{||} = \frac{a_s - a_l}{a_l}, \tag{2.28}$$

2.5.2 *Deformation potential method*

After determining the strain, it is possible to find the change in the conduction band energy various for valleys (k_i) by:

$$\Delta E^{\mathrm{k}_i} = \Xi_d^{\mathrm{k}} \mathrm{Tr}(\varepsilon) + \Xi_u^{\mathrm{k}} \boldsymbol{a}_{\mathrm{k}_i}^T \, \varepsilon \, \boldsymbol{a}_{\mathrm{k}_i}, \tag{2.29}$$

where the deformation potential of pure dilations (Ξ_d) and pure shears (Ξ_u), for valley k. Where $\mathrm{k} = \Gamma$, X or L, and i goes over all equivalent valleys [90]. The$\boldsymbol{a}_{\mathrm{k}_i}$ is the unit vector pointing to that valley [20, 89]. The unit vectors of X and L equivalent valleys are:

$$a_{X_1} = \begin{bmatrix} 1 \\ 0 \\ 0 \end{bmatrix}, \quad a_{X_2} = \begin{bmatrix} 0 \\ 1 \\ 0 \end{bmatrix}, \quad a_{X_3} = \begin{bmatrix} 0 \\ 0 \\ 1 \end{bmatrix}, \tag{2.30}$$

$$a_{L_1} = \frac{1}{\sqrt{3}}\begin{bmatrix}1\\1\\1\end{bmatrix}, \qquad a_{L_2} = \frac{1}{\sqrt{3}}\begin{bmatrix}1\\1\\-1\end{bmatrix},$$
$$a_{L_3} = \frac{1}{\sqrt{3}}\begin{bmatrix}-1\\1\\1\end{bmatrix}, \qquad a_{L_4} = \frac{1}{\sqrt{3}}\begin{bmatrix}1\\-1\\1\end{bmatrix}. \tag{2.31}$$

Note that the Γ valley does not have a shear deformation potential. The new minimum conduction band energy of a particular valley (k) , eq. (2.3), is calculated by adding the energy change of the minimum in the presence of strain (ΔE^{k_i}) to the conduction band minimum with no strain (E^{g,k_i}) of a particular valley (k), plus the energy of the valence band maximum (because E^{g,k_i} is measured from E^{v}) as follows:

$$E^{c,k_i} = \Delta E^{k_i} + E^{g,k_i} + E^{v}. \tag{2.32}$$

The top of the valence band energy can be calculated from eq. (2.2). The energy of valence band top (E^{v}) in the absence of strain is set to zero [89].

2.6 GROWTH ORIENTATION EFFECT

When a layer is grown with a particular orientation ([001], [110] or [111] plane) of the crystal coordinate system, $\mathbf{x}'$, $\mathbf{y}'$ and $\mathbf{z}'$ are chosen so that $\mathbf{z}'$ is perpendicular to the growth plane. The coordinate transformation can be made to find the strain and stress in the new layer (growth) coordinate system.

$$\varepsilon'_{3\times3} = U \cdot \varepsilon_{3\times3} \cdot U^T, \tag{2.33}$$

$$\sigma'_{3\times3} = U \cdot \sigma_{3\times3} \cdot U^T, \tag{2.34}$$

or vice versa from

$$\varepsilon_{3\times3} = U^T \cdot \varepsilon'_{3\times3} \cdot U, \tag{2.35}$$

where U is the transformation matrix. For the growth direction [001], in this case $U_{[001]}$ is just the unity matrix I.

2.6.1 *The transformation matrix*

For other growth directions the crystal lattice will not be aligned with the crystal layer ($\mathbf{R} \neq \mathbf{R}'$), then a transformation matrix U is needed to transform from one Cartesian coordinate system to another as in eq. (2.35). The transformation is performed first by clockwise rotation through an angle (θ) around the $\hat{\mathbf{z}}$-axis, then by clockwise rotation through an angle (φ) around the new $\mathbf{y}'$-axis. These angles are called Euler angles. The transformation matrix is defined as [89]:

$$U = \begin{bmatrix} \cos\theta\cos\varphi & -\sin\theta & \cos\theta\sin\varphi \\ \sin\theta\cos\varphi & \cos\theta & \sin\theta\sin\varphi \\ -\sin\varphi & 0 & \cos\varphi \end{bmatrix}, \tag{2.36}$$

For the [110] and [111] growth directions the transformation matrices are $U_{[110]}$ and $U_{[111]}$ respectively, as

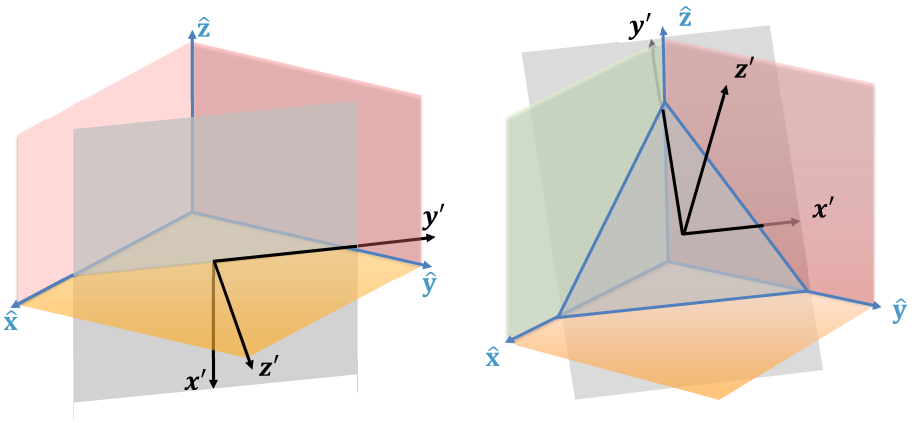

(a) z′: [110], y′: [-110], x′: [oo-1] (b) $\mathbf{z}'$: [111], $\mathbf{x}'$: $[-110]$, $\mathbf{y}'$: $[-1-12]$

Figure 2.4: Scheme of the crystal coordinate system and for the new layer coordinate system, for [110] growth (left) and for [111] growth (right), after ref. [7].

$$U_{[110]} = \begin{bmatrix} 0 & 0 & -1 \\ -\frac{1}{\sqrt{2}} & \frac{1}{\sqrt{2}} & 0 \\ \frac{1}{\sqrt{2}} & \frac{1}{\sqrt{2}} & 0 \end{bmatrix}, \qquad U_{[111]} = \begin{bmatrix} \frac{1}{\sqrt{2}} & -\frac{1}{\sqrt{2}} & 0 \\ \frac{1}{\sqrt{6}} & \frac{1}{\sqrt{6}} & -\frac{2}{\sqrt{6}} \\ \frac{1}{\sqrt{3}} & \frac{1}{\sqrt{3}} & \frac{1}{\sqrt{3}} \end{bmatrix}. \tag{2.37}$$

Figure (2.4) illustrates the transformation of the original coordinate system to the new coordinate system in case of [110] and [111] growth orientations.

2.6.2 *Effective masses*

There are six X-valleys, located at $(1,0,0)$, $(0,1,0)$, $(0,0,1)$ and $(-1,0,0)$, $(0,-1,0)$, $(0,0,-1)$, in the crystal coordinate system. The effective masses describing X-valleys (ellipsoidal constant energy surfaces) are m_ℓ (longitudinal mass, along the direction pointing from the Γ point to that X-valley), and m_t (transverse mass, in the other two directions). For the X-valley at $(1,0,0)$ the reciprocal effective mass matrix is

$$m_{X_1}^{-1} = \begin{bmatrix} m_\ell^{-1} & & \\ & m_t^{-1} & \\ & & m_t^{-1} \end{bmatrix}, \tag{2.38}$$

and it transforms in the new coordinate system (of the layer) according to

$$m_{X_1}^{-1'} = U \cdot m_{X_1}^{-1} \cdot U^T. \tag{2.39}$$

Similarly, the valleys located at $(0,1,0)$ and $(0,0,1)$ have

$$m_{X_2}^{-1} = \begin{bmatrix} m_t^{-1} & & \\ & m_\ell^{-1} & \\ & & m_t^{-1} \end{bmatrix} \quad m_{X_3}^{-1} = \begin{bmatrix} m_t^{-1} & & \\ & m_t^{-1} & \\ & & m_\ell^{-1} \end{bmatrix}, \tag{2.40}$$

and they also transform using eq. (2.39) [85].

There are four L-valleys, located at $(1,1,1)$, $(1,1,-1)$, $(-1,1,1)$ and $(1,-1,1)$. Each L-valley also has a longitudinal mass m_ℓ in the direction pointing from Γ to that L point, and a transverse mass m_t in the other two directions. However, the difference from the X-valleys is that none of these directions is along the $\hat{\mathbf{x}}$, $\hat{\mathbf{y}}$ and $\hat{\mathbf{z}}$ axes of the crystal coordinate system. To find the reciprocal mass matrix for an L-valley in the new layer (growth) coordinate system, first convert that L-valley from its own coordinate system to the crystal coordinate system using

$$m_{L_1(\text{cryst})}^{-1} = U_{111}^T \cdot m_{L_1}^{-1} \cdot U_{111}, \tag{2.41}$$

then from the crystal coordinate system to the layer coordinate system using the eq. (2.39) but with changing correspondence.

The reciprocal mass matrix for all L-valleys [85] is

$$m_L^{-1} = \begin{bmatrix} m_t^{-1} & & \\ & m_t^{-1} & \\ & & m_\ell^{-1} \end{bmatrix}, \tag{2.42}$$

but the transformation matrices for the rest of the four L-valleys, at $(1,1,1)$, $(1,1,-1)$, $(-1,1,1)$ and $(1,-1,1)$ are

$$U_{[111]}^{L_1} = \begin{bmatrix} \frac{1}{\sqrt{2}} & -\frac{1}{\sqrt{2}} & 0 \\ \frac{1}{\sqrt{6}} & \frac{1}{\sqrt{6}} & -\frac{2}{\sqrt{6}} \\ \frac{1}{\sqrt{3}} & \frac{1}{\sqrt{3}} & \frac{1}{\sqrt{3}} \end{bmatrix}, \qquad U_{[111]}^{L_2} = \begin{bmatrix} \frac{1}{\sqrt{2}} & -\frac{1}{\sqrt{2}} & 0 \\ -\frac{1}{\sqrt{6}} & -\frac{1}{\sqrt{6}} & -\frac{2}{\sqrt{6}} \\ \frac{1}{\sqrt{3}} & \frac{1}{\sqrt{3}} & -\frac{1}{\sqrt{3}} \end{bmatrix},$$

$$U_{[111]}^{L_3} = \begin{bmatrix} \frac{1}{\sqrt{2}} & -\frac{1}{\sqrt{2}} & 0 \\ -\frac{1}{\sqrt{6}} & \frac{1}{\sqrt{6}} & -\frac{2}{\sqrt{6}} \\ -\frac{1}{\sqrt{3}} & \frac{1}{\sqrt{3}} & \frac{1}{\sqrt{3}} \end{bmatrix}, \qquad U_{[111]}^{L_4} = \begin{bmatrix} \frac{1}{\sqrt{2}} & \frac{1}{\sqrt{2}} & 0 \\ -\frac{1}{\sqrt{6}} & \frac{1}{\sqrt{6}} & \frac{2}{\sqrt{6}} \\ \frac{1}{\sqrt{3}} & -\frac{1}{\sqrt{3}} & \frac{1}{\sqrt{3}} \end{bmatrix},$$

respectively.

2.7 RESULTS AND DISCUSSION

Using the coordinate transformation mentioned previously, the strain tensor was determined for (001), (110) and (111) growth directions for the semiconductor material undergoing biaxial strain (B). Then, using the deformation potential method an investigation was carried out to study the strain effects on the conduction band valley minima for bulk-like Ge.

Then, for bulk-like Ge, the two bands $\mathbf{k}.\mathbf{p}$ method was used to find the variation of the energy of the valence band maximum with different types of applied strain in the before mentioned three growth directions.

2.7.1 *Strain tensor*

The energy shift of the bottom of the three valleys of the conduction and the top of the valence band for bulk Ge has been investigated, for different strain conditions and the various growth orientations, by following the previously mentioned methodology. The strain conditions are biaxial compressive and tensile strain. The three growth orientations are the conventional [001], [110] and [111] substrates.

2.7.1.1 *Biaxial strain effect*

When a biaxial strain is applied to a bulk semiconductor material, known values of in-plane strain ($\varepsilon_{||}$) are applied along two axes (ε'_{xx},ε'_{yy}), with an unknown value along the perpendicular axis (ε'_{zz}), and with no shear strain components (ε'_{xy},ε'_{yz},ε'_{xz}). The perpendicular stress element (σ'_{zz}) equals zero, and the other tensor elements can be calculated from eq. (2.25). Then, the unknown strain tensor elements can be determined by applying these conditions in different growth directions ([001], [110] and [111]). The energy shifts of all valleys can be calculated using eq. (2.32).

Biaxial strain in the [001] growth direction

The resultant strain tensor in the [001] growth orientation is

$$\varepsilon_{[001]\mathrm{B}} = \varepsilon_{||} \begin{bmatrix} 1 & 0 & 0 \\ 0 & 1 & 0 \\ 0 & 0 & -2\frac{C_{12}}{C_{11}} \end{bmatrix}. \tag{2.43}$$

The shift in the energy of the Γ valley is

$$\Delta E^{\Gamma}_{[001]\mathrm{B}} = 2\Xi^{\Gamma}_{d}\frac{C_{11}-C_{12}}{C_{11}}\varepsilon_{||}. \tag{2.44}$$

All of the L valleys will be shifted according to

$$\Delta E^{L}_{[001]\mathrm{B}} = \frac{2}{3}\frac{C_{11}-C_{12}}{C_{11}}\left(3\Xi^{L}_{d}+\Xi^{L}_{u}\right)\varepsilon_{||}. \tag{2.45}$$

But the degeneracy will be lifted for X-valleys, and their shifts in energy are

$$\Delta E^{X_{1,3}}_{[001]\mathrm{B}} = 2\left(\frac{C_{11}-C_{12}}{C_{11}}\Xi^{X}_{d}+\Xi^{X}_{u}\right)\varepsilon_{||}, \tag{2.46}$$

$$\Delta E^{X_{2}}_{[001]\mathrm{B}} = \frac{2}{C_{11}}\left(\left(C_{11}-C_{12}\right)\Xi^{X}_{d}+C_{12}\Xi^{X}_{u}\right)\varepsilon_{||}. \tag{2.47}$$

The energy shifts for conduction band valleys minimum and the valence band top in the case of a Ge layer grown in the [001] crystal orientation are shown in fig. (2.5). The degeneracy of the X valleys is lifted and they split into four fold degenerate $X_{1,2}$ valleys, and double degenerate X_3 valleys, which they behave differently with the applied strain.

Biaxial strain in the [110] growth direction

The resultant strain tensor in the [110] growth orientation is

$$\varepsilon_{[110]\mathrm{B}} = \frac{\varepsilon_{||}}{C_{11}+C_{12}+2C_{44}} \begin{bmatrix} 2C_{44}-C_{12} & -C_{11}-2C_{12} & 0 \\ -C_{11}-2C_{12} & 2C_{44}-C_{12} & 0 \\ 0 & 0 & C_{11}+C_{12}+2C_{44} \end{bmatrix}. \tag{2.48}$$

The shift in the energy of the Γ valley is

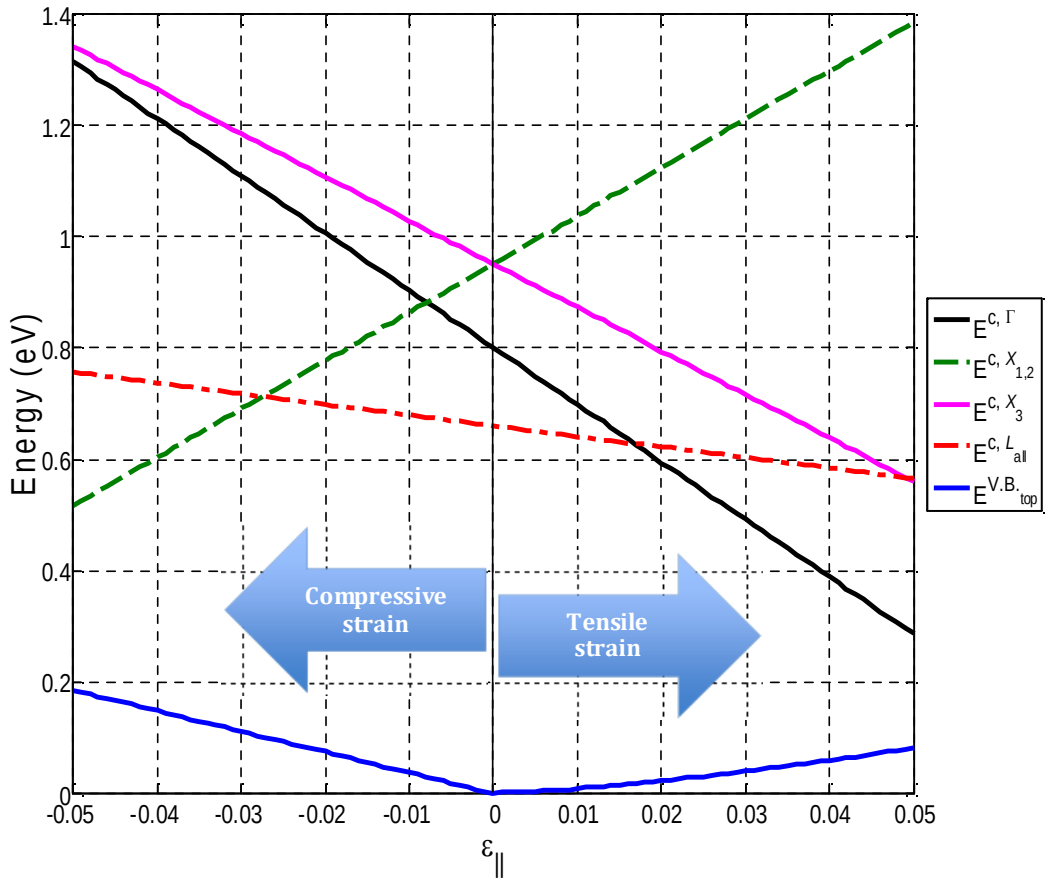

Figure 2.5: The energy of the conduction bands bottom of k-valley (E^{c,k_i}) and the top of the valence band ($E^{\text{V.B.top}}$) of biaxially strained [001] bulk Ge.

$$\Delta E^{\Gamma}_{[110]B} = \Xi^{\Gamma}_{d} \frac{C_{11} - C_{12} + 6C_{44}}{C_{11} + C_{12} + 2C_{44}} \varepsilon_{||}. \tag{2.49}$$

All of the degenerate L valleys will be shifted according to

$$\Delta E^{L_{1,2}}_{[110]\text{B}} = \frac{12C_{44}\Xi^{L}_{d} - 2\left(C_{11} + 2C_{12} - 2C_{44}\right)\Xi^{L}_{u}}{C_{11} + 2C_{12} + 4C_{44}} \varepsilon_{||}, \tag{2.50}$$

$$\Delta E^{L_{3,4}}_{[110]\text{B}} = \frac{2}{3} \frac{\left(C_{11} + 2C_{12} + 6C_{44}\right)\Xi^{L}_{d} + 18C_{44}\Xi^{L}_{u}}{C_{11} + 2C_{12} + 4C_{44}} \varepsilon_{||}. \tag{2.51}$$

But the degeneracy will be lifted for X-valleys, and their shifts of energy are

$$\Delta E^{X_{1,2}}_{[110]\mathrm{B}} = \frac{\left(C_{11} - C_{12} + 6C_{44}\right)\Xi^X_d - \left(C_{12} - 2C_{44}\right)\Xi^X_u}{C_{11} + C_{12} + 2C_{44}}\varepsilon_{||}, \tag{2.52}$$

$$\Delta E^{X_3}_{[110]\mathrm{B}} = \left(\frac{C_{11} - C_{12} + 6C_{44}}{C_{11} + C_{12} + 2C_{44}}\Xi^X_d + \Xi^X_u\right)\varepsilon_{||}. \tag{2.53}$$

The energy shift for conduction band valleys bottom and the valence band top dependence as a function of biaxial strain for Ge grown in [110] crystal orientation are shown in fig. (2.6). The degeneracy is lifted in the indirect C.B. valleys L and X. The L valleys split into two double folded degenerate $L_{1,2}$ and $L_{3,4}$. The X valleys split into four fold degenerate $X_{1,2}$ valleys, and double degenerate X_3 valleys. The split valleys behave differently with the applied strain.

Biaxial strain in the [111] growth direction

The resultant strain tensor in the [111] growth orientation is

$$\varepsilon_{[110]\mathrm{B}} = \frac{\varepsilon_{||}}{C_{11} + C_{12} + 2C_{44}} \begin{bmatrix} 2C_{44} - C_{12} & -C_{11} - 2C_{12} & 0 \\ -C_{11} - 2C_{12} & 2C_{44} - C_{12} & 0 \\ 0 & 0 & C_{11} + C_{12} + 2C_{44} \end{bmatrix}. \tag{2.54}$$

The shift in the energy of the Γ valley is

$$\Delta E^{\Gamma}_{[111]\mathrm{B}} = \frac{12C_{44}}{C_{11} + C_{12} + 4C_{44}}\Xi^{\Gamma}_d\varepsilon_{||}, \tag{2.55}$$

The shift in energy of the X-valleys is

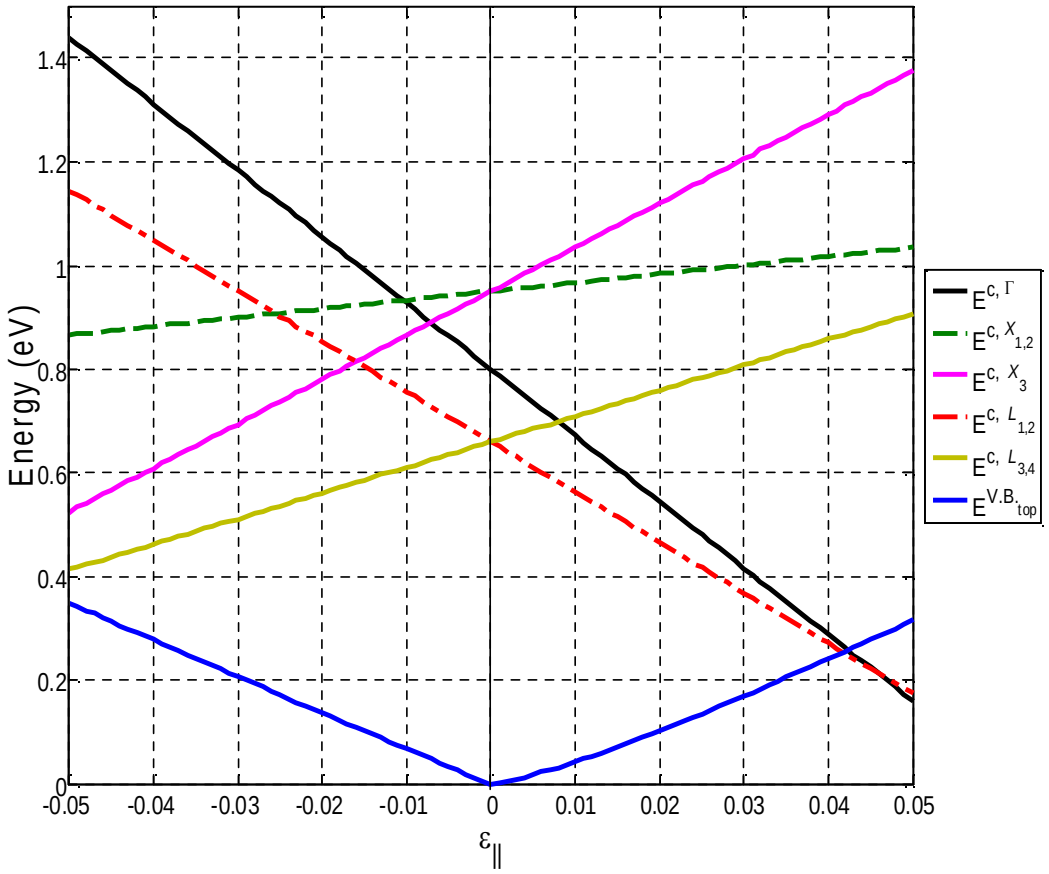

Figure 2.6: For biaxially strained [110] bulk Ge, The energy of the conduction band bottom of k-valley (E^{c,k_i}) and the top of the valence band ($E^{\mathrm{V.B.top}}$) as a function of (tensile and compressive) strain.

$$\Delta E^{X}_{[111]\mathrm{B}} = 4C_{44}\frac{3\Xi^{X}_{d} + \Xi^{X}_{u}}{C_{11} + 2C_{12} + 4C_{44}}\varepsilon_{||}. \tag{2.56}$$

The degenerate L valleys will be shifted according to

$$\Delta E^{L_1}_{[111]\mathrm{B}} = \frac{12C_{44}\Xi^{L}_{d} - 2\left(C_{11} + 2C_{12} - 2C_{44}\right)\Xi^{L}_{u}}{C_{11} + 2C_{12} + 4C_{44}}\varepsilon_{||}, \tag{2.57}$$

$$\Delta E^{L_{2,3,4}}_{[111]\mathrm{B}} = \frac{2}{3}\,\frac{18C_{44}\Xi^{L}_{d} + \left(C_{11} + 2C_{12} + 6C_{44}\right)\Xi^{L}_{u}}{C_{11} + 2C_{12} + 4C_{44}}\varepsilon_{||}. \tag{2.58}$$

For Ge grown in the [111] crystal direction, fig (2.7) shows the energy shift for the conduction band valleys minimum and the valence band top. The X-valleys remain degenerate while it is lifted in the L-valleys.

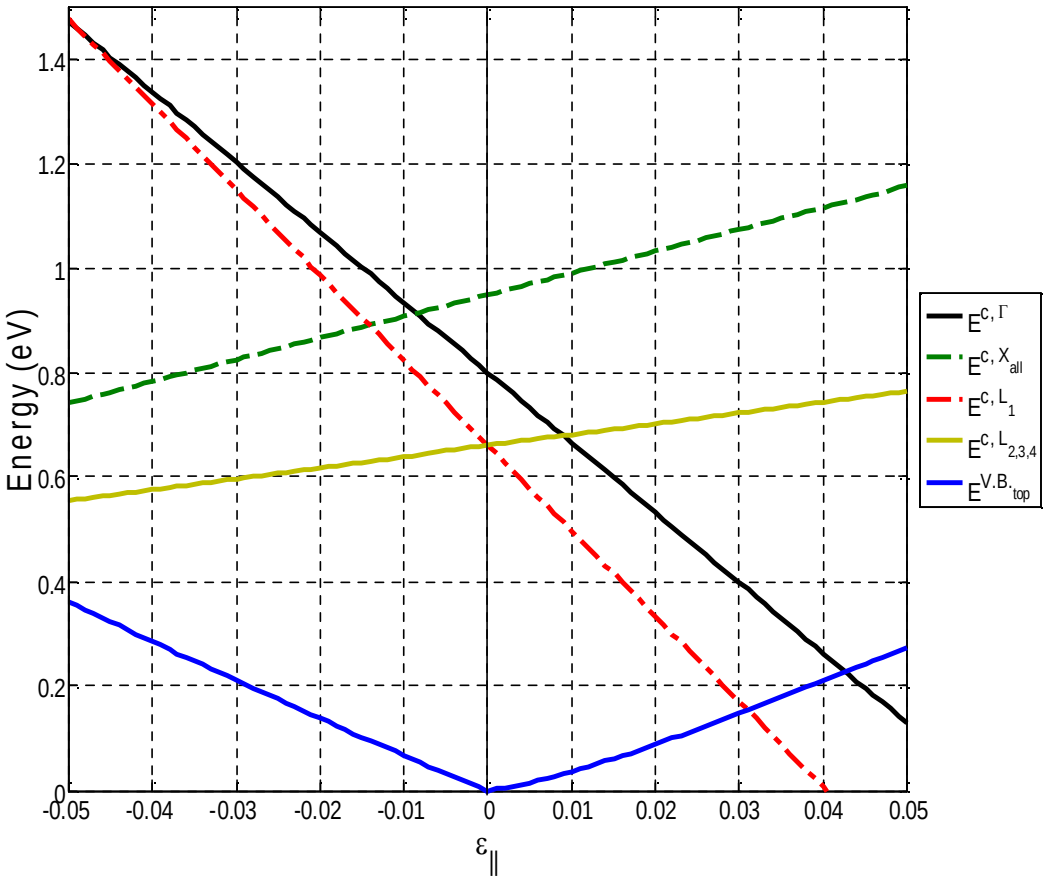

Figure 2.7: For biaxially strained [111] bulk Ge, The energy of the bottom of the conduction bands of k-valley (E^{c,k_i}) and the top of the valence band ($E^{V.B._{top}}$) as a function of applied tensile and compressive.

2.7.2 *The V.B. top*

The calculations of the V.B. maximum have been performed for bulk Ge under the same applied strain condition mentioned above in this section. The

blue line in figures (2.5, 2.6 and 2.7) shows the energy of the top of the V.B. as a function of strain for Ge grown in [001], [110] and [111] orientations, respectively.

2.8 DISCUSSION

For bulk-like Ge, the conduction band bottom of valley (k) and the top of the valence band change when biaxial strain is applied in [001], [110], and [111] growth directions. When [001] Ge is subject to biaxial strain (compressive and tensile), the conduction band at Γ, the four degenerate L-valleys, and the twofold degenerate X-valleys (X_2) have negative slope (the energy decreases with tensile and increase with compressive strain) but the fourfold degenerate X-valleys along $X_{1,3}$ have positive slope (the energy increases with tensile and decreases with compressive strain) as shown in fig. 2.5 .

The Γ-valley has the largest negative slope in [001] Ge, and has the largest energy with more than 1 % compressive strain in [110] and [111] Ge. Ge becomes direct band gap at biaxial tensile strain 1.7 % in [001] Ge. The degenerate L-valleys split in [110] Ge into two fourfold groups, $L_{1,2}$ with negative slope and $L_{3,4}$ with positive slope, and in [111] Ge split into twofold degenerate L_1 with negative slope and sixfold degenerate $L_{2,3,4}$ with positive slope. The degenerate X-valleys split in [110] Ge as in [001] Ge, all X-valleys have positive slope; they do not split in [111] Ge and have positive slope, see figs. (2.5-2.7). Ge has zero band gap in [110] and [111] Ge for around 4.3 and 3.1 % tensile strain, respectively.

The degeneracy of HH and LH is lifted when biaxial strain is applied. The LH (HH) is the highest in biaxially tensile (compressive) strained [001] bulk Ge, while the HH (LH) is the highest in the other cases with applied tensile (compressive) strain for [110] and [111] Ge. Since they have the opposite

behaviour with the applied strain a broken line of the energy shift of the valence band maximum can be seen, in figures 2.5 - 2.7. The top of the valence band increases more for compressive than for tensile strain for all cases ([001], [110] and [111] Ge). However, the rate of increase for both types of strain is larger in [110] than in [111] and [001] bulk Ge.

2.9 CONCLUSION

In this chapter, a concise background theory has been given about the properties of Ge as semiconductor material. Two methods to obtain the $E - k$ relation for Ge have been described. The effects of strain calculations were then performed to investigate the variation of the energy bands for Ge grown in different orientations, and under different strain conditions. Our calculations show that the direct C.B. edge energy increases with the applied compressive strain and decreases with tensile strain for bulk Ge grown in all three orientations. The [001] orientation has moderate energy shift for the applied biaxial tensile strain than the [110] and [111], for bulk Ge. The degeneracy of the indirect C.B. valleys (L and X) is lifted with applied strain for certain growth orientations of the Ge layer. The energy shifts of non-degenerate indirect valleys have different behaviour with strain. The 1.7 % biaxially tensile strained [100] Ge is best for achieving a direct band gap amongst the three growth orientations. The rate of change of the valence band maximum is different for each growth direction. The valence band maximum increases more with both compressive than with tensile strain.

3

INJECTION EFFICIENCY OF BULK GE AND GE QUANTUM WELL

3.1 INTRODUCTION

Ge is the most interesting group IV semiconductor material for light emitting processes. Emitted light from direct band gap (Γ-valley) transitions in Ge is in the near infrared wavelength range. Achieving this process from the direct band gap in Ge is difficult due to the fact that the direct band gap is $\sim 140\,\text{meV}$ above the indirect band gap at room temperature [25].

As mentioned in chapter (2), the band structure of Ge can be engineered by varying strain conditions. Strain can result in changes to the direct band gap energy. Shifting and splitting of degenerate equivalent indirect valleys (X and L), and also shifting of the valence band top can occur. These changes depend on the type of applied strain and its direction, as well as the substrate orientation [25, 68], see figures (3.1a and 3.1b). The n-type doping for bulk or strain Ge can reduce the energy separation between the direct and the indirect conduction band valleys [8]. These methods which have been proposed to tune the Ge band structure to achieve a direct band gap material will be introduced briefly and discussed in the following sections.

This chapter investigates the effect, at low temperature, of the different tensile strain conditions (biaxial, or uniaxial along particular axes) on the direct band gap energy reduction. Detailed expressions for the strain tensor and the C.B and V.B. valleys shifts with the applied uniaxial strain along particular axes at Appendix A. Then the doping requirements, of bulk Ge and Ge quantum wells grown on [001], [110] and [111] oriented substrates and subjected to different types of tensile strain. After that, the fraction of the injected carriers (the injection efficiency) which reside in the direct valley and therefore contribute to direct transitions and optical gain is calculated, in order to find optimum strain conditions for bulk or quantum well active layers of near infrared Ge lasers.

3.2 GE AS DIRECT BAND GAP MATERIAL

Two methods have been proposed to tune the Ge band structure to achieve a direct band gap material. Introduce optimized strain condition for a given growth orientation in choosing growth orientation. The second method is to introduce heavy *n*-type doping to fill all indirect valleys has energy below the energy of the Γ-point in Ge, at low temperature.

3.2.1 *Tensile strained Ge*

In chapter 2, calculation shows that at about 1.7 % biaxial tensile strain [001] Ge becomes a direct band gap material. That leads to more electrons populating the Γ valley of the conduction band. Therefore, the direct band recombination transition becomes more efficient which is a major advantage of strained germanium. Yet the direct band gap in Ge shrinks due to the increase in the valence band top and decrease in the Γ valley with tensile strain.

3.2.2 *Heavily n-type doped Ge*

For n-type doped semiconductor material, the excess electrons populate the lowest conduction band valley first at low temperature. In n-type bulk Ge the indirect L valleys will be filled first before the direct Γ valley. By filling all indirect valleys below the bottom of the Γ-valley Ge can behave like a direct band gap semiconductor. Any further electrons injected into the material will have a significant probability of occupying Γ valley state, depending on the relative densities of states in the Γ and L valleys at the relevant electron energy. Figure (3.1a) shows a schematic diagram of the band structure for bulk Ge and how the heavy n-type doping makes Ge effectively a direct band gap material, fig. (3.1c). At finite temperatures, the electrons have more possibility to be thermally distributed in the L valleys of the conduction band, and hence the effect is less strong.

Combining moderate tensile strain and n-type doping will result in less doping required to fill all the indirect valleys below the Γ valley minimum, at low temperature [8]. Further detailed discussion later on in this chapter is about obtaining Ge as direct band gap material for bulk like and quantum well structure.

3.3 THEORY

Because of the indirect gap an amount of electrons must be supplied by doping to enhance the direct transitions. After applying a strain to the semiconductor material (Ge), the energy shifts of each valley can be calculated as described in chapter 2, and then used to determine the electron density in different valleys. In this section a background theory is given about calculating the electron doping density required to fill all the energy states of indirect valleys below the energy bottom of Γ-valley, and about finding the

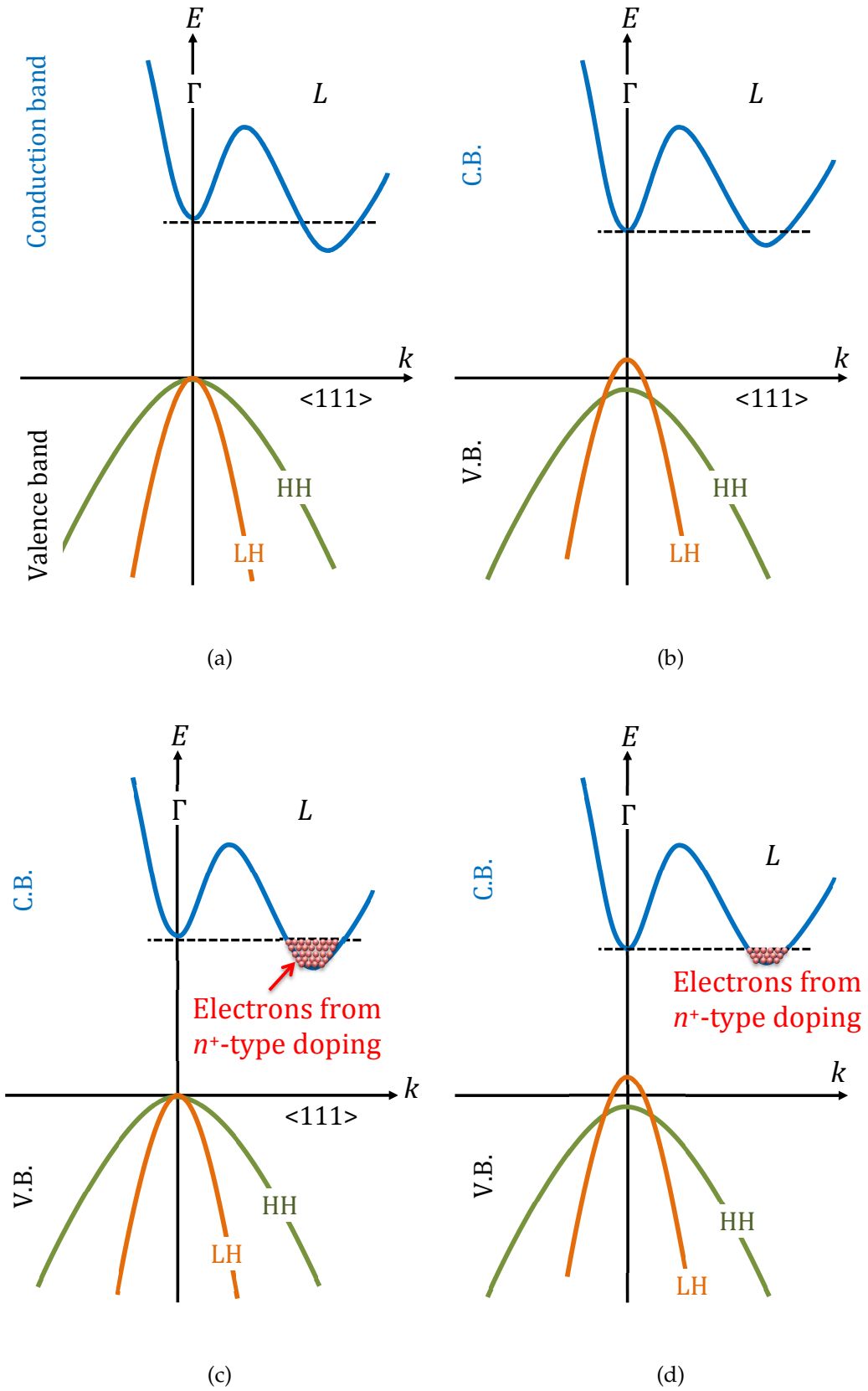

Figure 3.1: Schematic of the band structure for four different cases of Ge, (a) Bulk Ge, (b) Tensile strained intrinsic [001] Ge, (c) n^+-type doped Ge, and (d) n^+-type tensile strained [001] Ge, after ref. [8].

excess effective injected carrier density that populate the Γ-valley for bulk Ge and Ge QW, at low temperature.

3.3.1 *The doping density and the Fermi level in semiconductors*

A bulk-like layer and a very thin layer were considered in this investigation, both at very low temperature.

3.3.1.1 *Bulk case (3D)*

For bulk-like layers, the relation between the electron density (n_{3D}) in a valley and the Fermi level (E_F) measured from the conduction band bottom of valley (k) is:

$$E_F = \frac{\hbar^2 \left(3\pi^2 n_{3D}\right)^{2/3}}{2m_{3D}}, \tag{3.1}$$

at very low temperatures ($T \approx 0\,\mathrm{K}$), where m_{3D} is the 3-dimensional density of states effective mass [82]. In thermal equilibrium, E_F is the same for all valleys. Under strain, the energy of the Γ, X and L valleys may change differently. For strained bulk Ge, the electron density in the presence of strain for valley k, in low temperature limit [90], is:

$$n_{3D}^{\mathrm{k}} = \frac{2^{3/2}}{3\pi^2\hbar^3} \sum_{i=1}^{\ell} \left[m_{3D}^{\mathrm{k}} \left(E_F - E^{\mathrm{c,k}_i} \right) \cdot \theta \left(E_F - E^{\mathrm{c,k}_i} \right) \right]^{3/2}, \tag{3.2}$$

where ℓ is the number of equivalent valleys and $\theta(x)$ is the Heaviside function:

$$\theta(x) = \begin{cases} = 1 & \text{for } x \geq 0 \\ = 0 & \text{for } x < 0 \end{cases}. \tag{3.3}$$

The $3D$ density of states mass (m_{3D}^{k}) of valley (k) depends on the longitudinal and transverse masses for valley k as:

$$m_{3D}^{k} = \sqrt[3]{m_{l}^{k} \cdot m_{t}^{k2}}, \tag{3.4}$$

where m_{l}^{k} and m_{t}^{k} are the longitudinal and transverse mass for valley (k) [90, 82], see Table (3.1).

Table 3.1: The longitudinal and transverse mass values of valley (k) in Ge in terms of the free electron mass [21, 22].

k	m_l	m_t
Γ	0.041	0.041
L	1.64	0.08
X	0.95	0.20

Setting the Fermi level equal to the Γ-valley bottom ($E^{c,\Gamma}$) in eq. (3.2), gives the electron density (N_{3D}) in bulk Ge that is required to fill all indirect valleys up to the lowest available energy in the Γ-valley, for the particular strain condition and growth orientation:

$$N_{3D} = \sum_{k}^{\Gamma,L,X} n_{3D}^{k}. \tag{3.5}$$

3.3.1.2 *Quantum well case (2D)*

In the case of a very thin layer, with width d, embedded in high barriers (strong quantization), the energies of the quantized states, measured from the bottom of a valley (k) in the thin layer (quantum well) material, are:

$$E_j = \frac{\pi^2 \hbar^2}{2 m_z d^2} \cdot j^2, \qquad j = 1, 2, 3 \ldots; \tag{3.6}$$

so each valley has its own set of quantized states, their energy depending on the effective mass component m_z [90]. For a particular valley, for a quantized state j (with energy E_j) the relation between the $2D$ electron density and Fermi level (E_F) is

$$\begin{aligned} n_{2D} &= \frac{m_{2D}k_BT}{\pi\hbar^2}\ln\left(1+\exp\left(\frac{E_F-E_j}{k_BT}\right)\right) \\ &\underset{T\to 0}{\approx} \frac{m_{2D}}{\pi\hbar^2}\cdot\left(E_F-E_j\right)\cdot\theta\left(E_F-E_j\right). \end{aligned} \tag{3.7}$$

In thermal equilibrium, the electron density for a very thin layer in all quantized states of valley k, in the low-temperature limit, is given by:

$$n_{2D}^{\mathrm{k}} = \frac{1}{\pi\hbar^2}\sum_i^{\ell}\sum_j\left[m_{2D}^{\mathrm{k}_i}\left(E_F-E_j^{\mathrm{c,k}_i}\right)\cdot\theta\left(E_F-E_j^{\mathrm{c,k}_i}\right)\right]^{3/2}, \tag{3.8}$$

where m_{2D} is the density of states mass for that valley [90], which depends on the orientation of a particular valley (k_i) in respect to the layer orientation for X and L-valleys and it is given by:

$$m_{2D}^{\mathrm{k}_i} = \sqrt{\frac{\left(m_{3D}^{\mathrm{k}_i}\right)^3}{m_z^{\mathrm{k}_i}}}. \tag{3.9}$$

Unlike m_{3D} which depends on the type of valley (k), the m_z and m_{2D} depend on the orientation of a particular valley (k_i) in respect to the layer orientation. Only in the case of the Γ valley is it independent of orientation (the Γ-valley only has one scalar effective mass, $m^{\Gamma} = m_l = m_t$) [82, 90]. The effective mass (m_z) perpendicular in the direction to the crystal surface, for the L and X valleys for different growth directions shown in Table (3.2). In this work the modelling does not take into account the case when the conduction band minimum overlaps with the valence band maximum.

Table 3.2: The effective mass m_z perpendicular in the direction to the crystal surface, for the L and X valleys for different orientations [23, 24].

Growth orientation	$m_z^{L_i}$	L_i	$m_z^{X_i}$	X_i
[001]	$\frac{3m_tm_l}{m_t+2m_l}$	L_{all}	m_l	X_3
			m_t	$X_{1,2}$
[110]	$\frac{3m_tm_l}{m_t+2m_l}$	$L_{1,2}$	$\frac{2m_tm_l}{m_t+m_l}$	$X_{1,2}$
	m_t	$L_{3,4}$	m_l	X_3
[111]	m_l	L_1	$\frac{3m_tm_l}{m_t+2m_l}$	X_{all}
	$\frac{9m_tm_l}{m_t+8m_l}$	$L_{2,3,4}$		

Setting the Fermi level equal to the energy of the lowest quantized state of a Ge quantum well ($E_1^{c,\Gamma}$) in eq. (3.8), gives the electron density (N_{2D}) in a Ge quantum well required to fill all indirect quantized state in valleys up to the lowest available energy in the Γ-valley, for the particular strain conditions:

$$N_{2D} = \sum_{k=1}^{\Gamma,L,X} n_{2D}^{k}. \tag{3.10}$$

3.3.2 *Injection efficiency*

For the two cases of heavily doped tensile strained Ge (bulk-like or quantum well), any excess injected electrons will then populate both the L and Γ valleys, according to the (energy-dependent) distribution of the density of states. The efficiency with which the injected electrons populate the Γ-valley, for n^+ doped strained bulk Ge under quasi-equilibrium conditions, is given by:

$$\sigma_{bulk}^{\Gamma} = \frac{\triangle n_{3D}^{\Gamma}}{\triangle n_{3D}^{\Gamma} + \triangle n_{3D}^{L} + \triangle n_{3D}^{X}}, \tag{3.11}$$

where $\triangle n_{3D}^{k}$ is the portion of the total excess (injected) electron density which resides in valley k of the strained doped bulk Ge. An equivalent expression is used for the case of Ge quantum wells (with $\triangle n_{3D}^{k}$ replaced by $\triangle n_{2D}^{k}$) [10].

3.4 RESULT AND DISCUSSION

Biaxial and uniaxial tensile strained Ge layers, grown in the conventional [001], [110] and [111] directions have been considered in this calculation. For the uniaxial strain case, the strain was directed along the [100] crystallographic axis for [001] growth, along the $x' = [001]$ or $y' = [\bar{1}10]$ crystallographic axes for [110] growth, and along the $x' = [\bar{1}10]$ or $y' = [11\bar{2}]$ crystallographic directions for [111] growth, see Appendix A. The necessary material parameters were obtained from refs. [20, 45, 91].

3.4.1 *The Γ-point band gap shrinkage*

It has been shown previously how the conduction band valleys behave under different strain conditions and since the energy of the top of the valence band increases with the applied strain (compressive and tensile). The overall change of the band gap at the Γ-point with tensile strain for different substrate orientations is shown in fig. (3.2).

The Γ-point direct band gap of biaxially tensile strained [110] and [111] Ge shows a stronger dependence on strain than in other cases, yet the biaxial tensile strain for [001] Ge growth is clearly the best choice, and can be achieved epitaxially, or by tunable (e.g. membrane deformation) techniques.

In contrast, uniaxial strain is less effective, especially for [110] Ge along the x'axis, although it is easier to achieve in its tunable variant, *e.g.* by plate or beam bending. In either case, however, the required strain is quite large, and can be applied only to very thin Ge layers, below the critical thickness for elastic deformation.

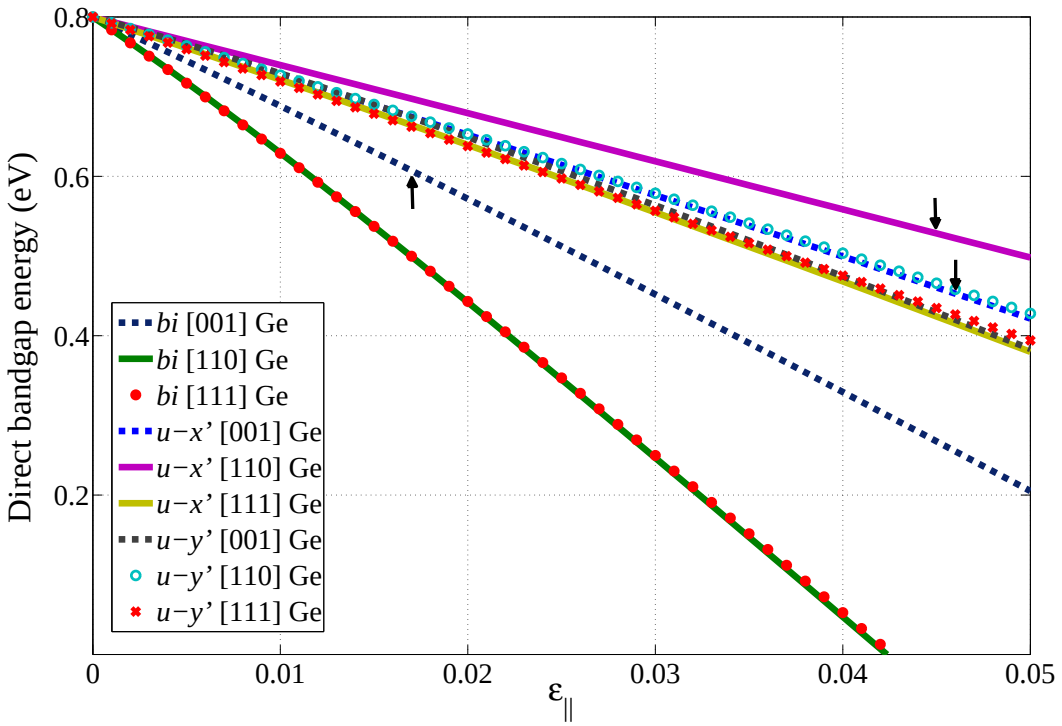

Figure 3.2: The variation of the direct band gap with the applied biaxial (*bi*), or uniaxial strain along x'- (*u*-x') and y'axis (*u*-y'), for Ge grown in different orientations. The black arrows indicate the critical strain values where Ge becomes direct band gap [9, 10].

3.4.2 *The required n-type doping density to compensate the energy difference*

For moderate values of strain, while Ge still has an indirect gap, appropriate doping can be used to fill all indirect-valley states up to the Γ-valley minimum, in order to enable a population inversion based on additionally injected electrons. This required *n*-type doping density will be calculated for the previous mentioned cases of growing bulk like Ge and Ge quantum wells in different directions and under variant tensile strain cases.

3.4.2.1 *Bulk like Ge*

The doping density required to fill the indirect valleys up to the Γ valley minimum , at low temperature is shown in fig. (3.3). Results are shown for biaxially and uniaxially strained bulk Ge grown on [001], [110] and [111] orientations. Clearly, the [001] growth is no longer the best option in this approach for moderate values of tensile strain (likely to be achievable in most realistic structures). Biaxially strained [110] and [111] Ge require a lower *n*-type doping density than other cases, especially compared to the [001] case.

3.4.2.2 *Ge quantum wells*

At low temperature and in the strong quantization limit, the strain-dependent doping density required to fill all indirect valley quantized states up to the lowest Γ-valley quantized state in $d = 10\,\text{nm}$ and $20\,\text{nm}$ wide Ge quantum wells was calculated for the same previous strain conditions and substrate orientations. As shown in figs. (3.4) and (3.5), biaxial tensile strain again requires a lower doping density than uniaxial tensile strain. The [111] Ge performs better than the other orientations at strain values less than 1.4 %.

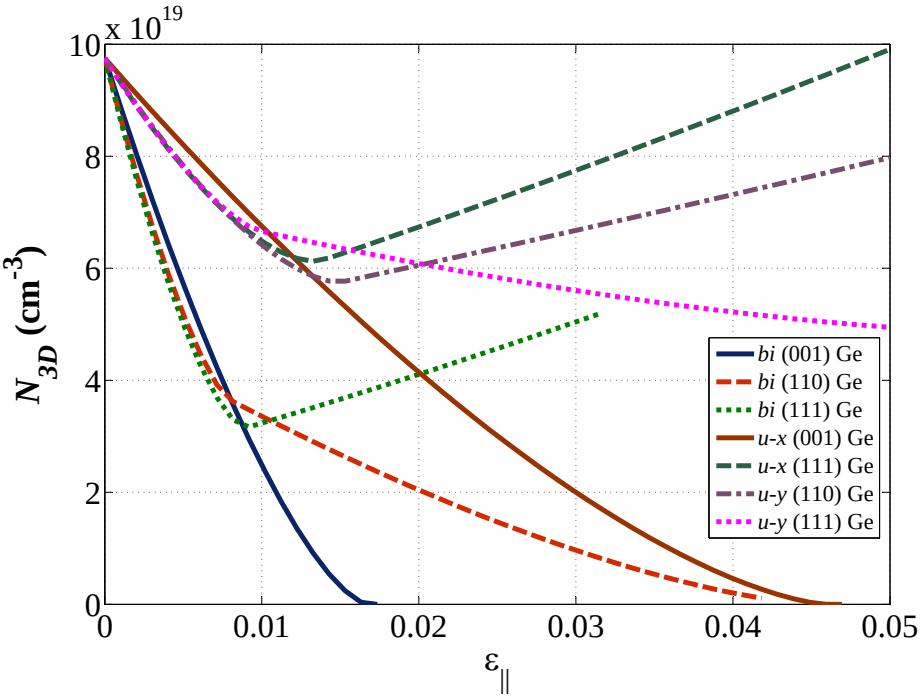

Figure 3.3: The variation of the doping density required for band-filling up to the Γ minimum (N_{3D}) with the applied tensile (biaxial and uniaxial along x' and y'axis) strain: [001], [110] and [111] grown bulk Ge [9, 10].

The variation of the minimum doping density with applied strain is a result of the interplay of various four effects mentioned before. Therefore, the [111] grown 20 nm wide Ge well requires the lowest doping at $\sim 1\,\%$ biaxial tensile strain, an almost fivefold reduction compared to the unstrained system, and a twofold reduction compared to the [001] case. Some other cases of strain conditions have their own optimum strain values, as observed in figs. (3.4 and3.5).

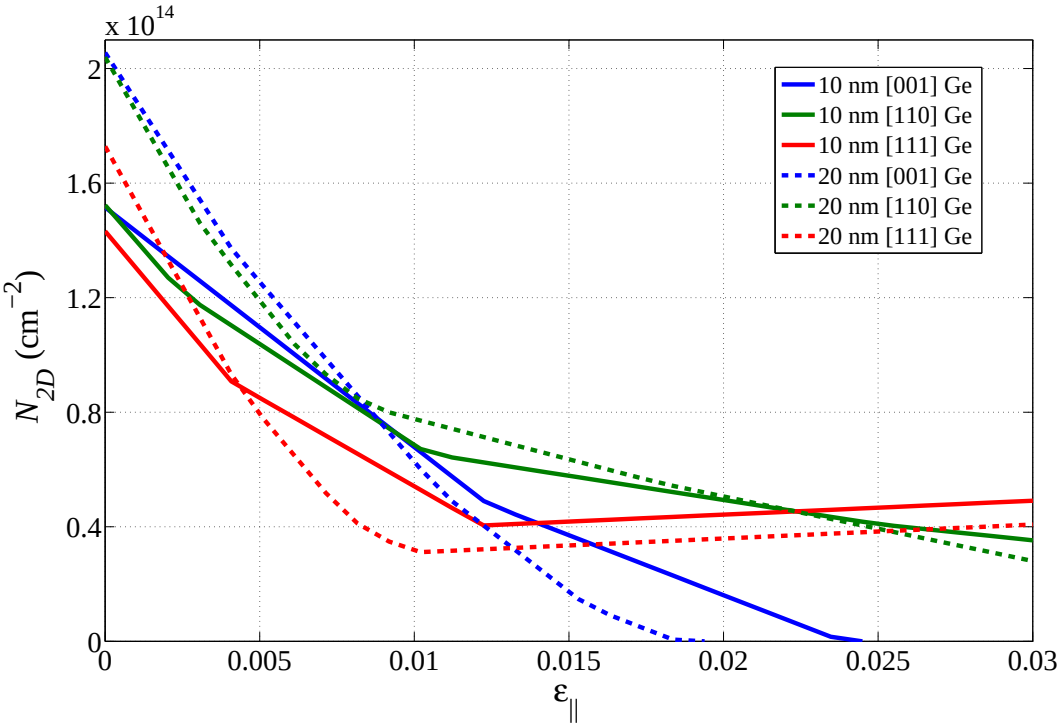

Figure 3.4: The variation of the required doping density (N_{2D}) with applied biaxial tensile strain for [001], [110] and [111] grown 10 and 20 nm thick Ge quantum wells [9, 10].

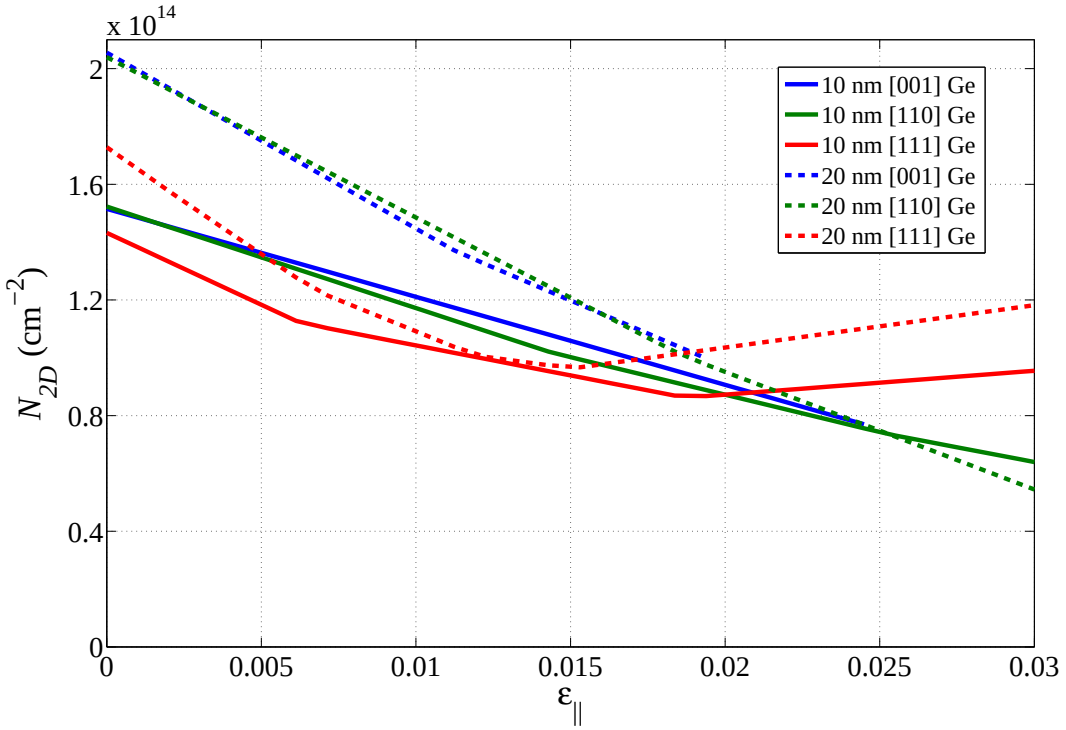

Figure 3.5: The variation of the required doping density (N_{2D}) with applied uniaxial tensile strain along the x'axis for [001], [110] and [111] grown 10 and 20 nm thick Ge quantum wells [9, 10].

3.4.3 *Injection efficiency*

For a strained Ge system which is doped with the required electron density to compensate for the energy difference up to Γ lowest energy state, any additional injected electrons will populate both the L and Γ-valleys, according to the distribution of the density of states. The fraction of the injected electrons residing the Γ-valley may be called the injection efficiency, and increasing its value clearly increases the gain, *i.e.* reduces the threshold current. To assess the injection efficiency behavior in direct band gap doped Ge, the Fermi level in this calculation was set at 10 and 20 meV above the $E^{c,\Gamma}$ and E^{c,Γ_1} for both bulk like Ge and Ge quantum wells, respectively.

3.4.3.1 *Bulk Ge*

The effective mass of density of states of the *L*-valley is larger than the Γ-valley's in Ge. When Ge becomes direct band gap by introducing proper strain and *n*-type doping, a small number of states slightly above the bottom of the Γ-valley compete with the much larger number of states of *L*-valleys at the same energy.

Figure (3.6) illustrates the injection efficiency for doped Ge under different strain conditions for different growth orientations. Biaxially strained Ge is generally more efficient than uniaxially strained Ge; despite the strong shrinkage of the direct band gap mentioned before, [110] and [111] Ge performs better than other cases (and in particular better than [001] Ge) for $< 1.3\,\%$ biaxial tensile strain. When bulk [001] Ge becomes a direct band gap material due to the applied biaxial strain, it acquires the best injection efficiency. For large values of uniaxial strain ($> 3.4\,\%$), which can be achieved practically, the [001] Ge is more efficient than other uniaxially strained cases.

3.4.3.2 *Ge quantum wells*

In contrast to the bulk like case, the case of Ge quantum wells is more favourable for the injection efficiency, because of the step-like energy dependence of the density of states. For 10 and 20 nm wide doped Ge quantum wells the injection efficiency calculations were performed as a function of applied tensile strain. Despite the growth direction, the biaxial strain cases have higher injection efficiency than the uniaxial strain conditions for 10 nm quantum wells. The biaxially strained [111] doped Ge QW generally shows the best efficiency for moderate strain values. The biaxially strained [110] Ge QW has the advantage in the range from 0.25 to 0.44 % for the

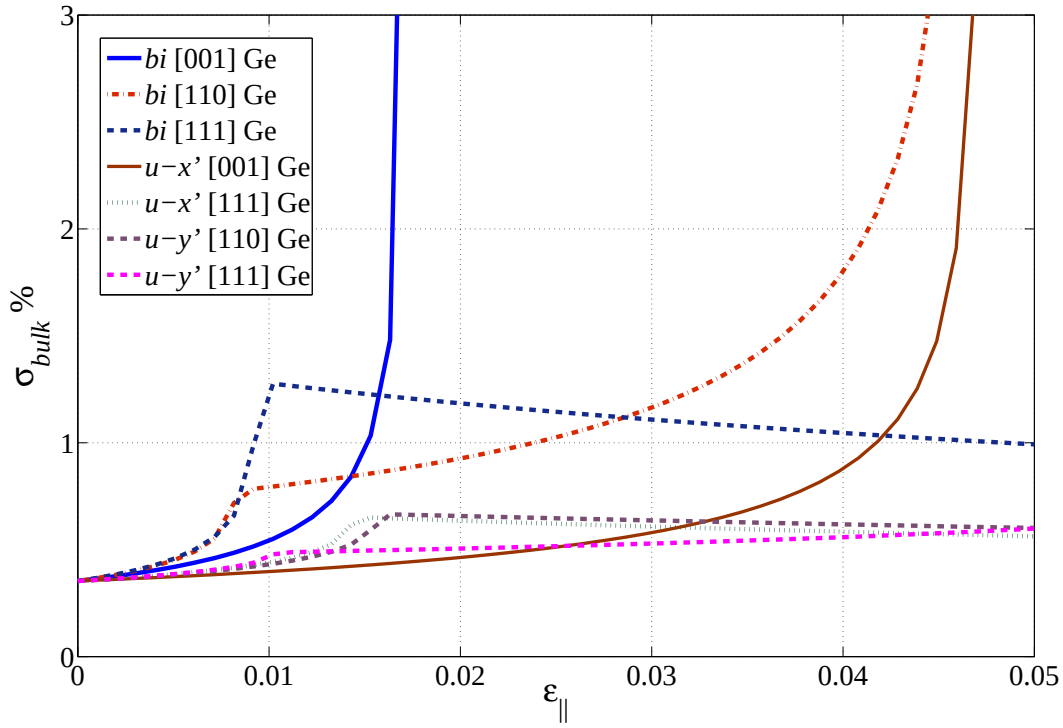

Figure 3.6: Dependence of the electron injection efficiency into Γ-valley of n^+ tensile strained bulk Ge [10].

smaller quantum well width. The efficiency of the biaxially strained [001] Ge QW increases sharply when Ge becomes a direct band gap material. In the 20 nm QW the uniaxial along y'axis gives larger efficiency for very moderate strain values than the biaxially strained [111] Ge QW of the same width.

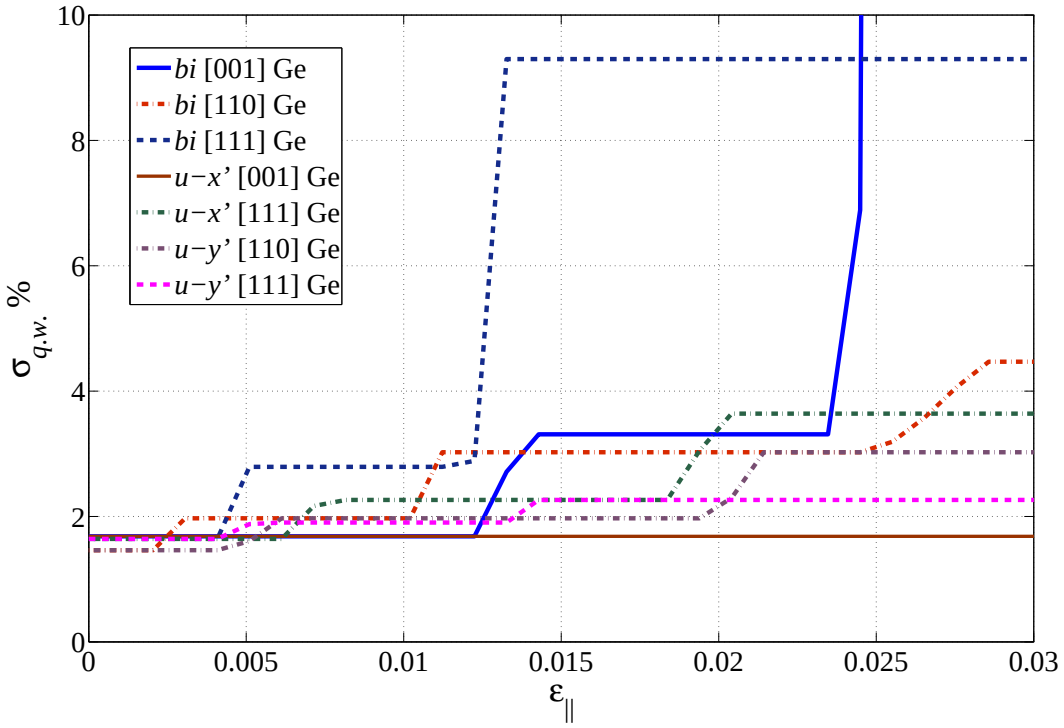

Figure 3.7: Dependence of the electron injection efficiency into Γ-valley of n^+ tensile strained 10 nm wide Ge quantum well [10].

From the calculations performed, for a range of moderate strain the injection efficiency in quantum wells is much larger than for bulk Ge, even though it is still small. Exceeding the doping density required to fill the indirect valleys up to the direct band energy bottom might improve the injection efficiency to Γ-valley, yet that doping is already quite hard to obtain by standards of the present technology.

Furthermore, it should be noted that a small injection efficiency does not necessarily imply a small power efficiency of Ge lasers. Electron recombination lifetime in indirect valleys is orders of magnitude larger than the intervalley scattering time, and if care is taken to prevent escape of indirect electrons to the active layer they will readily refill the Γ-valley states

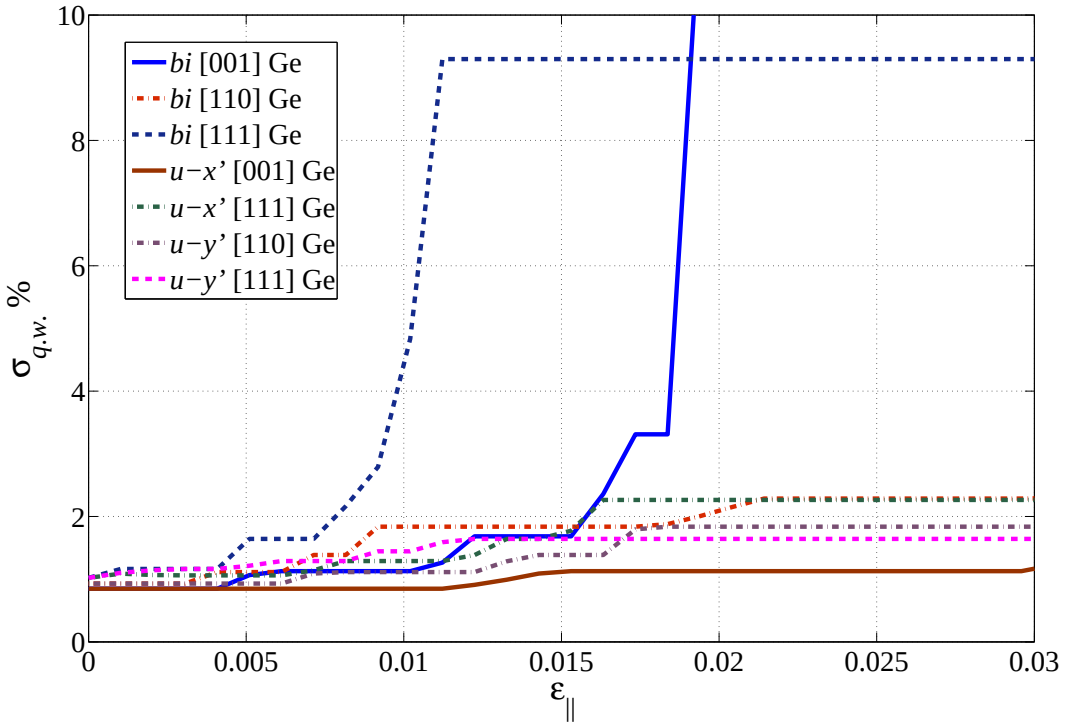

Figure 3.8: Dependence of the electron injection efficiency into Γ-valley of n^+ tensile strained 20 nm wide Ge quantum well [10].

as these become available due to stimulated emission. Therefore, the active layer saturation intensity may be unaffected, but the gain (and threshold current) of Ge laser will clearly be affected by limited injection efficiency.

3.5 CONCLUSION

After finding the required strain conditions for bulk Ge grown in different substrates to make Ge a direct band gap material using the deformation potential method, the doping density required to compensate the energy difference was also obtained using the effective mass method. Calculations have been carried out to investigate the combination of the applied strain and doping density to make Ge behave as a direct band gap of the injection efficiency for both bulk like Ge and Ge quantum wells in forms of different widths.

Despite the fact that the 1.7 % biaxially tensile strained [100] Ge is the best choice for achieving a direct band gap among all the substrate and strain orientations considered, biaxially tensile strained [111] and [110] bulk Ge perform better than [001] grown Ge for moderate strain values ($< 0.8\,\%$ strain) where some doping is required to fill the indirect valleys below the Γ-valley energy bottom. Similarly, for Ge quantum wells, [111] growth is the best option, with an even larger reduction of the required doping density than is achievable in bulk Ge in the range of $1.4\,\% < \varepsilon < 2\,\%$ uniaxial strain, relative to the zero strain case. The shrinkage of the direct band gap is smallest for uniaxially strained [110] Ge, which is therefore the best choice for keeping the emitted wavelength within the communications band. However it requires much larger doping density and large value of uniaxial strain in bulk Ge. The electron injection efficiency into the Γ-valley is much larger for Ge quantum wells than for bulk Ge, and the biaxially strained [111] Ge is generally better in this respect than other cases, but the [110] Ge has the advantage between 0.25 to 0.44% biaxial stain.

The required doping level is found to vary considerably (and generally non-monotonically) with the value of strain, its type and direction. Thus

the electron injection efficiency will vary too. Such behaviour is caused by an interplay of various effects:

1. The degeneracy lifting partially or fully for indirect band gap valleys which were equivalent under no-strain conditions, depending on their orientation in respect to characteristic directions of the system.
2. The energies of new non-degenerate indirect valleys have different dependence on the increasing strain.
3. Only the states below the Γ-valley minimum are relevant, at low temperature.
4. The inequality in the quantization and density of states effective masses for various valley orientations for quantum wells case.

4

GAIN AND INTERVALENCE BAND ABSORPTION FOR BULK Ge

After obtaining the engineered Ge band structure by strain, introducing the injection efficiency as a figure of merit (combining the heavy n-type doping and different strain conditions as a guideline parameter in order to find the optimum conditions for Ge laser operation), and calculating the injection efficiency of bulk Ge and Ge quantum wells at low temperature, in this chapter the optical gain and the intervalley band absorption are calculated and their dependence on strain and carrier density are investigated at finite temperature. Whilst the light-emitting layer in a Ge laser is expected to be n-type doped, to achieve direct-gap-like behaviour, both excess electrons and holes will be injected to operate the device, and the holes will give rise to intervalence band absorption, which can be a significant loss process.

4.1 INTRODUCTION

At finite temperature and under tensile strain, energy bands were calculated using the 8×8 $\mathbf{k}.\mathbf{p}$ method for the conduction and valence bands at the Γ-point, while the effective mass approximation was used for indirect valleys. The quasi-Fermi level was then obtained for specified carrier densities in the conduction and valence bands, E_{Fc} and E_{Fv} respectively,

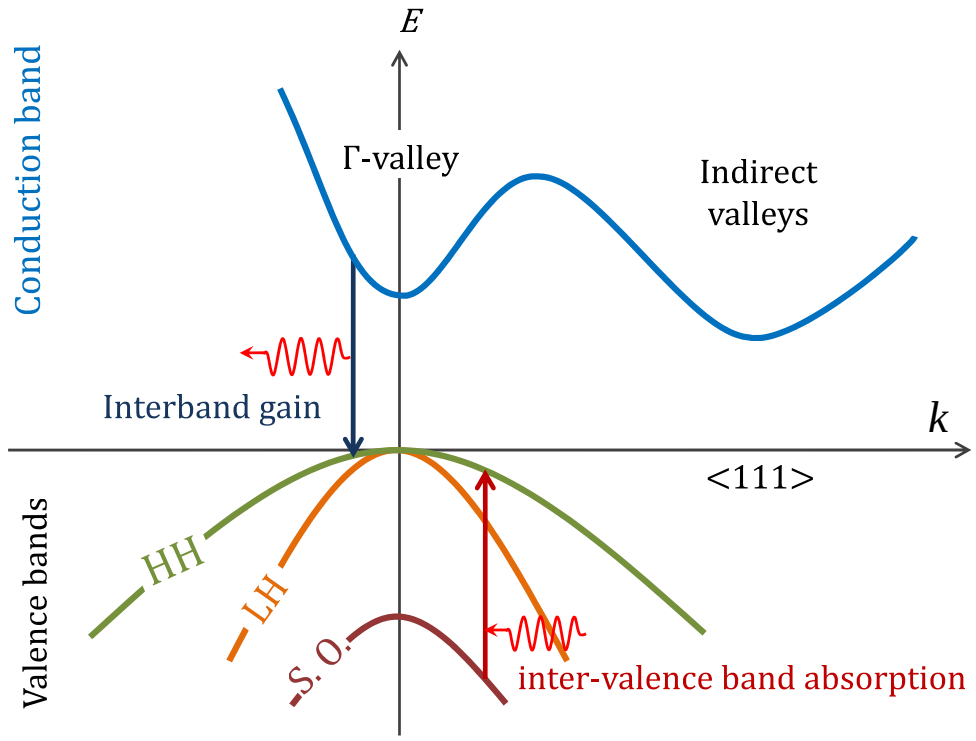

Figure 4.1: Band structure scheme of bulk Ge with transitions between states, leading to interband gain and inter-valence band absorption.

where the carrier density for the bands contains the injected carrier density as well as carriers due to doping. The interband gain spectrum and the inter-valence band absorption (IVBA) were then calculated for this model. These calculations were performed to find the effect of strain conditions, electron and hole densities and temperature on the interband gain and IVBA, and hence on the total gain achievable in n^+ bulk Ge. Figure (4.1) shows a schematic of the interband gain and the IVBA coming from a number of transitions in the band structure of bulk Ge.

The fraction of photons absorbed per unit distance at a photon energy $\hbar\omega$ is defined as the absorption spectrum $\alpha(\hbar\omega)$; the optical gain spectrum $g(\hbar\omega)$ is the negative of the absorption spectrum. For an engineered band structure obtained using the **k.p** method, the electron promotion or demotion transitions are accompanied by photon emission or absorption.

4.2 THE HAMILTONIAN OF ELECTRON-PHOTON INTERACTION

Perturbation theory can be used to calculate the rate of absorption and emission of photons, as the coupling term perturbs the band structure. As discussed previously, the band structure can be obtained for zinc blende crystal structures by solving [84]:

$$H\psi_{nk}(x) = E_n(k)\psi_{nk}(x). \tag{4.1}$$

In time-dependent perturbation theory, the Schrodinger equation becomes:

$$H\psi(\mathbf{r},t) = -\frac{\hbar}{i}\frac{\partial}{\partial t}\psi(\mathbf{r},t), \tag{4.2}$$

where the Hamiltonian (H) here is expanded to an unperturbed time independent Hamiltonian (H_0) and a time dependent perturbation Hamiltonian (H') as

$$H = H_0 + H'(\mathbf{r},t). \tag{4.3}$$

The solution for

$$H_0 = \frac{\mathbf{p}^2}{2m_0} + V(\mathbf{r}), \tag{4.4}$$

has continuous eigenstates, while the perturbation term is

$$H' = -\frac{e}{m_0}\mathbf{A}(\mathbf{r},t).\mathbf{p}, \tag{4.5}$$

where ($\mathbf{A}$) is the assumed vector potential of the electric field, which can be written as

$$\begin{aligned} \mathbf{A}(\mathbf{r},t) &= \hat{e}\mathrm{A}_0 cos(\boldsymbol{k}\cdot\mathbf{r}-\omega t) \\ &= \hat{e}\frac{\mathrm{A}_0}{2}\left(e^{i(\boldsymbol{k}\cdot\mathbf{r}-\omega t)}+e^{-i(\boldsymbol{k}\cdot\mathbf{r}-\omega t)}\right), \end{aligned} \tag{4.6}$$

where $\boldsymbol{k}$ is the wave vector, ω is the optical angular frequency, $\hat{e}$ is a unit vector in the direction of the electric field, and the momentum vector is $\mathbf{p} = -i\hbar\nabla$. The interaction Hamiltonian may be written as:

$$H'(\mathbf{r},t) = H'(\mathbf{r},t)e^{-i\omega t} + H'^{+}(\mathbf{r},t)e^{+i\omega t}, \tag{4.7}$$

where the '+' subscript indicates the Hermitian adjoint operator [84].

4.3 ELECTRON-PHOTON INTERACTION TRANSITION RATE

Between initial and final electron states a and b with energies E_a and E_b respectively, the transition rate T, according to Fermi's golden rule, is given by:

$$T = \frac{2\pi}{\hbar}\left|\left\langle b\left|H'(\mathbf{r})\right|a\right\rangle\right|^2 \delta\left(E_b - E_a - \hbar\omega\right). \tag{4.8}$$

In the steady-state, consider the electron transition rate between a state in the valence band a of energy E_a, and a state in the conduction band b of energy E_b due to absorbing photons with energy $\hbar\omega$, see fig. (4.2) [84]. Each band a and b has a probability of occupancy f_a and f_b respectively, which is been assumed here to be represented by a Fermi-Dirac distribution. For an electron promotion from state a to state b due to photon absorption, the transition rate is proportional to the probability of occupancy f_a of the valence band state, and the probability of a vacancy $(1 - f_b)$ in the

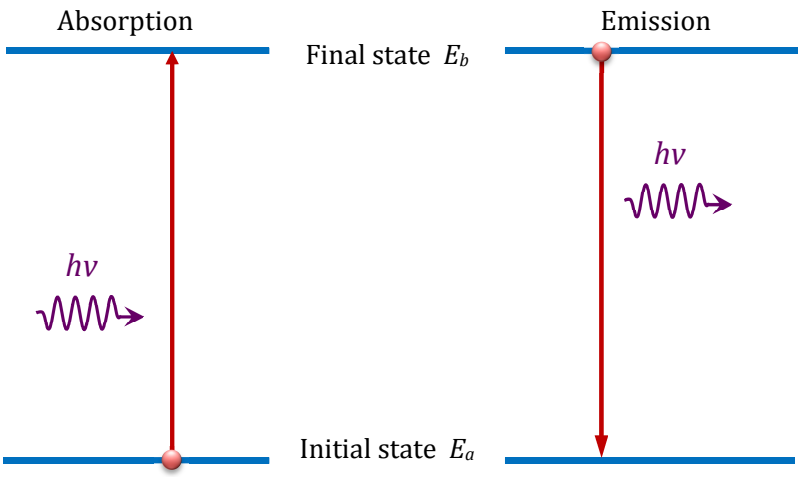

Figure 4.2: The electron transitions due to photon absorption (right) and emission (left), after [11].

conduction band state. The rate of absorption transitions will be therefore given by:

$$W_{abs} = \frac{2\pi}{\hbar} \left| \langle b \left| H'(\mathbf{r}) \right| a \rangle \right|^2 \delta \left(E_b - E_a - \hbar\omega \right) f_a \left(1 - f_b \right). \tag{4.9}$$

The total transition rate per unit crystal volume from occupied lower state a to empty upper state b is

$$R_{a\to b} = \frac{2}{V} \sum_{k_a} \sum_{k_b} \frac{2\pi}{\hbar} \left| H'_{ba} \right|^2 \delta \left(E_b - E_a - \hbar\omega \right) f_a \left(1 - f_b \right). \tag{4.10}$$

The sum here is over all the possible initial and final states, while summing over spin degeneracy has been considered by including the prefactor 2 [84]. The matrix element H'_{ba} is given by

$$H'_{ba} = \langle b \left| H'(\mathbf{r}) \right| a \rangle = \int \Psi_b^* \left(\mathbf{r} \right) H' \left(\mathbf{r} \right) \Psi_a \left(\mathbf{r} \right) d^3\mathbf{r}. \tag{4.11}$$

For an electron initially at the upper state b, the photon emission transition rate between states b and a is given by:

$$W_{emission} = \frac{2\pi}{\hbar} \left|H'_{ba}\right|^2 \delta\left(E_a - E_b + \hbar\omega\right) f_b \left(1 - f_a\right). \tag{4.12}$$

And the total downward transition rate per crystal unit volume in this case is [84]:

$$R_{b\to a} = \frac{2}{V} \sum_{\mathbf{k}_a} \sum_{\mathbf{k}_b} \frac{2\pi}{\hbar} \left|H'^{+}_{ab}\right|^2 \delta\left(E_a - E_b - \hbar\omega\right) f_b \left(1 - f_a\right). \tag{4.13}$$

The net rate of photon transitions between b and a [84] is:

$$\begin{aligned} W\left(\hbar\omega\right) &= W_{absorb} - W_{emission} \\ &= \frac{2\pi}{\hbar} \left|H'_{ba}\right|^2 \delta\left(E_b - E_a - \hbar\omega\right)\left(f_a - f_b\right). \end{aligned} \tag{4.14}$$

And the net transition rate per unit volume can be written as:

$$R\left(\hbar\omega\right) = \frac{2}{V} \sum_{a,b} \frac{2\pi}{\hbar} \left|H'_{ba}\right|^2 \delta\left(E_b - E_a - \hbar\omega\right)\left(f_a - f_b\right), \tag{4.15}$$

using the delta function even-ness property, as $\delta\left(x\right) = \delta\left(-x\right)$ and $H'_{ab} = H'^{+}_{ab}$ [84].

The crystal optical absorption coefficient α is given by:

$$\alpha = \frac{R}{\left(P/\hbar\omega\right)}, \tag{4.16}$$

where R is the number of photons absorbed per unit volume per second, P is the optical intensity and $P/\hbar\omega$ represents the number of injected photons per unit area per second, given by the optical intensity divided by the photon energy [84]. The optical intensity is $P = \frac{1}{2} n_r c \epsilon_0 \omega A_0^2$. Thus:

$$\alpha(\hbar\omega) = \frac{2\hbar\omega R}{n_r c\epsilon_0 \omega A_0^2}. \tag{4.17}$$

The matrix elements can be written in terms of the momentum matrix element [84] as:

$$H'_{ba} = -\frac{e}{m_0} A \bullet \langle b | \mathbf{p} | a \rangle = -\frac{eA_0}{2m_0} \hat{e} \bullet \mathbf{p}_{ba}. \tag{4.18}$$

So the optical absorption coefficient [84] is:

$$\alpha(\hbar\omega) = \frac{\pi e^2}{n_r c\epsilon_0 m_0 \omega} \frac{2}{V} \sum_a \sum_b |\hat{e} \bullet \mathbf{p}_{ba}|^2 \delta(E_b - E_a - \hbar\omega)(f_a - f_b). \tag{4.19}$$

4.4 INTERBAND ABSORPTION AND GAIN FOR BULK SEMICONDUCTOR MATERIAL

The optical matrix element for interband transition between the valence band and conduction band in semiconductor material [84] is given by:

$$H'_{ba} = \left\langle b \left| -\frac{e}{m_0} A(\mathbf{r}) \bullet \mathbf{p} \right| a \right\rangle. \tag{4.20}$$

The vector potential for the optical field is:

$$\mathbf{A}(\mathbf{r}) = \mathbf{A} e^{i\mathbf{k}_{op}\cdot\mathbf{r}} = \hat{e} \frac{\mathrm{A}_0}{2} e^{i\mathbf{k}_{op}\cdot\mathbf{r}}. \tag{4.21}$$

The Bloch functions for electrons in the valence band E_a and the conduction band E_b are given by:

$$\psi_a(\mathbf{r}) = u_v(\mathbf{r}) \frac{e^{i\mathbf{k}_v\cdot\mathbf{r}}}{\sqrt{V}}, \tag{4.22}$$

$$\psi_b(\mathbf{r}) = u_c(\mathbf{r}) \frac{e^{i\mathbf{k}_c \cdot \mathbf{r}}}{\sqrt{V}}, \tag{4.23}$$

where $u_v(\mathbf{r})$ and $u_c(\mathbf{r})$ are the periodic parts of the Bloch function, and the exponentials are the envelope functions for free electrons [84]. The momentum matrix element can be derived as:

$$\begin{aligned} H'_{ba} &= -\frac{eA_0}{2m_0}\hat{e} \bullet \int \psi_b^* e^{i\mathbf{k}_{op}\cdot\mathbf{r}} \mathbf{p} \psi_a d^3\mathbf{r} && (4.24) \\ &= -\frac{eA_0}{2m_0}\hat{e} \bullet \int u_c^*(\mathbf{r}) e^{-i\mathbf{k}_c\cdot\mathbf{r}} e^{i\mathbf{k}_{op}\cdot\mathbf{r}} \\ &\quad \left[\left(\frac{\hbar}{i}\nabla u_v(\mathbf{r})\right) e^{i\mathbf{k}_v\cdot\mathbf{r}} + \hbar\mathbf{k}_v u_v(\mathbf{r}) e^{i\mathbf{k}_v\cdot\mathbf{r}}\right] \psi_a \frac{d^3\mathbf{r}}{V}, && (4.25) \end{aligned}$$

using the approximation

$$\int_V \left[u_c^*(\mathbf{r}) \frac{\hbar}{i}\nabla u_v(\mathbf{r})\right] F(\mathbf{r}) d^3\mathbf{r} \simeq \int_V F(\mathbf{r}) d^3\mathbf{r} \int_\Omega u_c^*(\mathbf{r}) \frac{\hbar}{i}\nabla u_v(\mathbf{r}) \frac{d^3\mathbf{r}}{\Omega},$$

where the integral over $d^3\mathbf{r}$ can be calculated as the product of two integrals, one over the unit cell Ω for the periodic part ($u_c^*(\mathbf{r}) \frac{\hbar}{i}\nabla u_v(\mathbf{r})$) and one over the slowly varying part ($F(\mathbf{r})$) [84].

Then:

$$\begin{aligned} H'_{ba} &\simeq -\frac{eA_0}{2m_0}\hat{e} \bullet \int_\Omega u_c^*(\mathbf{r}) \frac{\hbar}{i}\nabla u_v(\mathbf{r}) \frac{d^3\mathbf{r}}{\Omega} \int_V e^{i\left(-\mathbf{k}_c+\mathbf{k}_{op}+\mathbf{k}_v\right)\cdot\mathbf{r}} \frac{d^3\mathbf{r}}{V} \\ &= -\frac{eA_0}{2m_0}\hat{e} \bullet \mathbf{p}_{cv}\delta_{\mathbf{k}_c,\mathbf{k}_v+\mathbf{k}_{op}} && (4.26) \end{aligned}$$

where the interband momentum matrix element $\mathbf{p}_{cv}$ [84] is given by:

$$\mathbf{p}_{cv} = \int_{\Omega} u_c^* (\mathbf{r}) \frac{\hbar}{i} \nabla u_v (\mathbf{r}) \frac{d^3\mathbf{r}}{\Omega}. \tag{4.27}$$

4.4.1 *k-selection rule*

Due to conservation of momentum, the crystal momentum of an electron in a final state is equal to its initial momentum, plus the photon momentum, is $\hbar\boldsymbol{k}_c = \hbar\boldsymbol{k}_v + \hbar\boldsymbol{k}_{op}$. Since the initial and final electron state momenta are of the order $2\pi a_0^{-1}$ (where a_0 is the lattice constant, and the photon's wavevector magnitude $\sim 2\pi\lambda_0^{-1}$ can be ignored) the equation (4.26) may be written as:

$$H'_{ba} \simeq -\frac{eA_0}{2m_0}\hat{e} \bullet \mathbf{p}_{cv}\delta_{k_c,k_v}, \tag{4.28}$$

which is the $\boldsymbol{k}$-selection rule that restricts the summation to vertical transitions only, for interband optical transitions, see figure (4.3) [84].

The interband momentum matrix element ($\mathbf{p}_{cv}$) depends only on the periodic parts (u_c and u_v) of the Bloch functions and is derived from the optical momentum matrix element ($\mathbf{p}_{ba}$), which in contrast depends on the full wave function [84].

4.4.2 *Optical absorption coefficient*

The absorption coefficient for a bulk semiconductor material, eq. (4.19), using the $\boldsymbol{k}$-selection rule of the matrix element, eq. (4.28), will be

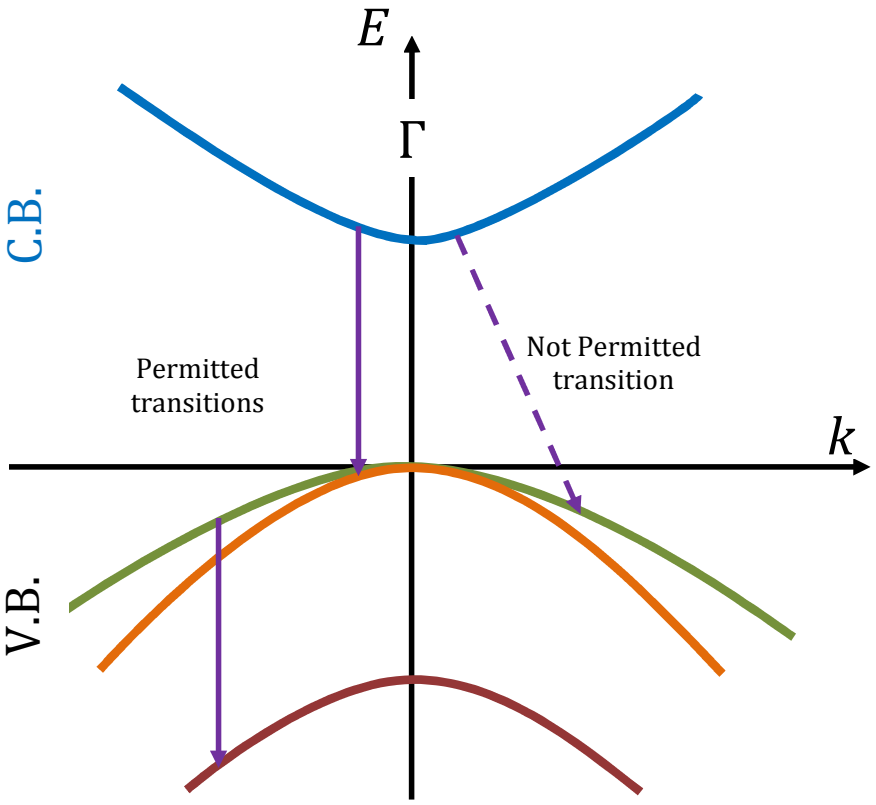

Figure 4.3: Schematic of the permitted and excluded electron-photon transitions between the conduction and valence bands due to the k-selection rule.

$$\alpha\left(\hbar\omega\right) = \frac{\pi e^2}{n_r c \epsilon_0 m_0 \omega} \frac{2}{V} \sum_{\boldsymbol{k}} \left|\hat{e} \bullet \mathbf{p}_{cv}\right|^2 \delta\left(E_c - E_v - \hbar\omega\right)\left(f_v - f_c\right). \tag{4.29}$$

The momentum matrix element $\left|\hat{e}.\mathbf{p}_{cv}\right|^2$ can be determined from the Hamiltonian in the 8×8 $\mathbf{k}.\mathbf{p}$ method for any interband transition.

4.4.3 *Intraband relaxation function*

The delta function can be replaced by a Lorentzian function when the intraband relaxation is included in the absorption spectrum [84], where the Lorentzian function with a Full-width at half-maximum (FWHM) or line width 2γ is

$$\begin{aligned} &\delta\left(E_b - E_a - \hbar\omega\right) \Rightarrow \\ &\quad L\left(E_b - E_a - \hbar\omega\right) \;=\; \frac{\gamma}{\pi\left[\left(E_b - E_a - \hbar\omega\right)^2 + \left(\gamma\right)^2\right]}. \end{aligned} \tag{4.30}$$

4.4.4 *The distribution function*

The occupation probability in both the conduction and the valence bands can be described by a Fermi-Dirac distribution function, given, respectively, as:

$$
\begin{aligned}
f_c(\boldsymbol{k}) &= \left[\exp\left(\frac{E(\boldsymbol{k}) - E_{F_c}}{k_B T}\right) + 1\right]^{-1}, \\
f_v(\boldsymbol{k}) &= \left[\exp\left(\frac{E(\boldsymbol{k}) - E_{F_v}}{k_B T}\right) + 1\right]^{-1}.
\end{aligned}
\tag{4.31}
$$

Here, the quasi-Fermi levels E_{F_c} and E_{F_v} for the conduction and valence bands depend on the doping and carrier injection concentrations. The excitation source, which excites carriers up into the conduction bands (and thus holes into the valence bands), is assumed to be time-independent [92, 84].

4.4.5 *The carrier densities*

The carrier density in a semiconductor material includes the thermal equilibrium carrier density and the excess injected carrier density from external sources, for both electrons and holes, over all conduction and valence bands respectively. The thermal equilibrium electron volume density (n_0) is equal to the thermal hole volume density (p_0) for intrinsic semiconductors and both are equal to the intrinsic carrier volume density (n_i). For n-type and p-type doped semiconductors the carrier densities are equilibrium given by:

$$
n_0 \approx N_D^+ - N_A^- \gg p_0 = \frac{n_i^2}{n_0}, \tag{4.32}
$$

$$
p_0 \approx N_A^- - N_D^+ \gg n_0 = \frac{n_i^2}{p_0}, \tag{4.33}
$$

respectively, where N_D^+ and N_A^- are the ionized donor and acceptor concentrations [82]. Any excess injected carriers will have the same volume

concentration for electrons (δn) and holes (δp). Therefore the total concentrations for electrons and holes in bulk semiconductor are:

$$n = n_0 + \delta n \ , \ p = p_0 + \delta p. \tag{4.34}$$

For bulk Ge, the injected electrons will populate the three conduction band valleys Γ, L, and X, depending on the quasi-Fermi level [82]. The electron concentration for one conduction band valley (k) is expressed as:

$$n^{\mathrm{k}} = \frac{2}{(2\pi)^3} \int \left[\exp\left(\frac{E^{c,\mathrm{k}}(\boldsymbol{k}) - E_{F_c}}{k_B T} \right) + 1 \right]^{-1} d\boldsymbol{k}. \tag{4.35}$$

Since there are four (six) equivalent L (X) valleys for bulk Ge, then the total electron volume density for bulk Ge can be written as:

$$n = n^{\Gamma} + n^{L} + n^{X} = \frac{2}{(2\pi)^3} \sum_{\mathrm{k}} \sum_{i} \int \left[\exp\left(\frac{E^{c,\mathrm{k}_i}(\boldsymbol{k}) - E_{F_c}}{k_B T} \right) + 1 \right]^{-1} d\boldsymbol{k}. \tag{4.36}$$

where (i) indicates the number of equivalent valleys [90].

Similarly, the total hole concentration in the valence band (which has three bands in the case of bulk Ge) is:

$$p = p^{HH} + p^{LH} + p^{SO} = \frac{2}{(2\pi)^3} \sum_{i} \int \left[\exp\left(\frac{E_{F_v} - E^{v,i}(\boldsymbol{k})}{k_B T} \right) + 1 \right]^{-1} d\boldsymbol{k}. \tag{4.37}$$

The quasi-Fermi level can be determined for given total carrier densities using eq. (4.36) and eq. (4.37) [90].

4.5 OPTICAL GAIN COEFFICIENT

In strained bulk Ge (which may be grown in different substrate orientations) the final expression of the direct interband absorption coefficient can be written as:

$$\alpha\left(\hbar\omega\right)=\frac{\pi e^{2}}{n_{r}c\epsilon_{0}\omega m_{0}^{2}}\frac{2}{\left(2\pi\right)^{3}}\sum_{i}\int\left|\hat{e}.\mathbf{p}_{cv_{i}}\right|^{2}\left(f_{v_{i}}\left(\boldsymbol{k}\right)-f_{c}\left(\boldsymbol{k}\right)\right)L_{z}\left(E_{c}-E_{v_{i}}-\hbar\omega\right)\mathrm{d}\boldsymbol{k}. \tag{4.38}$$

The optical gain spectrum $g\left(\hbar\omega\right)$ is the inverse of the absorption coefficient [84].:

$$g\left(\hbar\omega\right)=-\alpha\left(\hbar\omega\right). \tag{4.39}$$

The intervalence band absorption can be calculating using the same formula as for interband absorption, simply by applying the following equation:

$$\begin{aligned}\alpha_{IVBA}\left(\hbar\omega\right) &= \frac{\pi e^{2}}{n_{r}c\epsilon_{0}\omega m_{0}^{2}}\frac{2}{\left(2\pi\right)^{3}}\sum_{j}\sum_{i}\int\left|\hat{e}.\mathbf{p}_{v_{j}v_{i}}\right|^{2}\\ &\quad\left(f_{v_{i}}\left(\boldsymbol{k}\right)-f_{v_{j}}\left(\boldsymbol{k}\right)\right)L_{z}\left(E_{v_{j}}-E_{v_{i}}-\hbar\omega\right)\mathrm{d}\boldsymbol{k},\end{aligned} \tag{4.40}$$

where j here represents the summation over heavy holes, light holes and spin-orbit split off holes, while i is the number of remaining valence bands: $i=2$ when $j=1$ and $i=1$ when $j=2$ [84, 90].

4.6 INTERBAND GAIN CALCULATIONS

The interband gain spectra at room temperature were calculated for unstrained bulk Ge for a range of carrier densities, ranging from $n_{inj} = p_{inj} = 10^{17}$ to $10^{20}\,\mathrm{cm}^{-3}$. The FWHM line width of the Lorentzian lineshape for bulk Ge at room temperature was taken as $\gamma = 6.43\,\mathrm{meV}$ [93]. Since Ge has an indirect band gap, and the injected carrier efficiency calculation shows that only a small ratio of carriers populate the direct valley in the unstrained case, bulk Ge is expected to have no interband gain. However for high carrier density (about $10^{20}\,\mathrm{cm}^{-3}$), from such a point where the injected carrier densities compensates for the energy difference between the direct Γ valley and the indirect L valleys, the carrier population in the Γ-valley is sufficiently high for interband gain to occur, fig. (4.4). The peak gain occurs at a photon energy of 820 meV indicating that the participating carriers lie just above and below the C.B. and V.B. edges.

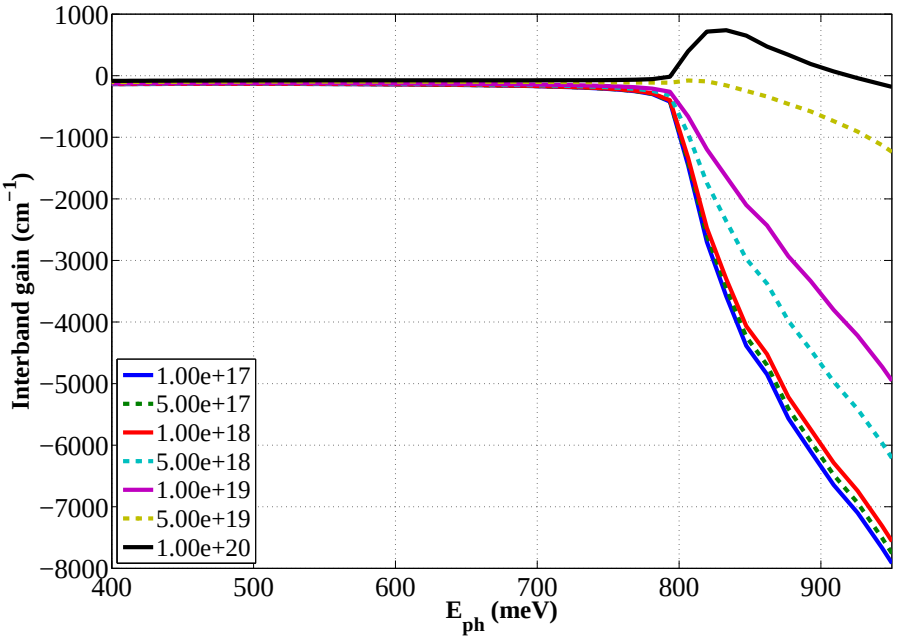

Figure 4.4: Interband gain spectra of bulk Ge for a range of injected carrier densities from $n_{inj} = p_{inj} = 10^{17}$ to $10^{20}\,\mathrm{cm}^{-3}$, at room temperature.

The dependence of interband gain on carrier density and strain will be addressed next.

4.6.1 *Interband gain dependence on strain*

In the conventional [001] growth direction, the direct band gap reduces faster with the applied tensile strain than does the indirect (L-valley) band gap. As a result the energy difference between them decreases, and less n-type doping is required to compensate for this energy gap.

The chosen biaxial tensile strain values for discussion here are the cases of moderate strain at 0.5 %, at 1.0 %, the case of 1.5 % strain which is just insufficient for Ge to acquire a direct band gap and direct band gap Ge at 2.0 % strain. The interband spectra for different carrier injection densities for bulk Ge under 0.5 % biaxial tensile strain are shown in figure (4.5). Such values of strain double the interband gain for a carrier density of $10^{20}\,\mathrm{cm}^{-3}$ at 775 meV, and additionally the optical gain appears at a lower injected carrier density of $5 \times 10^{19}\,\mathrm{cm}^{-3}$ at 750 meV. Interband gain also increases for these two doping densities when the strain is increased to 1.0 %, fig. (4.6). By increasing the biaxial tensile strain to a value of 1.5 %, just before bulk Ge becomes a direct band gap material (where the four equivalent L-valleys are very close to the Γ-valley) an interband gain appears at a injected carrier density of 580 meV for $10^{19}\,\mathrm{cm}^{-3}$, fig. (4.7). After [001] bulk Ge becomes direct band gap at 2.0 % tensile strain, the interband gain significantly increases for the above mentioned injected carrier density and also for $n = 5 \times 10^{18}\,\mathrm{cm}^{-3}$ when the peak gain occurs at 500 meV, see figure (4.8).Among the studied cases the zigzag behaviour shown in interband gain, IVBA and as a result in net gain figures is a numerical behaviour not a real physical reason, such can be improved by increasing the resolution in the numerical procedure in k-space.

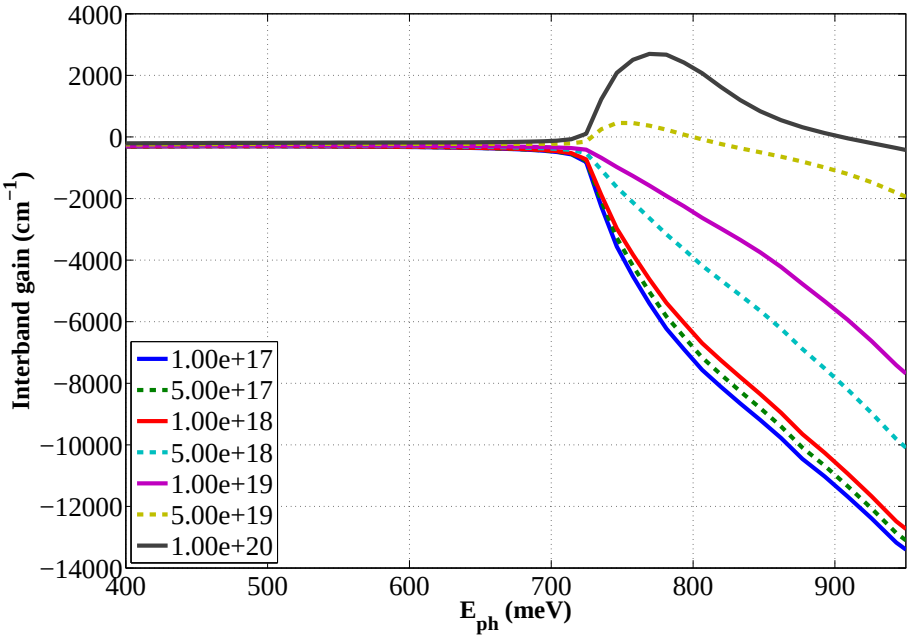

Figure 4.5: Room temperature Interband gain spectra of 0.5 % tensile strained [001] bulk Ge for a range of injected carrier densities from $n_{inj} = p_{inj} = 10^{17}$ to 10^{20} cm^{-3}.

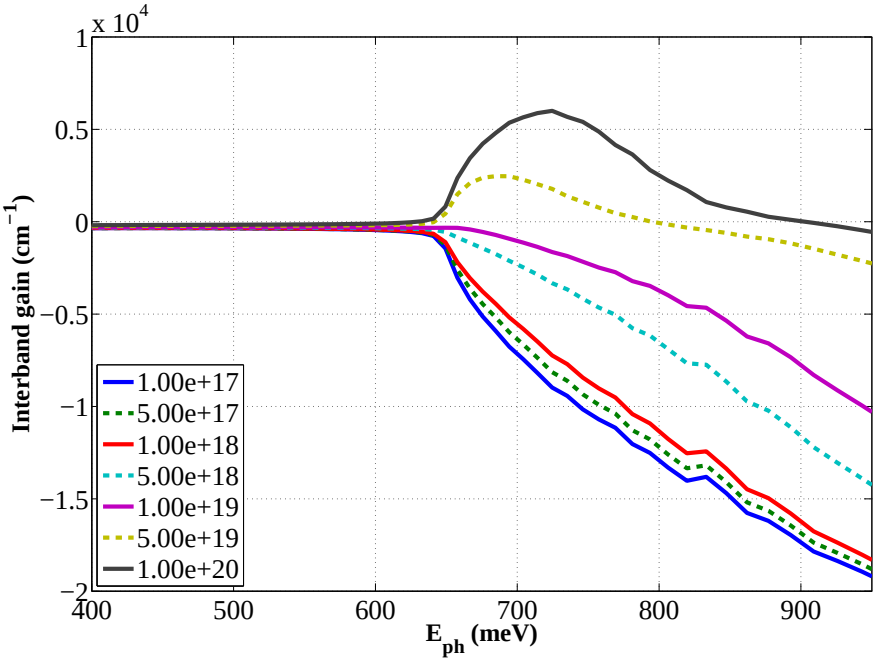

Figure 4.6: Room temperature Interband gain spectra of 1.0 % tensile strained [001] bulk Ge for a range of injected carrier densities from $n_{inj} = p_{inj} = 10^{17}$ to 10^{20} cm^{-3}.

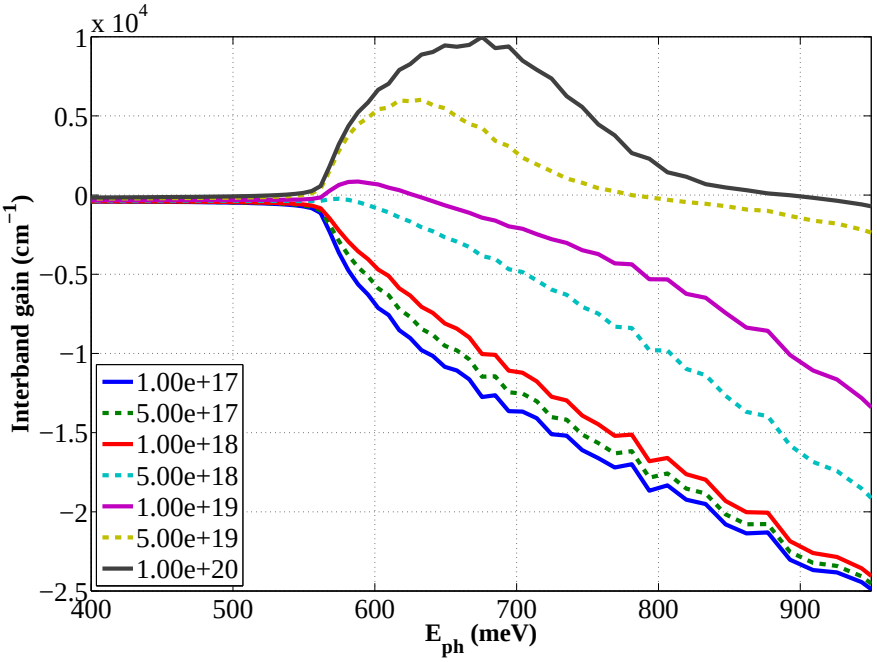

Figure 4.7: Room temperature Interband gain spectra of 1.5 % tensile strained [001] bulk Ge for a range of injected carrier densities from $n_{inj} = p_{inj} = 10^{17}$ to $10^{20}\,\mathrm{cm}^{-3}$. The zigzag line behaviour is a result of limitations of numerical modelling used.

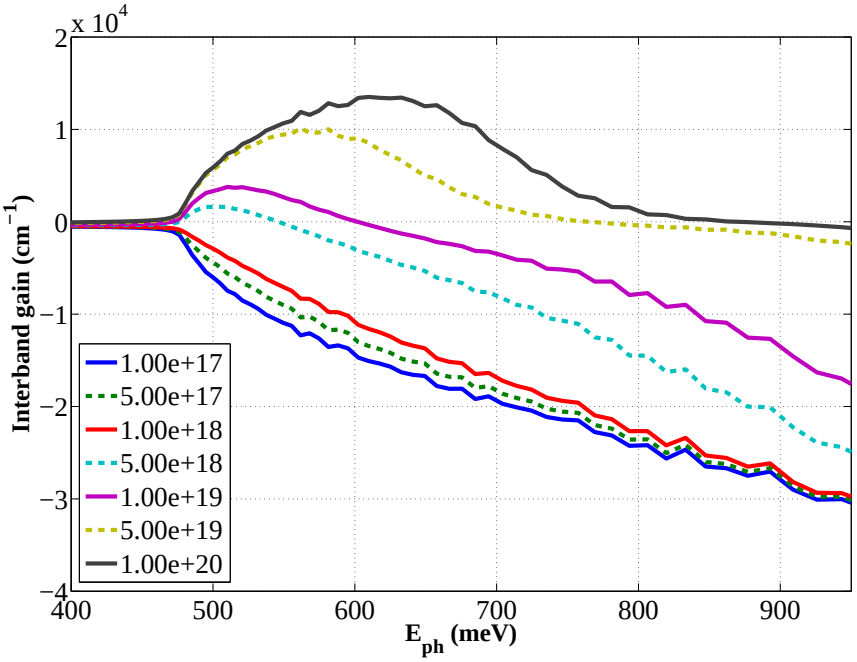

Figure 4.8: Room temperature Interband gain spectra of 2.0 % tensile strained [001] bulk Ge for a range of injected carrier densities from $n_{inj} = p_{inj} = 10^{17}$ to $10^{20}\,\mathrm{cm}^{-3}$.

4.6.2 *Interband gain dependence on carrier density*

Achieving a very high carrier electron density is essential for producing interband gain in [001] bulk Ge, however applying tensile strain will reduce this required carrier density. Figures (4.9 - 4.12) illustrate the effect of increasing the biaxial tensile strain on the interband gain of strained bulk Ge, with an injection carrier density of $n_{inj} = p_{inj} = 5 \times 10^{18}$, 10^{19}, 5×10^{19} and $10^{20}\,\mathrm{cm}^{-3}$, respectively at room temperature. The shift of the interband gain peak is caused by the reduction in the direct band gap due to applied tensile strain.

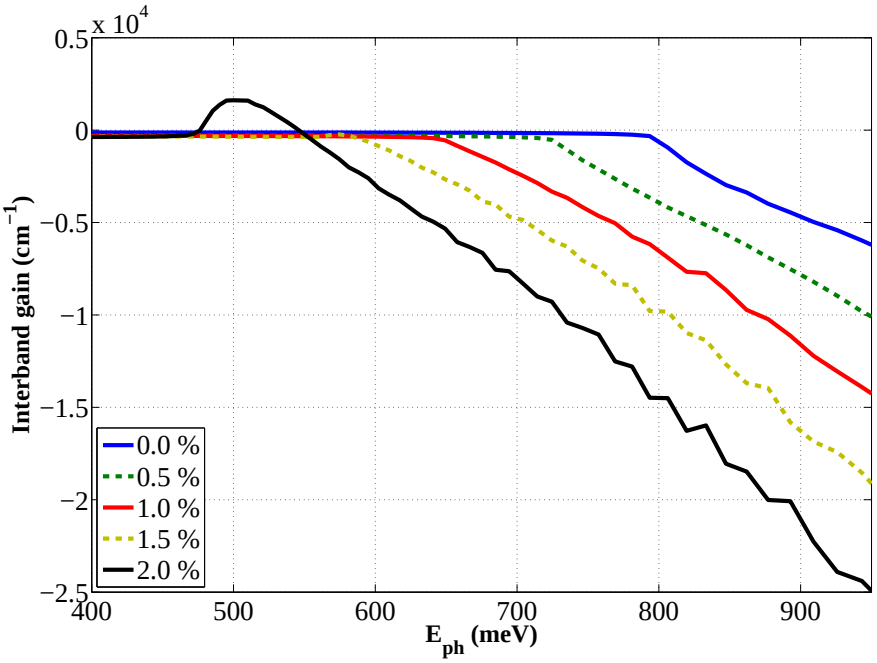

Figure 4.9: The interband gain of bulk [001] Ge for various biaxial tensile strain values, $\varepsilon_{||} = 0.0$, 0.5, 1.0, 1.5, and 2.0 %, at room temperature, an injected carrier density of $n = p = 5 \times 10^{18}\,\mathrm{cm}^{-3}$.

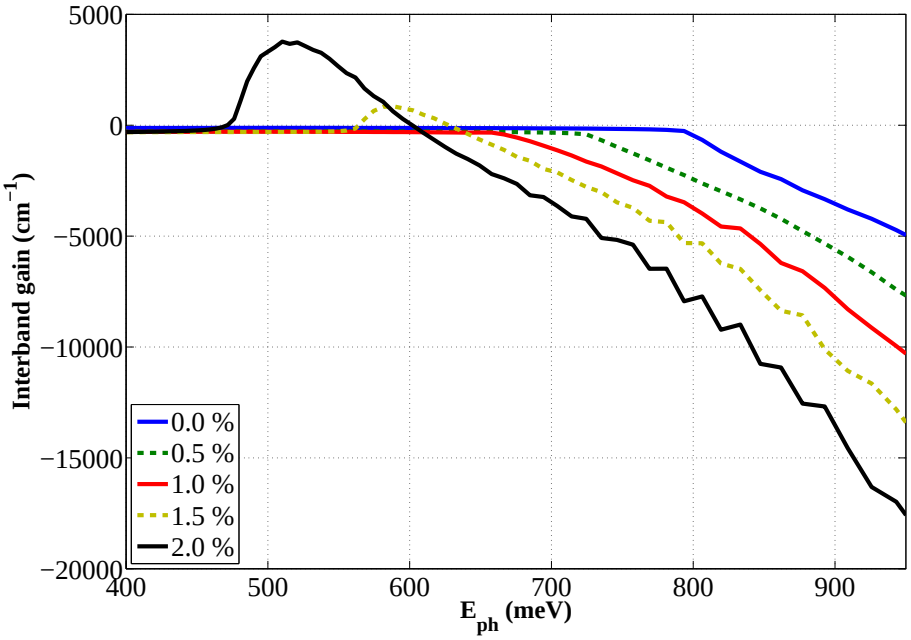

Figure 4.10: The interband gain of bulk [001] Ge for various biaxial tensile strain values, $\varepsilon_{||} = 0.0$, 0.5, 1.0, 1.5, and 2.0 %, at room temperature, an injected carrier density of $n = p = 10^{19}\,\mathrm{cm}^{-3}$.

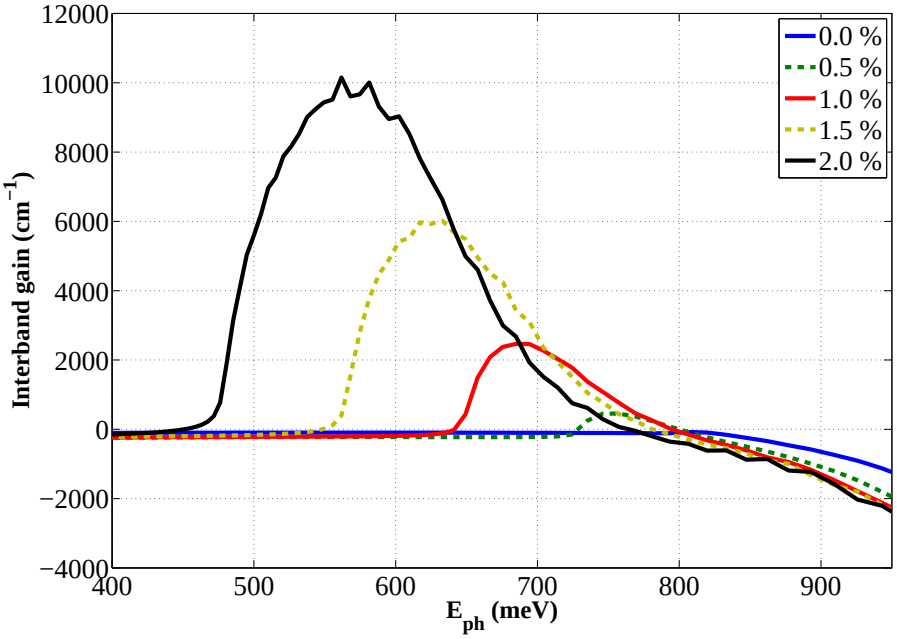

Figure 4.11: The interband gain of bulk [001] Ge for various biaxial tensile strain values, $\varepsilon_{||} = 0.0$, 0.5, 1.0, 1.5, and 2.0 %, at room temperature, an injected carrier density of $n = p = 5 \times 10^{19}\,\mathrm{cm}^{-3}$.

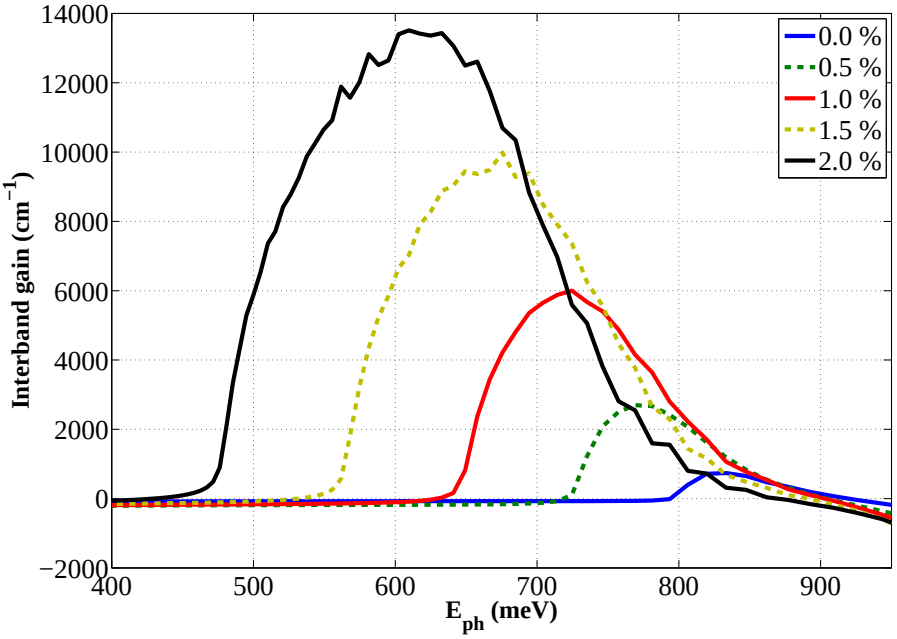

Figure 4.12: The interband gain of bulk [001] Ge for various biaxial tensile strain values, $\varepsilon_{||} = 0.0$, 0.5, 1.0, 1.5, and 2.0 %, at room temperature, an injected carrier density of $n = p = 10^{20}\,\mathrm{cm}^{-3}$.

4.7 INTERVALENCE BAND ABSORPTION RESULTS

The effect of varying carrier injection under different tensile strain conditions, at room temperature has been investigated for [001] bulk Ge. The intervalence band absorption has been calculated, and it was found that an increase in injected holes increases the IVB absorption dramatically, mainly due to absorption between the HH and other valence bands (LH and SO) for a given photon energy. Figure (4.13) illustrates this for hole densities of 10^{17} to $10^{20}\,\mathrm{cm}^{-3}$.

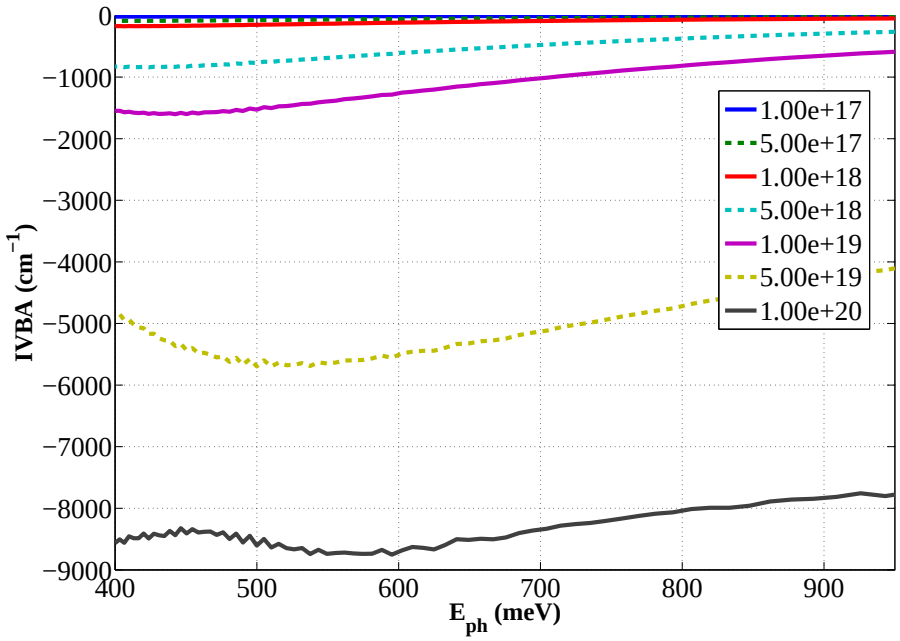

Figure 4.13: The intervalence band absorption spectra of [001] bulk Ge for a range of hole carrier densities from 10^{17} to $10^{20}\,\mathrm{cm}^{-3}$, at 300 K.

4.7.1 *Intervalence band absorption variation with applied strain*

The degeneracy between HH and LH is lifted when bulk Ge is under biaxial tensile (or compressive) strain conditions. The top of the LH band increases with the applied biaxial tensile strain and the HH band maximum decreases, with the opposite effect in the case of biaxial compressive strain. Following the interband gain calculations, the chosen biaxial tensile strain values here are 0.5, 1.0, 1.5 and 2.0 % applied for [001] bulk Ge.

The calculated intervalence band absorption spectra for 0.5 % biaxial tensile strained bulk-like Ge with a range of hole densities (10^{17} to $10^{20}\,\mathrm{cm}^{-3}$) is shown in Figure (4.14). Following the same trend as in unstrained bulk Ge, the IVB absorption increases faster as the carrier density increases.

Applying a larger biaxial tensile strain will increase the IVB absorption as the separation between the LH and HH bands and the SO increases, see

figures (4.15,4.16 and 4.17). Notice here from the interband gain and IVB absorption calculations, that the intervalence band absorption will dominate the interband gain given the same strain and carrier density conditions.

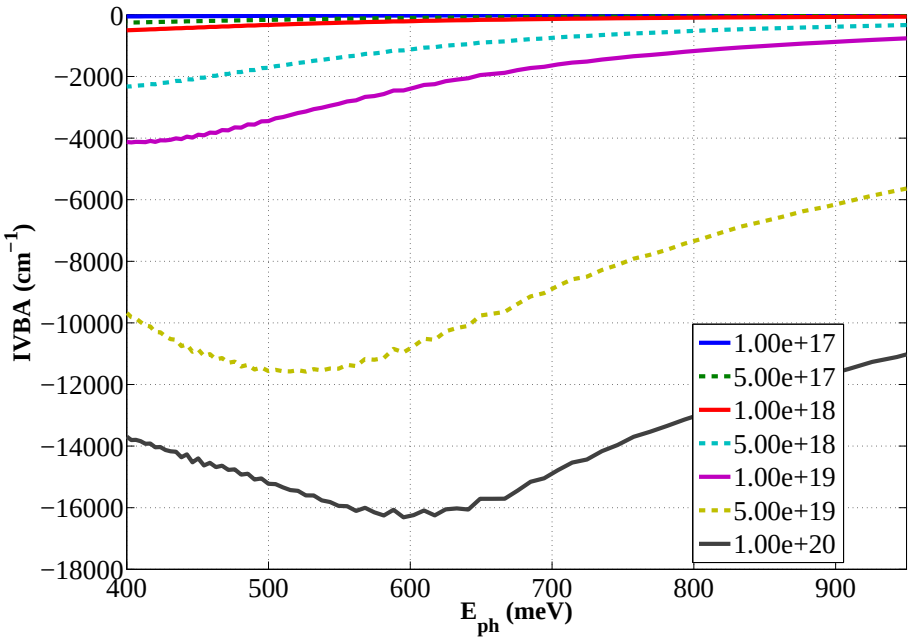

Figure 4.14: The intervalence band absorption spectra for 0.5 % biaxially tensile strained [001] bulk Ge for a range of hole carrier densities from 10^{17} to 10^{20} cm^{-3}, at 300 K.

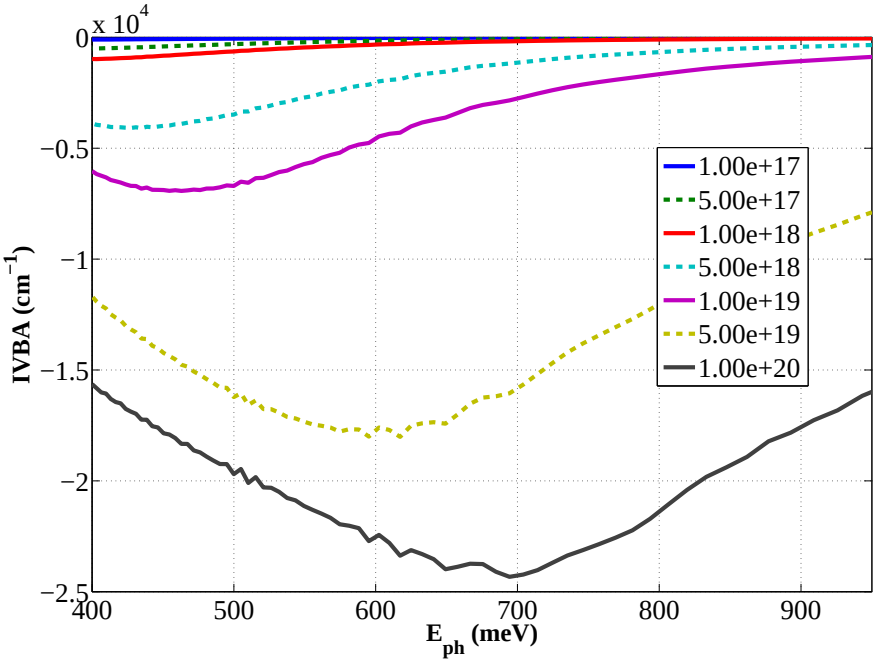

Figure 4.15: The intervalence band absorption spectra for 1.0 % biaxially tensile strained [001] bulk Ge for a range of hole carrier densities from 10^{17} to $10^{20}\,\mathrm{cm}^{-3}$, at 300 K.

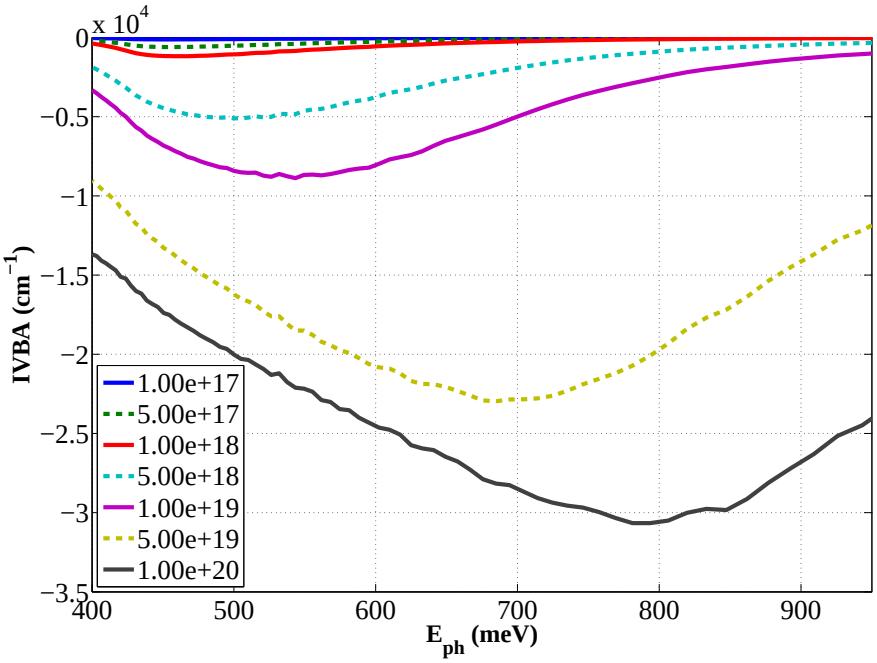

Figure 4.16: The intervalence band absorption spectra for 1.5 % biaxially tensile strained [001] bulk Ge for a range of hole carrier densities from 10^{17} to $10^{20}\,\mathrm{cm}^{-3}$, at 300 K.

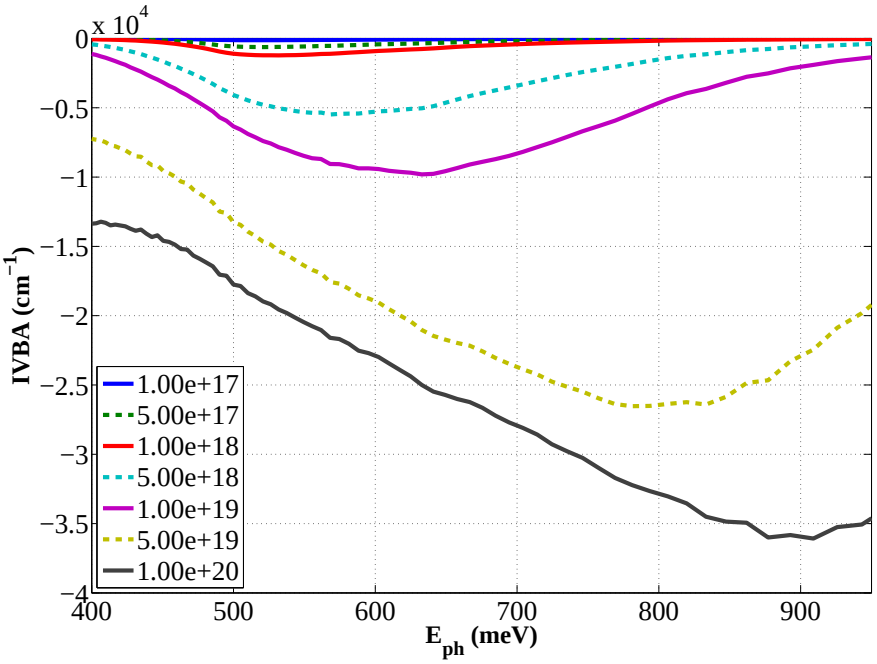

Figure 4.17: The intervalence band absorption spectra for 2.0 % biaxially tensile strained [001] bulk Ge for a range of hole carrier densities from 10^{17} to $10^{20}\,\mathrm{cm}^{-3}$, at 300 K.

4.7.2 *Dependence of carrier density quasi-Fermi level on strain*

The quasi-Fermi level as a function of carrier concentration under various biaxial tensile strain values has been extracted, along with the interband gain and IVB absorption calculations. At 300 K, [001] bulk Ge needs about $10^{20}\,\mathrm{cm}^{-3}$ of electron concentration to set the conduction band quasi-Fermi level to the bottom of Γ-valley, and a hole density of $6 \times 10^{18}\,\mathrm{cm}^{-3}$ to set the valence band quasi-Fermi level to the top of the valence band, fig. (4.18). The conduction band quasi-Fermi level decreases (for a fixed electron density) as the applied biaxial tensile strain increases. Such behavior arises since the shrinkage of the direct band gap is faster than that of the indirect band gap, which with its four equivalent valleys has much larger effective mass than the Γ-valley. This explains why, even with the energy separation between Γ and L valleys reduced, and even when Ge becomes direct band gap material, most of the electrons will populate L-valleys.

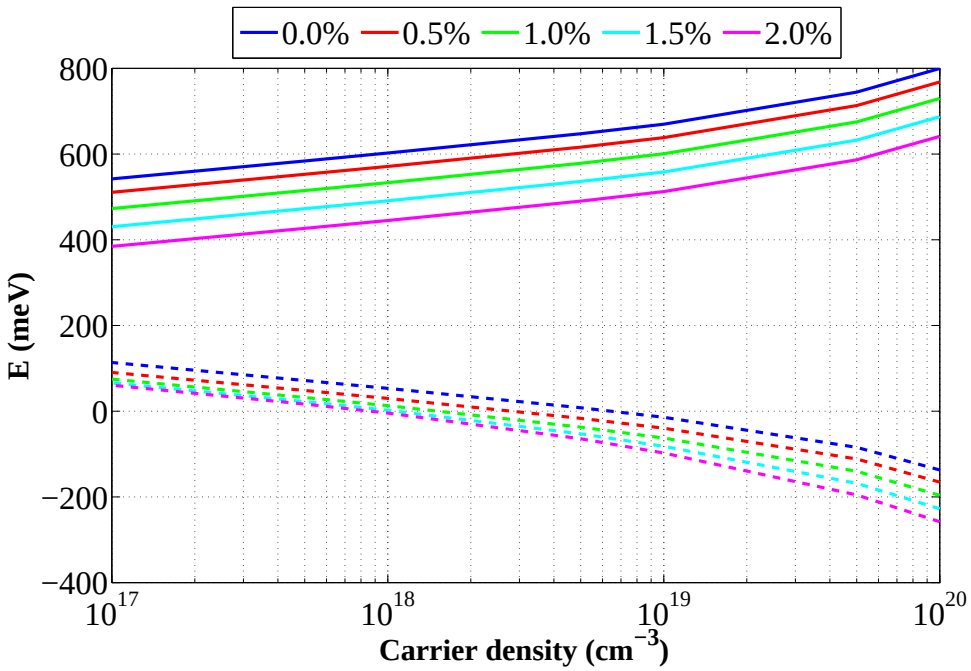

Figure 4.18: The quasi-Fermi levels of the conduction band (solid lines) and valence band (dashed lines) as a function of carrier concentration of unstrained [001] bulk Ge and under different biaxial tensile strain values, $\varepsilon_{||} = 0.5, 1, 1.5, 2\,\%$.

The valence band quasi-Fermi level as a function of hole concentration decreases with the tensile strain because the energy separation between the LH and HH bands increases, and the HH band sinks, with the applied tensile strain.

4.8 THE GAIN

Since there is a tradeoff between increasing the injected carrier concentration and applying biaxial tensile strain for [001] bulk Ge in order to obtain interband gain, and the fact that with such high injected carriers the intervalence band absorption is very large, one must control the n-type doping and the injected carrier densities in both conduction and valence bands in order to find the optimum case for gain. The gain here is the sum of the interband gain and IVB absorption. Control is achieved by introducing n-type doping to strained bulk Ge to compensate the partial of the energy difference between Γ-L, and then injecting carriers to achieve the required electron concentration in the conduction band, while keeping the hole concentration in the valence band low. The electron density (n) is the sum of the n-type doping density and injected carrier density, see fig. (4.19). Previous results of the interband gain and IVBA shows that in case of bulk Ge with only injected carriers form an external source will leave the Ge either with no interband gain due to the small number of electron density, or with domination of the IVBA over the interband gain. Therefore, the effect of the electron and hole concentrations control for doped strained bulk Ge under 1 % and 2 % biaxial tensile strain at room temperature will be discussed next.

4.8.1 *Dependence of gain on electron density*

The interband gain and IVB absorption calculations were performed for 1 and 2 % biaxial tensile strained n-type doped bulk Ge to investigate the variation of the interband gain and IVB with changing n-type doping density, while keeping injected carrier density value fixed. The total electron

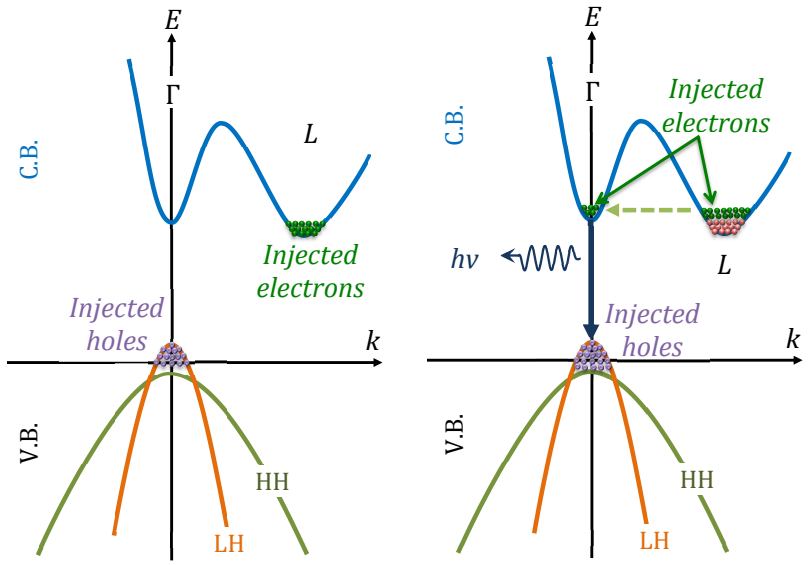

(a) Injected carriers

(b) n-type doping and Injected carriers

Figure 4.19: Scheme of Ge band structure, with injected carriers only (left) and the case of combine n-type doping and carriers injected form external source (right) [8, 12].

density has the values of $n = 10^{18}$, 5×10^{18}, 10^{19} and $5 \times 10^{19}\,\mathrm{cm}^{-3}$, while the injected carrier densities are $n_{inj} = p_{inj} = 10^{18}\,\mathrm{cm}^{-3}$.

Figure (4.20) illustrates the interband gain spectra for 1 % biaxial tensile strained bulk Ge in this range of carrier densities. There is no interband gain but the different interband behavior with varying electron density is shown. Such behavior becomes clearer as the tensile strain increases to 2 %, and the n-type doped strained bulk Ge shows interband gain at electron densities larger than $10^{19}\,\mathrm{cm}^{-3}$ as the injected carrier density is $10^{18}\,\mathrm{cm}^{-3}$, Figure (4.22).

The IVB absorption will remain the same for a given strain condition, since the valence band quasi-Fermi level does not change for a given hole concentration. Figures (4.21 and 4.23), show the IVB absorption spectra for 1 and 2 % biaxial tensile strain applied to bulk Ge with $10^{18}\,\mathrm{cm}^{-3}$ injected carrier density, at 300 K. These results suggest that the net gain is unlikely

to occur in tensile strained bulk Ge in such cases, due to suppression of interband gain and the IVB absorption.

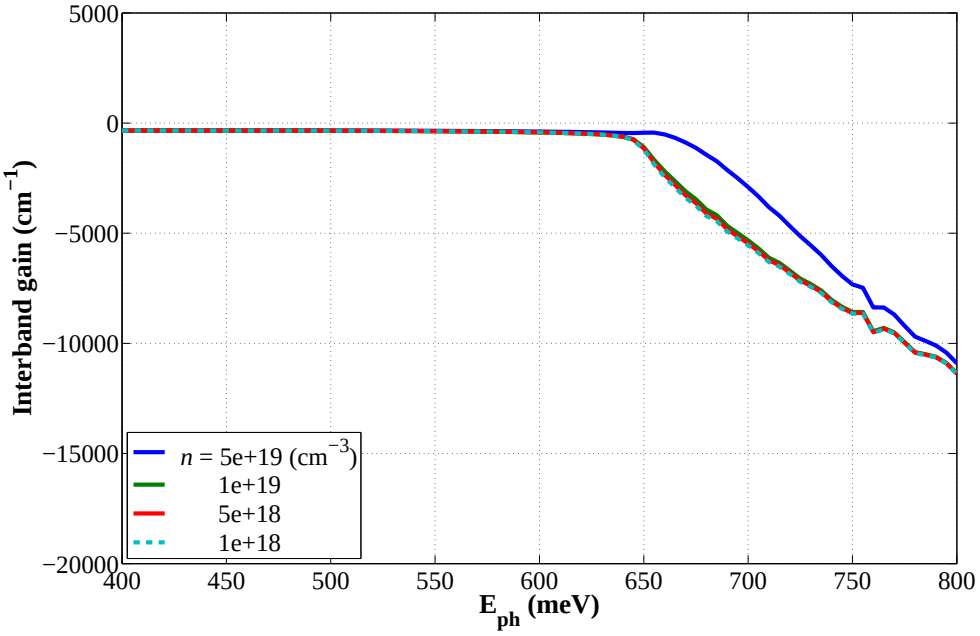

Figure 4.20: The interband gain spectra for 1 % tensile strained [001] bulk Ge with $10^{18}\,\mathrm{cm}^{-3}$ injected carriers, and a total of electron density of $n = 10^{18}$, 5×10^{18}, 10^{19} and $5 \times 10^{19}\,\mathrm{cm}^{-3}$, at room temperature.

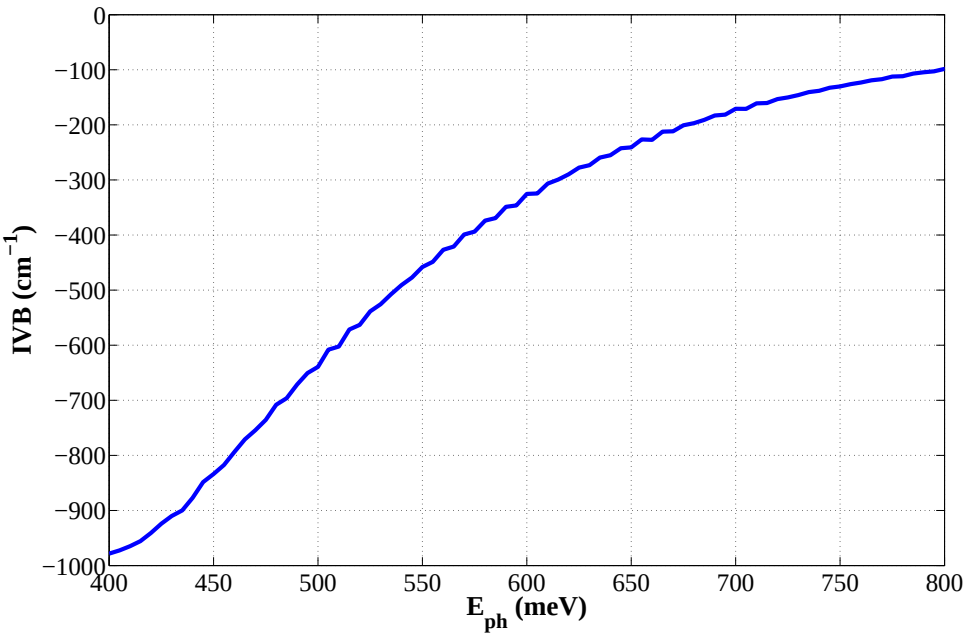

Figure 4.21: Room temperature IVB absorption spectrum for 1 % tensile strained [001] bulk Ge with $10^{18}\,\mathrm{cm}^{-3}$ injected carriers.

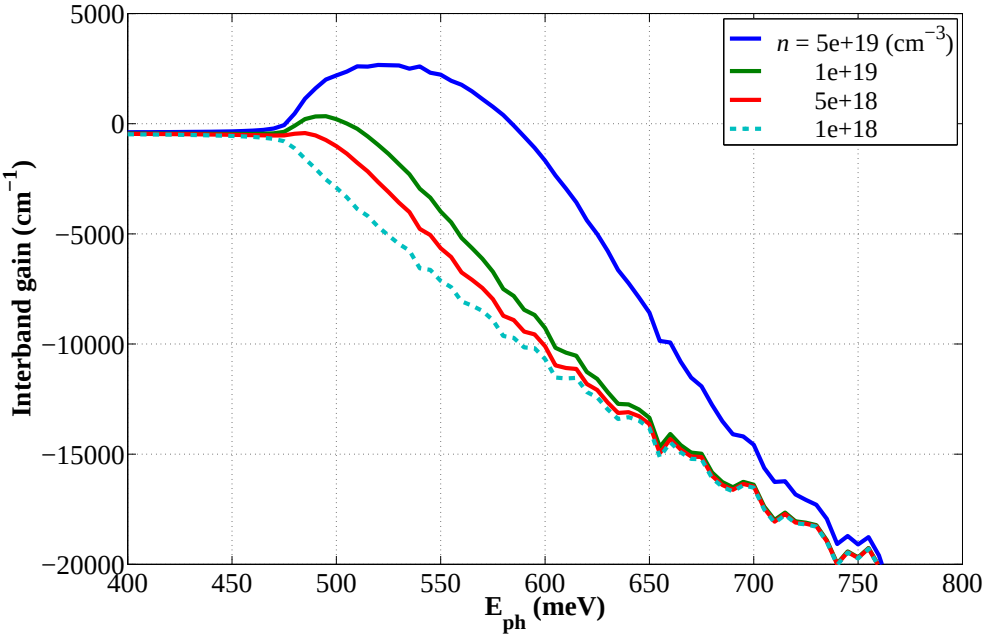

Figure 4.22: The interband gain spectra for 2 % tensile strained [001] bulk Ge with $10^{18}\,\mathrm{cm}^{-3}$ injected carriers, and total electron density of $n = 10^{18}$, 5×10^{18}, 10^{19} and $5 \times 10^{19}\,\mathrm{cm}^{-3}$, at room temperature.

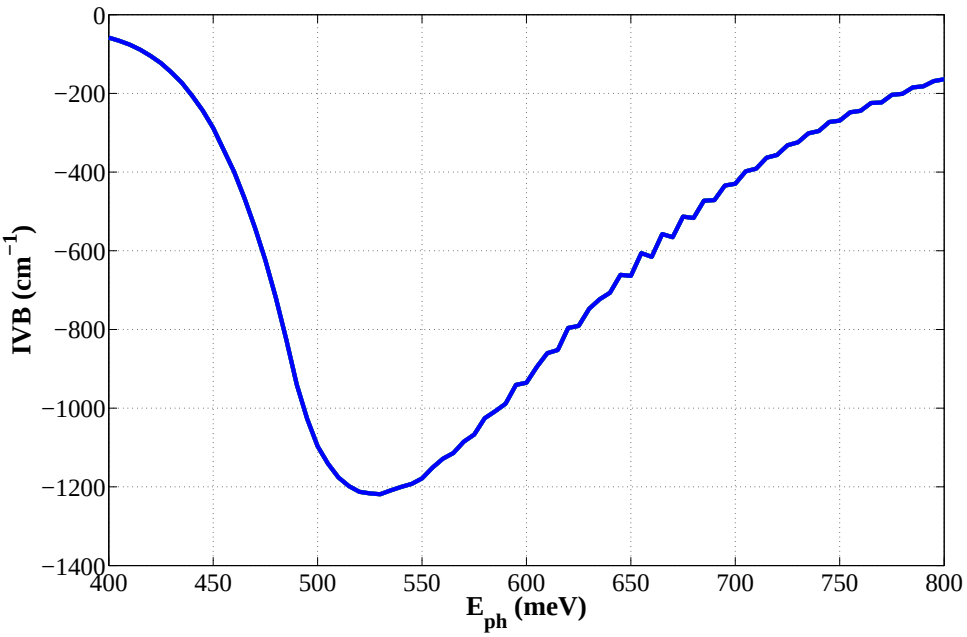

Figure 4.23: Room temperature IVB absorption spectrum for 2 % tensile strained [001] bulk Ge with $10^{18}\,\mathrm{cm}^{-3}$ injected carriers.

4.8.2 *Dependence of gain on hole density*

In this section, the optimum n-type doping and carrier injection, under variable strain conditions, for tensile strained bulk Ge, will be discussed. The total electron density is fixed at $5 \times 10^{19}\,\mathrm{cm}^{-3}$, while the injected carrier densities have values of $n_{inj} = p_{inj} = 10^{18}, 5 \times 10^{18}, 10^{19}$ and $5 \times 10^{19}\,\mathrm{cm}^{-3}$.

As the injected hole concentration varies the valence band quasi-Fermi level will take different values. This results in different IVB absorption and interband gain, despite the fixed electron density, since the valence band quasi-Fermi level is a factor in the interband gain equation.

The variation of IVB absorption with different injected carrier concentrations for 1 and 2 % biaxially tensile strained bulk Ge is shown in Figures (4.24) and (4.25), respectively. Both results show that the IVB absorption increases as the hole concentration increases, with some shift with larger strain.

The interband gain peak increases as the hole concentration increases, while the electron concentration remains fixed, Figures (4.26). As the tensile strain increases the interband peak becomes larger with an energy shift due to the direct band gap shrinkage with strain, see Figure (4.27).

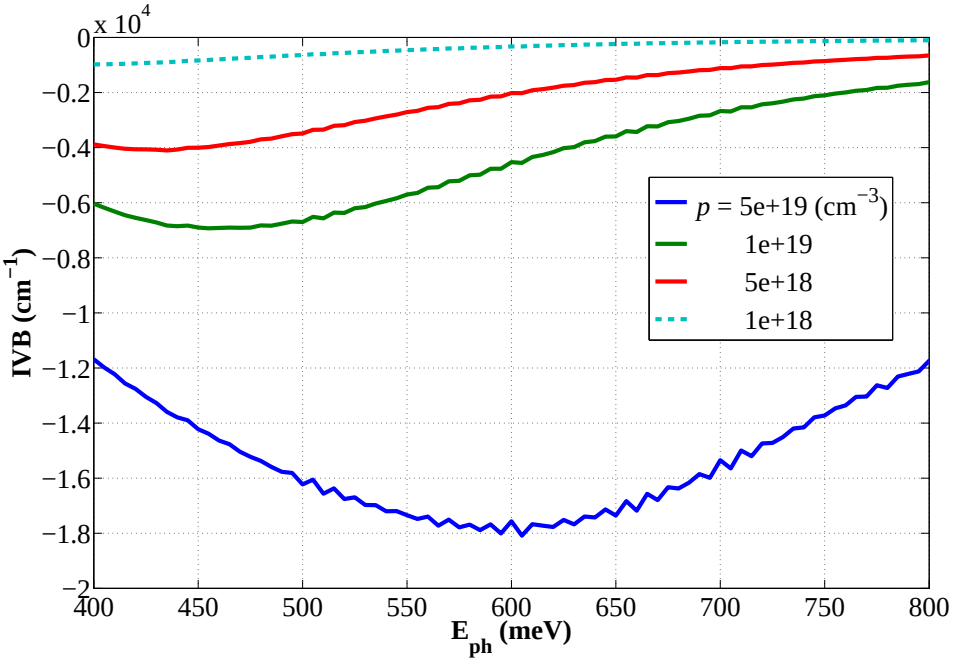

Figure 4.24: Room temperature IVB absorption spectra of 1 % tensile strained [001] bulk Ge with range of injected carriers, $n_{inj} = p_{inj} = 10^{18}$, 5×10^{18}, 10^{19} and $5 \times 10^{19}\,\mathrm{cm}^{-3}$, with $5 \times 10^{19}\mathrm{cm}^{-3}$ electron density.

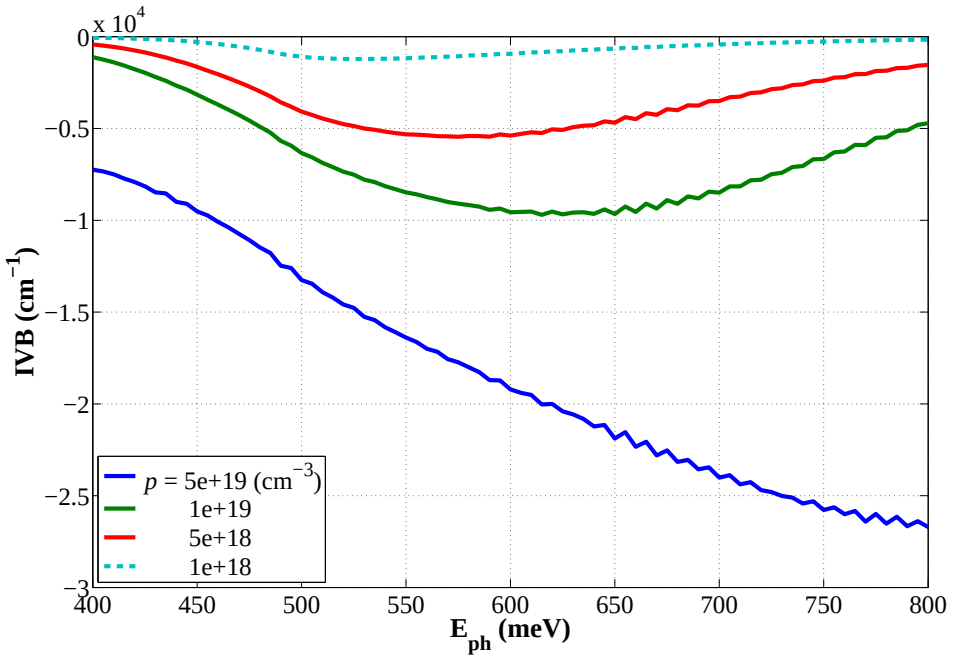

Figure 4.25: Room temperature IVB absorption spectra of 2 % tensile strained [001] bulk Ge with range of injected carriers, $n_{inj} = p_{inj} = 10^{18}$, 5×10^{18}, 10^{19} and $5 \times 10^{19}\,\mathrm{cm}^{-3}$, with $5 \times 10^{19}\mathrm{cm}^{-3}$ electron density.

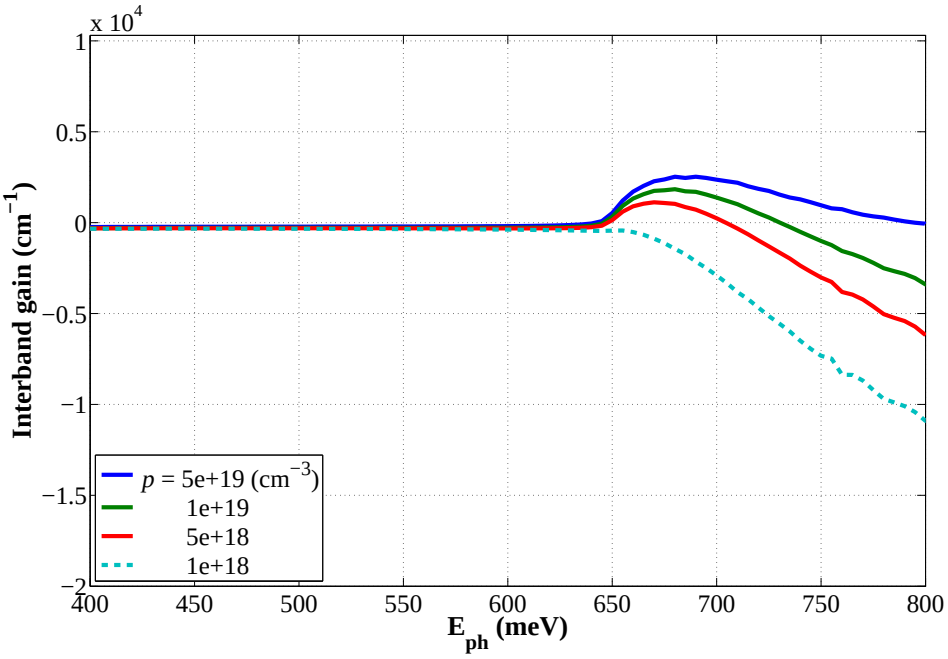

Figure 4.26: The interband gain spectra of 1 % tensile strained [001] bulk Ge with $5 \times 10^{19}\,\mathrm{cm}^{-3}$ electron density, and range of injected carriers $n_{inj} = p_{inj} = 10^{18}$, 5×10^{18}, 10^{19} and $5 \times 10^{19}\,\mathrm{cm}^{-3}$, at room temperature.

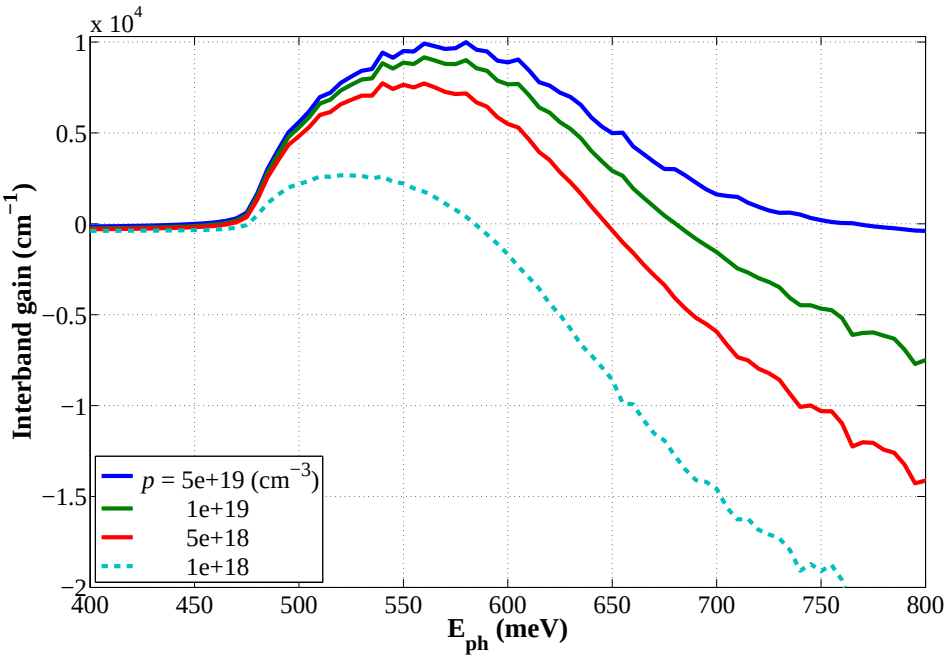

Figure 4.27: The interband gain spectra of 2 % tensile strained [001] bulk Ge with $5 \times 10^{19}\,\mathrm{cm}^{-3}$ electron density, and range of injected carriers $n_{inj} = p_{inj} = 10^{18}$, 5×10^{18}, 10^{19} and $5 \times 10^{19}\,\mathrm{cm}^{-3}$, at room temperature.

4.8.3 *Gain as a function of the applied tensile strain*

As the IVBA dominate the interband gain for the tensile strained [001] bulk Ge cases of increasing the injected carriers densities in order to obtain interband gain, see 4.6 and 4.7. Also, previously in this section result shows the tradeoff between the IVBA and interband gain for dependently controlled electron and hole densities for only two values of tensile strain. Here, a closer look to the interband gain and tradeoff of the sum of the interband gain and IVBA as a function of the applied tensile strain at 300 K for the same cases of fixing the total electron density while the hole density vary and vice versa.

Figures 4.28 and 4.29 summarize the interband gain peak results as a function of the tensile strain for [001] Ge, for the above mentioned cases of different electron and hole concentrations. The tensile strain takes five values as 0.0, 0.5, 1.0, 1.5 and 2%. It shows that for fixed electron density, a large injected carrier density will provide a large interband gain peak. Small injected carrier densities require large tensile strain for interband gain peak to occur.

Considering gain, figure (4.30 and 4.31) illustrate the sum of the interband gain peak and the corresponding IVB absorption as a function of applied tensile strain for [001] bulk Ge, under different electron and hole densities. The results show a tradeoff between the interband gain and the IVB absorption for larger carrier concentrations. This also shows the importance of applied tensile strain in creating gain for bulk-like Ge.

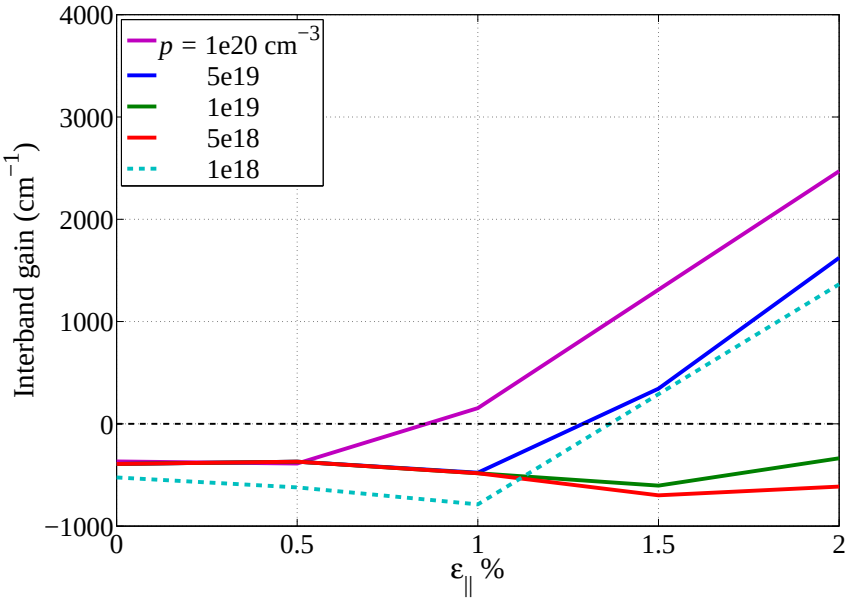

Figure 4.28: The interband gain peak as a function of applied tensile strain for [001] bulk Ge with $5 \times 10^{19}\,\mathrm{cm}^{-3}$ total electron density, and range of injected carriers $n_{inj} = p_{inj} = 10^{18}$, 5×10^{18}, 10^{19}, 5×10^{19} and $10^{20}\,\mathrm{cm}^{-3}$, at room temperature.

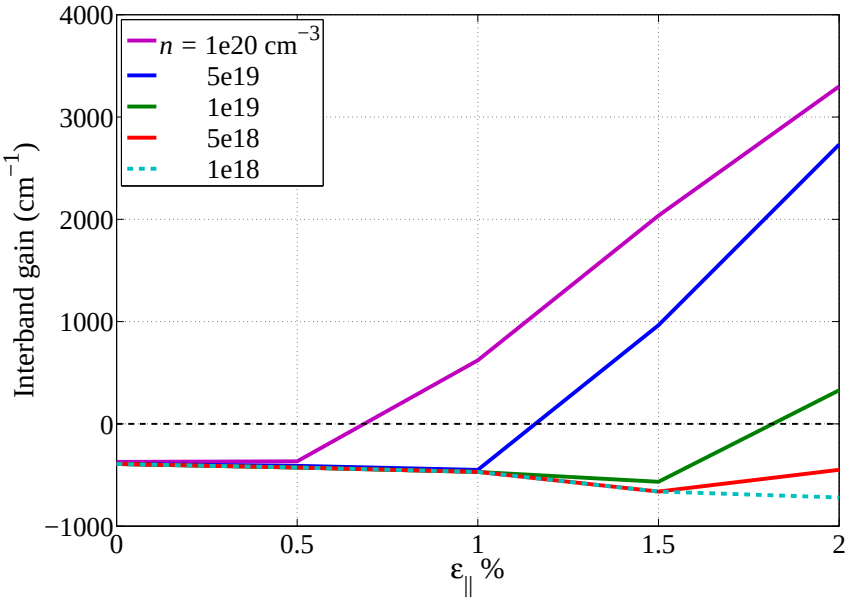

Figure 4.29: The interband gain peak as a function of applied tensile strain for [001] bulk Ge with injected carriers as $n_{inj} = p_{inj} = 10^{18}\,\mathrm{cm}^{-3}$, and total electron density has range of $n = 10^{18}$, 5×10^{18}, 10^{19}, $5 \times 10^{19}$and $10^{20}\,\mathrm{cm}^{-3}$, at room temperature.

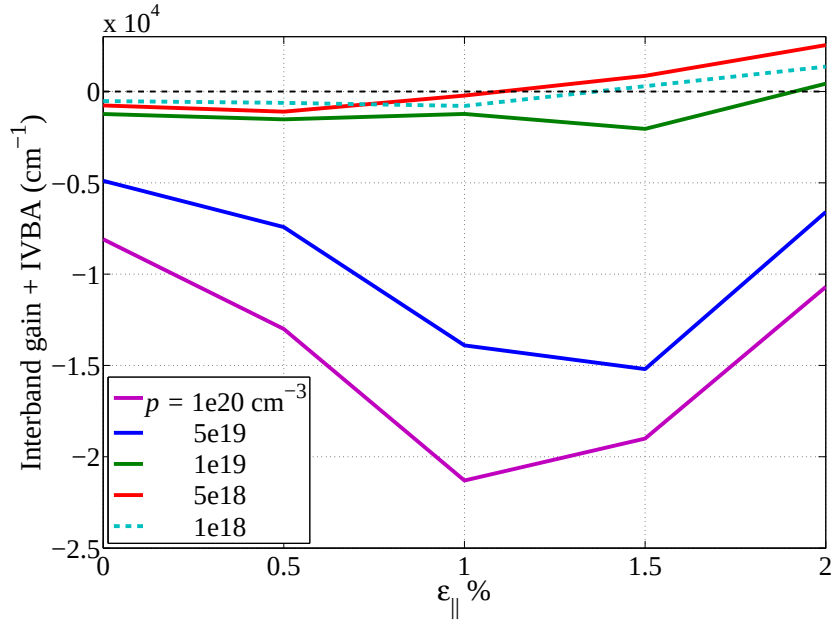

Figure 4.30: The peak gain as a function of applied tensile strain for [001] bulk Ge with $5 \times 10^{19}\,\mathrm{cm}^{-3}$ total electron density, and range of injected carriers $n_{inj} = p_{inj} = 10^{18}$, 5×10^{18}, 10^{19}, 5×10^{19} and $10^{20}\,\mathrm{cm}^{-3}$, at room temperature.

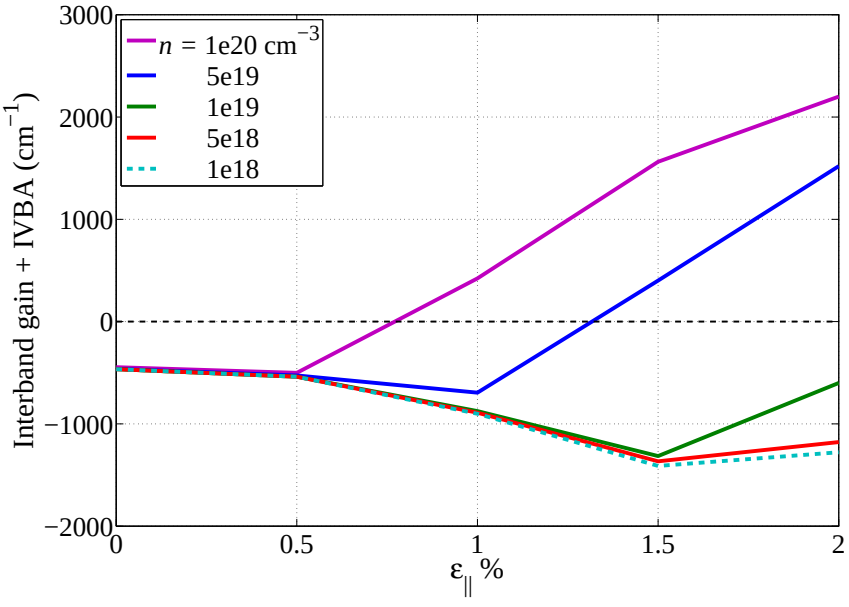

Figure 4.31: The peak gain as a function of applied tensile strain for [001] bulk Ge with injected carriers as $n_{inj} = p_{inj} = 10^{18}\,\mathrm{cm}^{-3}$, and total electron density has range of $n = 10^{18}$, 5×10^{18}, 10^{19}, $5 \times 10^{19}$and $10^{20}\,\mathrm{cm}^{-3}$, at room temperature.

4.9 TEMPERATURE AND GAIN DEPENDENCE

Temperature is another important factor to be considered in gain calculations, as it is known that as temperature rises the direct and indirect band gaps shrink [93, 94]. In reality, the Ge laser will operate at about 353 K, hence the gain calculations were performed for 2 % tensile strained bulk Ge at 353 K for the same electron and hole concentrations as in the previous section.

Figure (4.32) and (4.33) shows the gain spectra of 2 % tensile strained bulk Ge, with $5 \times 10^{19}\,\mathrm{cm}^{-3}$ electrons and a range of $p = 10^{18}$, 5×10^{18}, 10^{19} and $5 \times 10^{19}\,\mathrm{cm}^{-3}$, at 300 and 353 K, respectively. The results show that the gain spectrum varies with electron and hole concentrations, but overall is only weakly dependent on the system temperature, that difference dependent vary from one case to another depending on the electron and hole densities (between 7-20%). The gain peak is red shifted due to the fact that the band gap decreases with temperature.

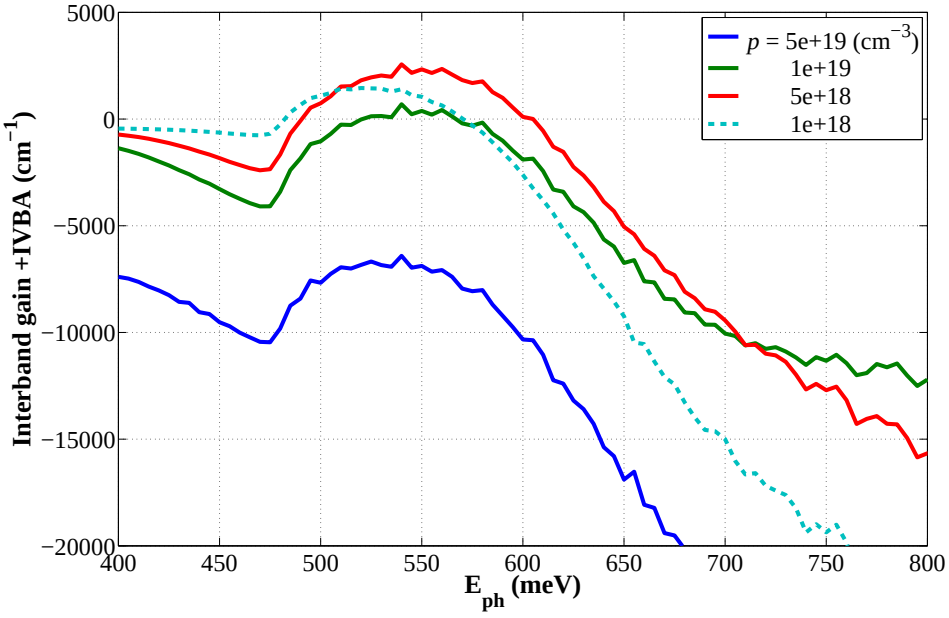

Figure 4.32: The room temperature gain spectra of 2 % tensile strained for [001] bulk Ge with $5 \times 10^{19}\,\mathrm{cm}^{-3}$ electron density, and range of injected carriers $n_{inj} = p_{inj} = 10^{18}$, 5×10^{18}, 10^{19} and $5 \times 10^{19}\,\mathrm{cm}^{-3}$.

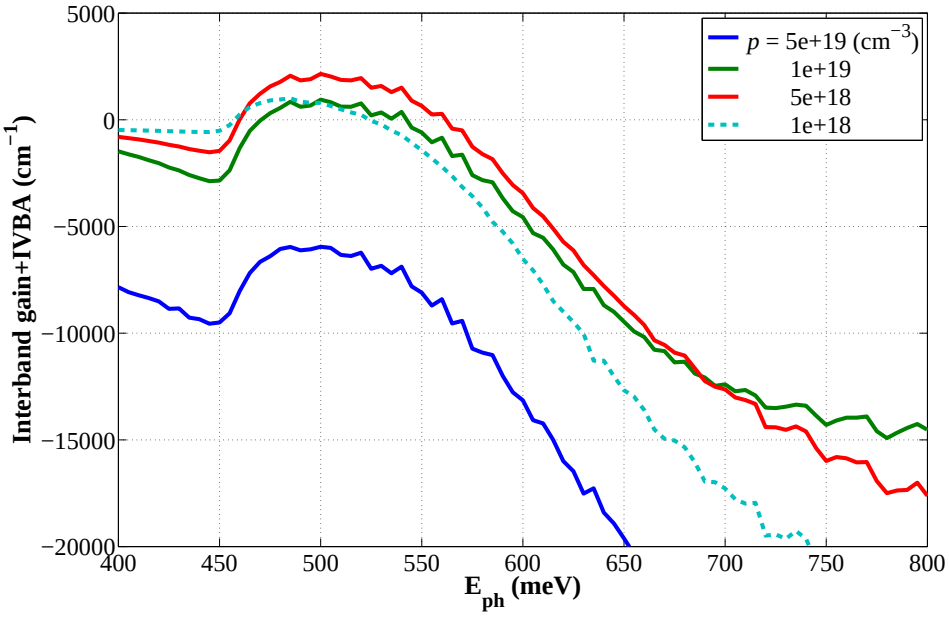

Figure 4.33: The gain spectra at 353 K of 2 % tensile strained [001] bulk Ge with $5 \times 10^{19}\,\mathrm{cm}^{-3}$ electron density, and range of injected carriers $n_{inj} = p_{inj} = 10^{18}$, 5×10^{18}, 10^{19} and $5 \times 10^{19}\,\mathrm{cm}^{-3}$.

4.10 CONCLUSION

Energy bands were calculated using the 8×8 **k**.**p** method for direct valley, and the effective mass approximation for indirect valleys, for bulk Ge under tensile strain. At finite temperatures, the carrier population of states was described by the quasi-Fermi levels. Then the interband gain spectra, and IVB absorption were both calculated. These calculations were performed to investigate the effect of strain conditions, electron and hole densities, and temperature on the interband gain and IVBA, and hence on the gain achievable in n^+ bulk Ge. These results suggest that population inversion is achievable in [001] bulk Ge with large tensile strain ($\varepsilon_{||} > 1\,\%$) for successful operation of mid-infrared Ge lasers. Independent control of electron and hole densities (via doping and carrier injection) is important to optimise the gain in a Ge laser. In general, high hole densities result in very strong IVB absorption. The gain spectrum is only weakly dependent on temperature in the 300-353 K temperature range. However, these observations do not account for additional free carrier absorption processes which may occur in the conduction bands. These will be investigated in the next chapter.

5

FREE CARRIER ABSORPTION

Free carrier absorption (FCA) is known to be a significant loss process in semiconductor materials and optical devices under conditions of high carrier densities. The simple Drude model of FCA predicts a parabolic dependence on photon wavelength, which is a good approximation for long wavelengths, corresponding to small photon energies which are comparable to the lifetime broadening for the electronic states. However, for the much larger photon energies involved in Ge lasers, this approximation does not hold, and a more accurate calculation is required, which accounts for the details of the Ge band structure and the electron scattering processes which give rise to FCA transitions [95]. This chapter shows the general method for calculating free carrier absorption types in doped tensile strained bulk Ge case and then investigate its effect on the total gain.

For a parabolic band structure, Tsai *et.al.* presented a general derivation of free carrier absorption coefficient for both intravalley and intervalley transitions considering a degenerate carrier distribution and the state-filling effect [13]. Following their model, in this chapter the intravalley and intervalley FCA coefficients will be calculated for bulk [001] Ge under various strain conditions and different doping concentrations. Furthermore, the temperature dependence in those cases will be considered.

5.1 FREE CARRIER ABSORPTION IN SEMICONDUCTORS

A carrier transits to a state $|f\rangle$ with higher energy (E_f) from a state $|i\rangle$ with initial energy (E_i) when it absorbs a photon ($\hbar\omega_t$). When this physical process occurs in the conduction band it is called free carrier absorption, it is referred to as the FCA [96]. If it happens within one conduction band valley, it is known as intravalley FCA, whilst intervalley FCA refers to the process which happens between two different valleys in the conduction band, fig. (5.1).

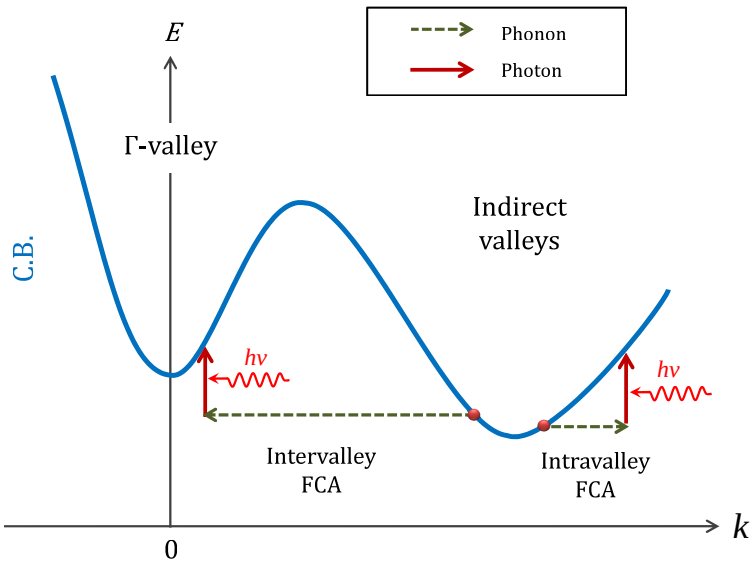

Figure 5.1: Intervalley and intravalley free carrier absorption in the bulk Ge conduction band.

FCA is a two-step process where the carrier needs adequate momentum to scatter to a higher state. Optical or acoustic phonon ($\hbar\omega_q$) will provide the shift in carrier momentum. Charged impurity scattering can also provide the necessary momentum shift. The classical Drude model conventionally describes FCA as depending on λ^2, which is the case in the long-wavelength region [97]. The free carrier absorption coefficient is

$$\alpha_{FCA} = \frac{e^2 \lambda^2 n_c}{4\pi^2 c^3 n_r \varepsilon_0 m^* \tau_c}, \tag{5.1}$$

where m^* is the carrier effective mass, τ_c is the effective scattering time, which can be determined by the carrier mobility (μ_c) as in $\tau_c = \frac{m^*}{e}\mu_c$, and n_c is the carrier density [92].

Second-order perturbation theory of quantum mechanics gives the scattering rate as

$$W_{i\to f} = \frac{2\pi}{\hbar} \sum_n \left| \frac{\langle f | H_{\text{per}} | n \rangle \langle n | H_{\text{per}} | i \rangle}{E_i - E_n} \right|^2 \delta\left(E_f - E_i\right), \tag{5.2}$$

where $|n\rangle$ is the intermediate state, and the interaction Hamiltonian (H_{per}) is the total of the four Hamiltonians for electron-photon absorption (H^a_{ct}) and emission (H^e_{ct}), and electron-phonon absorption (H^a_{cn}) and emission (H^e_{cn}) [84]. Figure 5.2 presents all the eight possible electron-phonon interactions to start from initial wavevector ($\vec{k_i}$) to final one ($\vec{k_f} = \vec{k_i} \pm q$) in intravalley free carrier scattering, which is the same case for intervalley free carrier absorption [84]. Then the scattering rate is

$$\begin{aligned} W_{k\to k\pm q} &= \frac{2\pi}{\hbar} \sum_n |S_1 + S_2 + S_3 + S_4 + S_5 + S_6 + S_7 + S_8|^2 \\ &\quad \times \delta\left(E_k - E_{k\pm q} \pm \hbar\omega_q \pm \hbar\omega_t\right). \end{aligned} \tag{5.3}$$

Based on common initial and common final states for these eight routes, the eight terms can be grouped into four terms as: $S_{++} = S_1 + S_3$, $S_{-+} = S_2 + S_4$, $S_{+-} = S_5 + S_7$, and $S_{--} = S_6 + S_8$. Then the energy conservation in the delta function implies that the square of the whole sum can be written as $\left|\sum_{i=1}^{8} S_i\right|^2 = |S_{++}|^2 + |S_{-+}|^2 + |S_{+-}|^2 + |S_{--}|^2$, where

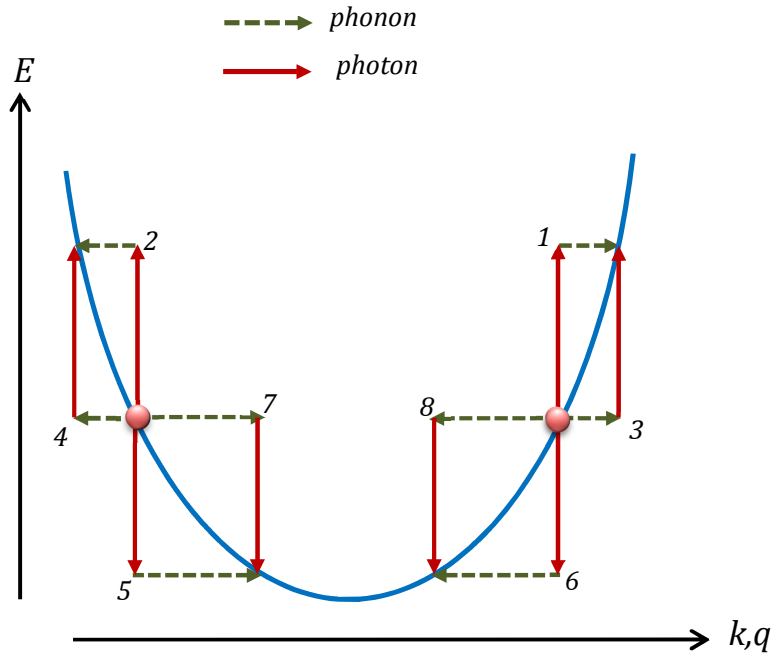

Figure 5.2: All possible electron-phonon plus photon intravalley scatterings, after [13, 14].

$$|S_{++}|^2 = |S_{+-}|^2 = |M_q|^2 N_q \frac{\hbar s e^2}{2\varepsilon\omega_t^2 m^{*2}} (\hat{e}.q)^2, \tag{5.4}$$

$$|S_{-+}|^2 = |S_{--}|^2 = |M_q|^2 (N_q + 1) \frac{\hbar s e^2}{2\varepsilon\omega_t^2 m^{*2}} (\hat{e}.q)^2, \tag{5.5}$$

where s is the photon density. The plus $(+)$ and minus $(-)$ signs refer to emission and absorption processes, respectively, for both phonon and photon in the subscripts [13]. The phonon number (N_q) is given by the Bose-Einstein distribution function

$$N_q = \left[\exp\left(\frac{\hbar\omega_q}{k_B T_L}\right) - 1\right]^{-1}, \tag{5.6}$$

where T_L is the lattice temperature, and $|M_q|^2$ is the carrier-phonon interaction [92].

The FCA coefficient can be expressed in terms of the scattering rate as

$$\alpha_{FCA} = \frac{1}{v_g s V_c} \sum_k W_{k \to k \pm q} \, f_k \left(1 - f_{k \pm q}\right), \tag{5.7}$$

where v_g is the photon group velocity and V_n is the phonon normalisation volume [13]. Using eq. (5.3) the FCA coefficient can be written as

$$\begin{aligned} \alpha_{FCA} \;=\; & \frac{1}{v_g s V_c} \sum_{k,q} \frac{2\pi}{\hbar} \\ & \Big[|S_{++}|^2 f_k (1 - f_{k+q}) \delta(E_k - E_{k+q} + \hbar\omega_q + \hbar\omega_t) \\ + \; & |S_{-+}|^2 f_k (1 - f_{k-q}) \delta(E_k - E_{k-q} - \hbar\omega_q + \hbar\omega_t) \\ - \; & |S_{+-}|^2 f_k (1 - f_{k+q}) \delta(E_k - E_{k+q} + \hbar\omega_q - \hbar\omega_t) \\ - \; & |S_{--}|^2 f_k (1 - f_{k-q}) \delta(E_k - E_{k-q} - \hbar\omega_q - \hbar\omega_t) \Big], \end{aligned} \tag{5.8}$$

$\hbar\omega_t$ is the photon energy and $\hbar\omega_q$ is the phonon energy [13]. The Fermi-Dirac distribution function (f_k) of carriers

$$f_k = \left[\exp\left(\frac{E_k - E_{Fc}}{k_B T_c} \right) + 1 \right]^{-1}, \tag{5.9}$$

where T_c is the temperature of carriers [92]. In this chapter, the lattice temperature and carrier temperature are assumed to be the same ($T_L = T_c$). Also, the thermal equilibrium condition for both carriers and phonons is assumed for the calculations of this chapter.

5.2 INTERVALLEY FCA PHONON SCATTERING

By acoustic and optical phonons, a carrier can be scattered from one valley to another one [98]. The intervalley free carrier absorption expression can be derived from eq. (5.8) as

$$
\begin{aligned}
\alpha_{interFCA}^{i\to f} &= \frac{e^2 k_B T_c}{12\pi^3 n_r c\varepsilon_0 \omega_t^3 \hbar^4} \int_{q_{min}}^{\infty} dq\, q^3\, V_n\, |M_q|^2 \\
&\times \left\{ \frac{N_q}{\exp(-\varepsilon_q - \varepsilon_t) - 1} \times \ln\left[\frac{\exp(-\eta + \varepsilon_q + \varepsilon_t) + \exp(-\varepsilon_{--}^{\min})}{\exp(-\eta + \varepsilon_q + \varepsilon_t) + \exp(-\varepsilon_{--}^{\max})} \right.\right. \\
&\qquad \left.\left. \times \frac{\exp(-\eta) + \exp(-\varepsilon_{--}^{\max})}{\exp(-\eta) + \exp(-\varepsilon_{--}^{\min})} \right] \right. \\
&+ \frac{N_q + 1}{\exp(\varepsilon_q - \varepsilon_t) - 1} \times \ln\left[\frac{\exp(-\eta - \varepsilon_q + \varepsilon_t) + \exp(-\varepsilon_{+-}^{\min})}{\exp(-\eta - \varepsilon_q + \varepsilon_t) + \exp(-\varepsilon_{+-}^{\max})} \right. \\
&\qquad \left. \times \frac{\exp(-\eta) + \exp(-\varepsilon_{+-}^{\max})}{\exp(-\eta) + \exp(-\varepsilon_{+-}^{\min})} \right] \\
&- \frac{N_q}{\exp(-\varepsilon_q + \varepsilon_t) - 1} \times \ln\left[\frac{\exp(-\eta + \varepsilon_q - \varepsilon_t) + \exp(-\varepsilon_{-+}^{\min})}{\exp(-\eta + \varepsilon_q - \varepsilon_t) + \exp(-\varepsilon_{-+}^{\max})} \right. \\
&\qquad \left. \times \frac{\exp(-\eta) + \exp(-\varepsilon_{-+}^{\max})}{\exp(-\eta) + \exp(-\varepsilon_{-+}^{\min})} \right] \\
&- \frac{N_q + 1}{\exp(\varepsilon_q + \varepsilon_t) - 1} \times \ln\left[\frac{\exp(-\eta + \varepsilon_q + \varepsilon_t) + \exp(-\varepsilon_{++}^{\min})}{\exp(-\eta + \varepsilon_q + \varepsilon_t) + \exp(-\varepsilon_{++}^{\max})} \right. \\
&\qquad \left. \left. \times \frac{\exp(-\eta) + \exp(-\varepsilon_{++}^{\max})}{\exp(-\eta) + \exp(-\varepsilon_{++}^{\min})} \right] \right\}, \qquad (5.10)
\end{aligned}
$$

where

the phonon energy is $\varepsilon_q = \frac{\hbar\omega_q}{k_B T_c}$,

the photon energy is $\varepsilon_t = \frac{\hbar\omega_t}{k_B T_c}$,

$\varepsilon_{\pm\pm}^{\max} = \frac{\left(\hbar k_{\pm\pm}^{\max}\right)^2}{2 m_c k_B T_c}$,

$$\varepsilon_{\pm\pm}^{\min} = \frac{\left(\hbar k_{\pm\pm}^{\min}\right)^2}{2m_c k_B T_c},$$

$$k_{\pm\pm}^{max} = \left|\frac{1}{2a}\left(1+\sqrt{1-4ab_{\pm\pm}}\right)\right|,$$

$$k_{\pm\pm}^{min} = \left|\frac{1}{2a}\left(1-\sqrt{1-4ab_{\pm\pm}}\right)\right|,$$

$$a = \frac{1-\left(m_f/m_i\right)}{2q},$$

$$b_{\pm\pm} = \left(\frac{q}{2} + \frac{m_f E_{\pm\pm}^{fi}}{\hbar^2 q}\right),$$

$$E_{\pm\pm}^{fi} = E_f - E_i \pm \hbar\omega_q \pm \hbar\omega_t,$$

$\eta = \frac{E_F - E_i}{k_B T_c}$ [13].

The quasi-Fermi level is E_F, which can be found for given value of electron density using numerical integration and the root finding method [99]. The total electron density is given by

$$n = \sum_{\mathrm{k}_i} 2\left(\frac{m_0 k_B T_c}{2\pi\hbar^2}\right)^{3/2} F_{\frac{1}{2}}\left(\frac{E_F - E^{\mathrm{k}_i}}{k_B T_c}\right) \tag{5.11}$$

The Fermi-Dirac integral expression can be found in refs [100, 101, 102].

The lower integral limit should fulfil the condition that

$$q_{min}^2 = \max\left(0, \left(2\hbar^{-2}E^{fi}(m_i - m_f)\right)\right). \tag{5.12}$$

For the intervalley free carrier absorption the carrier-phonon interaction is given by

$$\left|M_q\right|^2 = \frac{\hbar^2 D_{if}^2}{2\rho V_n \hbar\omega_{if}}, \tag{5.13}$$

where ρ is the Ge density, D_{if} is the corresponding deformation potential constant for (i) as the initial valley and the destination valley (f) for a phonon with energy $\hbar\omega_{if}$ [13].

5.2.1 *Direct to indirect intervalley scattering*

In bulk Ge, there is one direct Γ-valley and two indirect valleys (L and X). In zero strain case, the four pairs of L-valleys have identical distance in the reciprocal space and three equivalent X-valleys with same distance between each pair and different distance between the two valleys in the same pair. The intervalley scattering from direct to indirect valleys therefore can happen between $\Gamma \rightleftharpoons L$ and $\Gamma \rightleftharpoons X$ valleys, in both directions.

5.2.1.1 $\Gamma \rightleftharpoons L$ *intervalley scattering*

In case of unstrained or [001] strained bulk Ge, the L valley pairs remain degenerate. There are four intervalley scattering process from the Γ valley to the L valleys and vice versa. The interaction phonon has energy $\hbar\omega_{\Gamma L} = 27.56\,\text{meV}$ and a deformation potential of $D_{\Gamma L} = 2.0 \times 10^8\,\text{eV/cm}$. Those values are used in eq. (5.13) [103, 104]. Thus, by changing the corresponding index the $\Gamma \rightleftharpoons L$ intervalley scattering can be analytically integrated from eq. (5.10) as

$$\begin{aligned} \alpha_{interFCA}^{\Gamma \rightleftharpoons L} &= \sum_{i=1:4} \alpha_{interFCA}^{\Gamma \rightleftharpoons L_i} \\ &= 4 \times \left(\alpha_{interFCA}^{\Gamma \to L_1} + \alpha_{interFCA}^{L_1 \to \Gamma} \right), \end{aligned} \tag{5.14}$$

because all L valleys are identical (degenerate).

5.2.1.2 $\Gamma \rightleftharpoons X$ *intervalley scattering*

For [001] bulk Ge, there are six X valleys which gives rise to three pairs of identical intervalley scattering process from the Γ valley to the X valleys and vice versa. A deformation potential of $D_{\Gamma X} = 10^9\,\text{eV/cm}$ and a phonon

energy of $\hbar\omega_{\Gamma X} = 27.56\,\text{meV}$ are used in eq. (5.13) [103, 104]. The $\Gamma \rightleftharpoons X$ intervalley scattering can be obtained from eq. (5.10) as

$$\begin{aligned}\alpha_{interFCA}^{\Gamma\rightleftharpoons X} &= 2\times \sum_{i=1:3} \alpha_{interFCA}^{\Gamma\rightleftharpoons X_i} \\ &= 2\times \left(\alpha_{interFCA}^{\Gamma\to{}^2X} + \alpha_{interFCA}^{{}^2X\to\Gamma} + 2\alpha_{interFCA}^{\Gamma\to{}^4X} + 2\alpha_{interFCA}^{{}^4X\to\Gamma}\right) \quad (5.15)\end{aligned}$$

5.2.2 *Indirect intervalley scattering*

Calculations shows that the most of the carriers will occupy the L valleys, and because of the different energy shifts which occur in the indirect valleys when Ge is strained, studying the scattering from one indirect valley to another is needed to make the intervalley FCA calculation more realistic.

5.2.2.1 *$L\rightleftharpoons X$ intervalley scattering*

As mentioned before, the energy of the four L valleys in bulk Ge shifts down when tensile strain is applied, but not as fast as the X_2 valley (which is different from $X_{1,3}$ valleys which shift upwards with tensile strain).

The $L\rightleftharpoons X$ intervalley phonon scattering can be determined from the relation (5.13), using an interaction phonon energy $\hbar\omega_{LX} = 27.56\,\text{meV}$ and a deformation potential $D_{LX} = 4.1\times10^8\,\text{eV/cm}$ [103, 104].

The intervalley FCA coefficient is then

$$\begin{aligned}\alpha_{interFCA}^{L\rightleftharpoons X} &= 2 \times \sum_{i=1:4}\sum_{j=1:3} \alpha_{interFCA}^{L_i\rightleftharpoons X_j} \\ &= 8 \left(\alpha_{interFCA}^{L_1\to{}^2X} + \alpha_{interFCA}^{{}^2X\to L_1} + 2\alpha_{interFCA}^{L_1\to{}^4X} + 2\alpha_{interFCA}^{{}^4X\to L_1}\right). \quad (5.16)\end{aligned}$$

5.3 INTERVALLEY FCA MODELLING RESULTS

The intervalley FCA between the three conduction band valleys (Γ, L and X) were modelled for n-type doped bulk Ge at room temperature to investigate their intervalley absorption behaviour. Figure (5.3) shows the calculated intervalley FCA dependence on the absorbed photon wavelength for bulk Ge with $10^{19}\,\mathrm{cm}^{-3}$ n-type doping. The intervalley FCA coefficients show resonant behaviour when the photon energy corresponds to the separation between different conduction band minima in Ge, in contrast with the classical Drude model, which describes that the FCA coefficient depends on the square of the photon wavelength for Ge material [105].

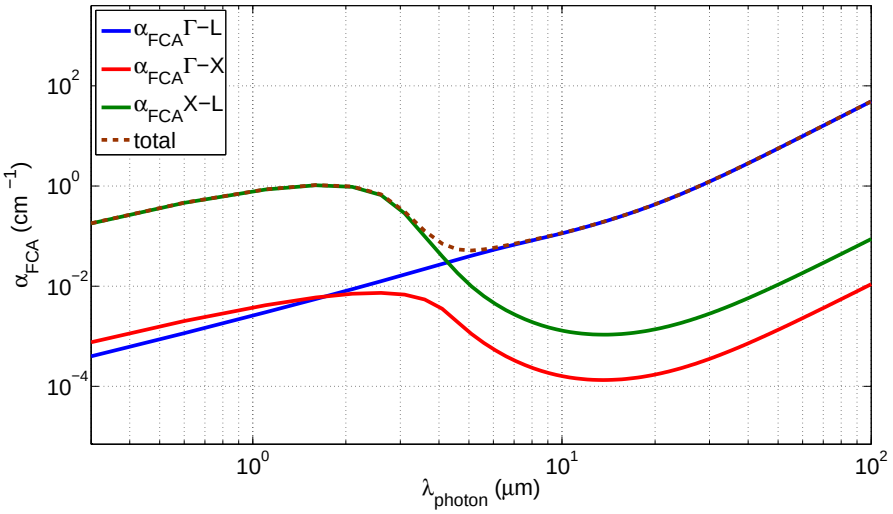

Figure 5.3: The free carrier absorption coefficient for intervalley electron scattering between three conduction band valleys (Γ, L and X) transition as a function of the photon wavelength for $10^{19}\,\mathrm{cm}^{-3}$ n-type doped bulk Ge, at 300 K.

The intervalley absorption between the X-valley and the other valleys is diminished when the photon energy becomes smaller than the energy separation between the X valley and other valleys ($E^X - E^\Gamma = 0.4\,\mathrm{eV}(3.1\mu\mathrm{m})$

and $E^X - E^L = 0.54\,\text{eV}(2.3\mu\text{m})$). A photon with such energy is not able to transfer electrons to the other valleys. The $L \rightleftharpoons X$ scattering induced absorption dominates for shorter wavelengths, whilst the $\Gamma \rightleftharpoons L$ scattering induced absorption dominates at long wavelengths.

The effect of different tensile strain and n-type doping conditions on the intervalley FCA will be discussed next for [001] bulk Ge.

5.3.1 *Strain effect*

By fixing the n-type doping density and applying different strain conditions one can investigate how the intervalley FCA behaves for bulk Ge. When tensile strain is applied to the [001] bulk Ge, one of the three X valley pairs is perpendicular to the tensile strain plane which results in partial lifting of degeneracy; i.e. splitting these two valleys ${}^2X$ from the remaining four valleys ${}^4X$. Increasing the tensile strain shifts the energy of the ${}^2X$ valleys down but not as fast as the Γ valley, and the ${}^4X$ valleys shift up, which indicates that the intervalley FCA will change with applied strain.

Figure (5.4) shows the intervalley scattering based absorption spectra between the three conduction band valleys of bulk Ge doped with $10^{19}\,\text{cm}^{-3}$ and with an applied biaxial tensile strain varying from 0.5 to 2 %. The dependance of the intervalley FCA on Figure (5.3 and 5.4) is nonmonotonic on the photon wavelength, that comes from the resonance terms in the denominator of the second perturbation expression in eq.(5.10). A portion of the electron density will populate Γ and X valleys, which is very small for zero strain compared to the L-valley electron density. As the strain increases, the Γ valley population increases, and hence the largest increase in FCA is observed for the $\Gamma \rightleftharpoons X$ processes, at short wavelengths, because of X-valley large density of states and the fact that two fold ${}^2X$ is move downward with strain.

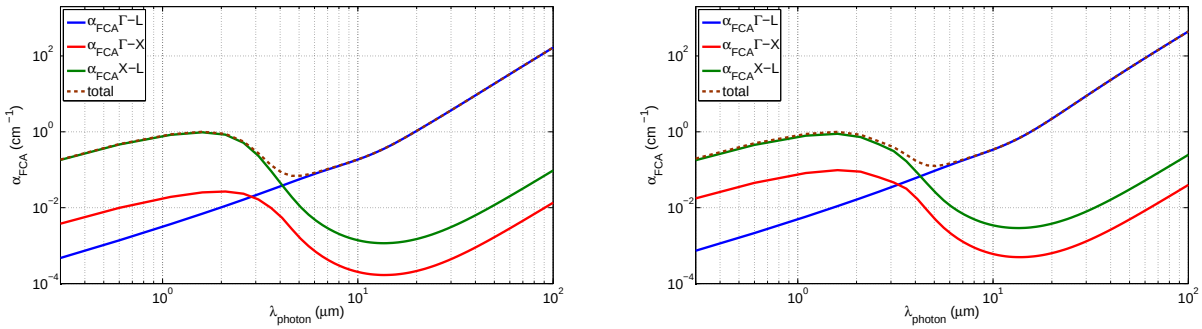

(a) $\varepsilon_{||} = 0.5\,\%$ (b) $\varepsilon_{||} = 1.0\,\%$

(c) $\varepsilon_{||} = 1.5\,\%$ (d) $\varepsilon_{||} = 2.0\,\%$

Figure 5.4: For different tensile strain conditions, the free carrier absorption coefficient for intervalley electron transitions between three conduction band valleys (Γ, L and X) as a function of the photon wavelength for $10^{19}\,\mathrm{cm}^{-3}$ n-type doped strained bulk Ge at 300 K.

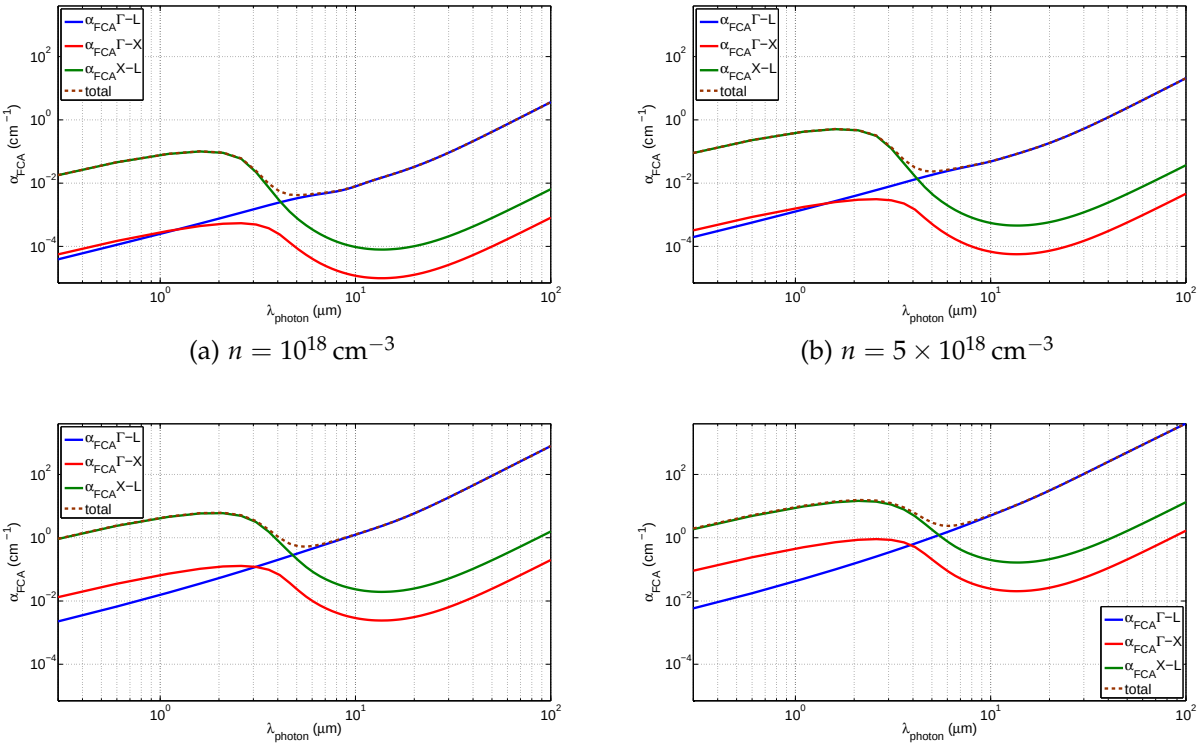

(a) $n = 10^{18}\,\mathrm{cm}^{-3}$ (b) $n = 5 \times 10^{18}\,\mathrm{cm}^{-3}$

(c) $n = 5 \times 10^{19}\,\mathrm{cm}^{-3}$ (d) $n = 10^{20}\,\mathrm{cm}^{-3}$

Figure 5.5: The free carrier absorption coefficient for intervalley electron transitions between the three conduction band valleys (Γ, *L* and *X*) as a function of the photon wavelength of doped bulk Ge with *n*-type concentration varying from 10^{18} to $10^{20}\,\mathrm{cm}^{-3}$, at 300 K.

5.3.2 *The n-type doping density effect*

In *n*-type bulk Ge, the majority of electrons will populate *L*-valleys because it is the lowest conduction band valley and it has larger effective mass than other conduction band valleys. Figure (5.5) illustrates the intervalley coefficients of the conduction band valleys for bulk Ge, in which the *n*-type doping concentration varies between 10^{18} and $10^{20}\,\mathrm{cm}^{-3}$.

As the doping density increases more electrons will populate Γ and X valleys. Therefore, one can say that by increasing the doping density for bulk Ge, all the intervalley absorption coefficients increase, but the transition between Γ and X shows the largest increase in the near infrared wavelength range.

The large relative change of $\Gamma \rightleftharpoons X$ scattering-induced absorption happens mostly for larger values of electron density, and arises from the strong increase of the Γ-valley population (whilst the population of the X state remains small). In contrast, the $\Gamma \rightleftharpoons L$ scattering-induced absorption mostly arises from electrons in the lowest, L valleys: this is where the majority of electrons reside and hence this absorption is expected to increase approximately linearly with electron density.

5.4 INTRAVALLEY FREE CARRIER ABSORPTION

When an electron absorbs a photon and both initial and final states belong to the same valley, the free carrier absorption is of the intravalley type. The intravalley FCA coefficient can be derived from the intervalley eq. (5.10) by putting $E_f = E_i$, $m_f = m_i$, and can thus be expressed as

$$\begin{aligned}
\alpha_{FCA} &= \frac{e^2 k_B T_c}{12\pi^3 n_r c \varepsilon_0 \omega_t^3 \hbar^4} \int_0^\infty dq\, q^3\, V_n\, |M_q|^2 \\
&\times \left\{ \frac{N_q}{\exp(-\varepsilon_q - \varepsilon_t) - 1} \times \ln\left[\frac{1 + \exp(\eta - \varepsilon_q - \varepsilon_t - \varepsilon_{--}^{\min})}{1 + \exp(\eta - \varepsilon_{--}^{\min})} \right] \right. \\
&+ \frac{N_q + 1}{\exp(\varepsilon_q - \varepsilon_t) - 1} \times \ln\left[\frac{1 + \exp(\eta + \varepsilon_q - \varepsilon_t - \varepsilon_{+-}^{\min})}{1 + \exp(\eta - \varepsilon_{+-}^{\min})} \right] \\
&- \frac{N_q}{\exp(-\varepsilon_q + \varepsilon_t) - 1} \times \ln\left[\frac{1 + \exp(\eta - \varepsilon_q + \varepsilon_t - \varepsilon_{-+}^{\min})}{1 + \exp(\eta - \varepsilon_{-+}^{\min})} \right] \\
&- \left. \frac{N_q + 1}{\exp(\varepsilon_q + \varepsilon_t) - 1} \times \ln\left[\frac{1 + \exp(\eta + \varepsilon_q + \varepsilon_t - \varepsilon_{++}^{\min})}{1 + \exp(\eta - \varepsilon_{++}^{\min})} \right] \right\} \quad (5.17)
\end{aligned}$$

where

$$k_{\pm\pm}^{min} = \left| q/2 + m_c E_{\pm\pm}/\hbar^2 q \right|$$

$$E_{\pm\pm} = \pm\hbar\omega_q \pm \hbar\omega_t.$$

In this process, two types of phonons (acoustic and optical) can contribute to the intravalley FCA, as well as charged impurity scattering [13].

5.4.1 *Acoustic Phonon intravalley absorption*

The acoustic phonon model used here is valid for low wavevector acoustic phonons, with the linear dispersion expression $\omega_q = q \times \nu_s$. The sound

velocity in Ge (v_s) has transverse (v_t) and longitudinal (v_l) components, which have values of 3.61×10^5 cm/sec and 5.31×10^5 cm/sec, respectively. The average velocity of sound is calculated from $v_s = \left(2v_t + v_l\right)/3$ [103].

The interaction matrix element between carriers and acoustic phonons in eq. (5.17) is defined as

$$|M_q|^2 = \frac{D_A^2 \hbar q^2}{2\rho\omega_q V_n}, \tag{5.18}$$

where D_A is the deformation potential of the acoustic phonons for the corresponding valley [13].

5.4.2 *Optical Phonon intravalley absorption*

The intravalley optical phonon scattering is only allowed in the L valley and is forbidden in the X and Γ valleys in Ge due to the symmetry of the system [106].

The carrier-optical phonon interaction element from eq. (5.17) is given by

$$|M_q|^2 = \frac{\hbar^2 D_{opt}^2}{2\rho V_n \hbar\omega_{opt}}, \tag{5.19}$$

where D_{opt} is the optical phonon deformation potential for the L valley [13]. In Ge, $D_{opt}^L = 5.5 \times 10^8$ eV/cm, with a respective optical phonon energy $\hbar\omega_{opt} = 37.04$ meV [104].

5.4.3 *Charged impurity Intravalley absorption*

The interaction matrix element for electron-charged impurity scattering is

$$|M_q|^2 = \frac{Z_i^2 e^4 n_e^i}{\varepsilon_s^2 V_n \left(q^2 + q_s^2\right)^2}, \tag{5.20}$$

where Z_i is the ionized impurity charge, n_e^i is the impurity density, the static permittivity is $\varepsilon_s = \varepsilon_0 K_s$, K_s is the static dielectric constant and the static screening wavevector is $q_s = \left(\frac{e^2}{\varepsilon_s}\frac{\partial n_e}{\partial E_F}\right)^{1/2}$ [13].

5.4.4 *Intravalley absorption results*

Since the intravalley transitions occur between states in the same valley, the variation of the doping density is the only effect in this case, while the strain condition does not affect the intravalley FCA coefficient. Figure (5.6) shows the acoustic phonon, optical phonon and charged impurity contributions to intravalley absorption in bulk Ge at room temperature. Similarly to the intervalley cases, the intravalley absorption increases with increasing carrier density in the conduction band. The impurity-based absorption has a much stronger dependence on carrier density than the other phonon absorption types, because increasing the number of dopants increases number of 'scatterers', *i.e.* the total strength of the interaction, and also increases the number of electrons which these dopants released and which give rise to absorption. The acoustic phonons give a larger absorption coefficient than the optical phonons for n-type bulk Ge. The applied strain has no effect on the intravalley FCA coefficient for doped bulk Ge.

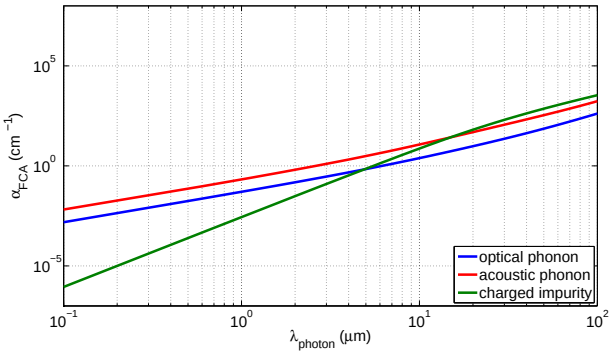

(a) $n = 1 \times 10^{18}\,\mathrm{cm}^{-3}$

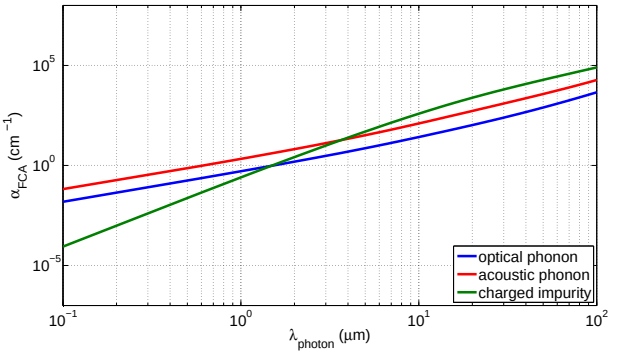

(b) $n = 10^{19}\,\mathrm{cm}^{-3}$

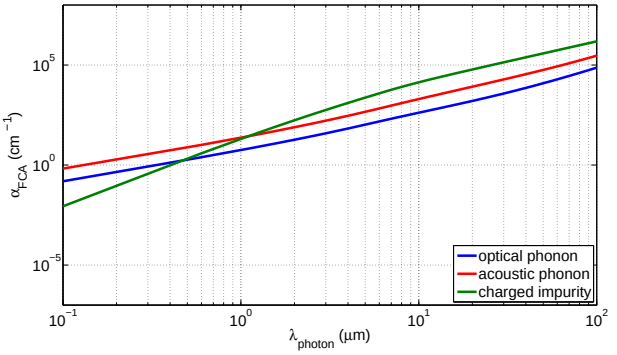

(c) $n = 1 \times 10^{20}\,\mathrm{cm}^{-3}$

Figure 5.6: The acoustic, optical phonon and charged impurity intravalley FCA for bulk Ge at 300 K.

5.5 THE TOTAL FCA

The relative importance of different processes, and the dependence of absorption on electron density and strain, is decided by a complicated interplay of variable populations of different valleys due to their relative energy positions and Fermi-Dirac population effects, changes of screening length for impurity scattering, etc. Therefore only numerical calculations can identify the significant processes that determine the absorption for a particular wavelength.

From the previous discussion, carrier concentration plays a more significant role for the intravalley and intervalley absorption transitions; the applied strain has effect only on the intervalley absorption transitions. Summing the intervalley and intravalley absorption FCA coefficients will give the total free carrier absorption coefficient, which can give the full picture of the bulk Ge FCA spectrum dependence on the biaxial tensile strain condition, carrier concentration and temperature.

Figure (5.7) summarises the variation of the total FCA coefficient for [001] bulk Ge with n-type doping of $n = 10^{18}$, 5×10^{18}, 10^{19}, 5×10^{19} and $10^{20}\,\mathrm{cm}^{-3}$, and biaxial tensile strain with $\varepsilon_{||} = 0$, 0.5, 1.5 and 2 %. The FCA coefficient increases approximately linearly with the n-type doping increase, whilst it is only weakly dependent on the applied strain. Increasing the temperature from room temperature to a typical device temperature (about 353 K) does not affect the FCA coefficient much for any case with the same doping and strain condition. Figure 5.7 the solid (dashed) lines represent the FCA coefficient at 300 K (353 K). The absorption is generally expected to increase with temperature because of increasing phonon population, and also because of broadening of the electron distribution, meaning that more final states become available at higher temperatures.

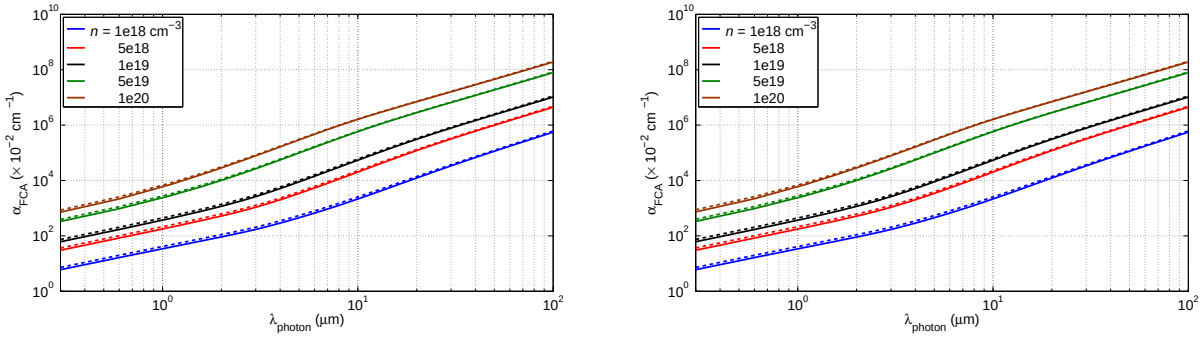

(a) $\varepsilon_{||} = 0.0\,\%$ (b) $\varepsilon_{||} = 0.5\,\%$

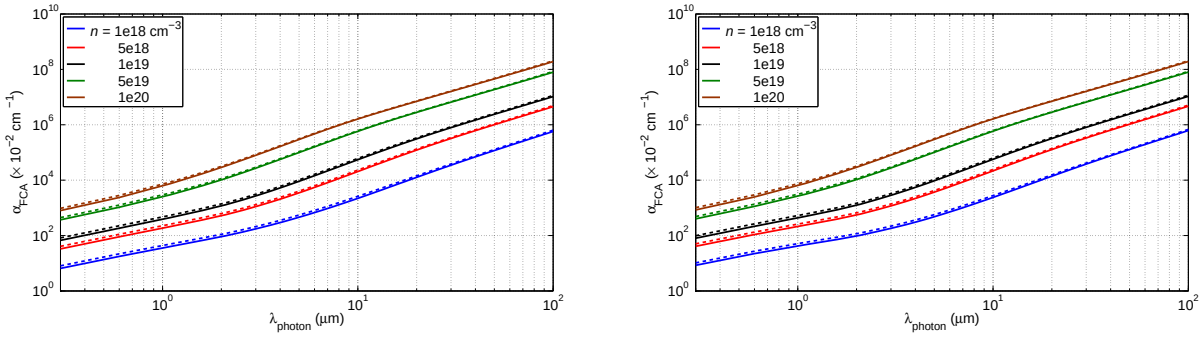

(c) $\varepsilon_{||} = 1.5\,\%$ (d) $\varepsilon_{||} = 2.0\,\%$

Figure 5.7: The total free carrier absorption coefficient spectra for n-type doped strained bulk Ge at 300 (solid lines) and 353 K (dashed lines), the doping density varies from 10^{18} to $10^{20}\,\mathrm{cm}^{-3}$, and the biaxial tensile strain values are $\varepsilon_{||} = 0$, 0.5, 1.5 and 2 %.

5.6 THE NET GAIN

The interband gain and intervalence band absorption have been presented for [001] bulk Ge in the previous chapter 4. The effect of introduce different n-type doping and injected carrier densities on the total gain for strained bulk Ge have also been performed and discussed. The total gain which has been presented earlier is the sum of the interband gain and IVBA only. Here in this section the result of the net gain - the sum of the interband gain, IVBA and FCA - will be discussed for the similar conditions of carrier density and applied strain. Previous results showed that the interband gain and the IVBA increase with carrier density and the applied tensile strain. The interband gain (IVBA) peaks show red (blue) shifts with the applied strain. Adding the FCA to the calculations will give results for the overall net gain of bulk Ge under such controlled conditions of doping and tensile strain, at room and typical device temperatures.

5.6.1 *Dependence of the net gain on electron density*

The net gain calculations were performed for 1 and 2 % biaxial tensile strained n-type bulk Ge to investigate the variation of the net gain with different electron and hole concentrations in the conduction and valence band, respectively. The total electron density has values of $n = 10^{18}$, 5×10^{18}, 10^{19}, 5×10^{19} and $10^{20}\,\mathrm{cm}^{-3}$, while the injected carriers remain fixed at $n_{inj} = 10^{18}\,\mathrm{cm}^{-3}$ in tensile strained bulk Ge.

The calculated net gain spectra for 1 and 2 % biaxial tensile strained Ge in the mentioned range of electron and injected concentrations is shown in figures (5.8) and (5.9), respectively. These results show that the inverse relation of FCA with photon energy diminishes the net gain peak. However, a significant net gain is still predicted for 2 % strain.

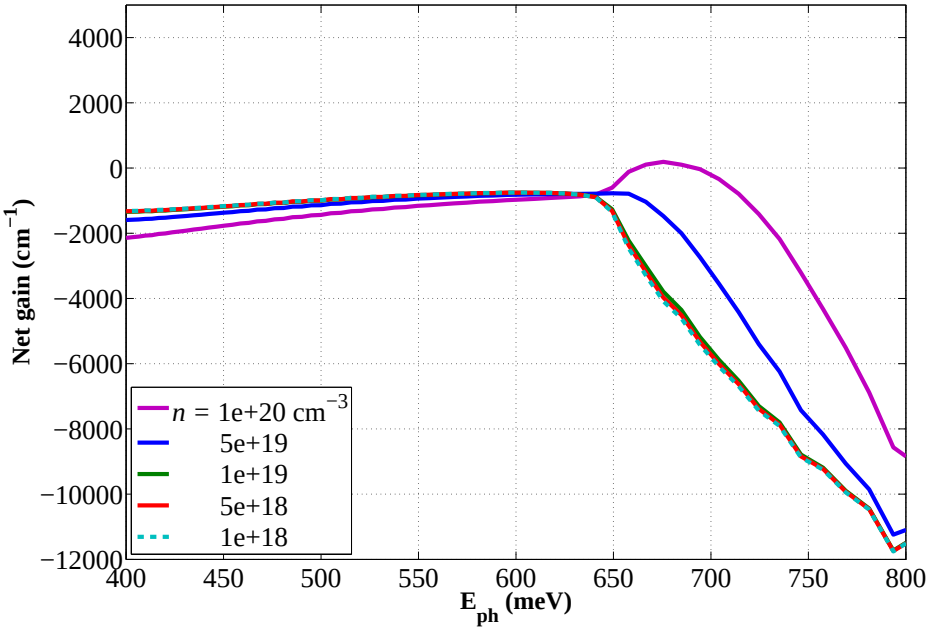

Figure 5.8: The net gain spectra for 1 % tensile strained [001] Ge with $10^{18}\,\mathrm{cm}^{-3}$ injected carriers, and the total electron density varying from $n = 10^{18}$ to $10^{20}\,\mathrm{cm}^{-3}$, at room temperature.

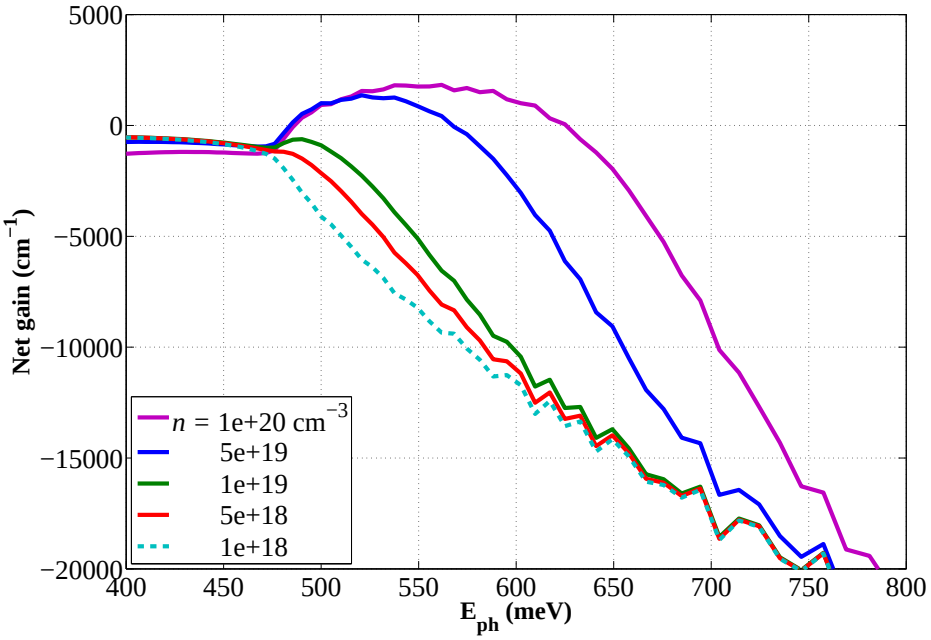

Figure 5.9: The net gain spectra for 2 % tensile strained [001] Ge with $10^{18}\,\mathrm{cm}^{-3}$ injected carriers, and the total electron density varying from $n = 10^{18}$ to $10^{20}\,\mathrm{cm}^{-3}$, at room temperature.

5.6.2 *Dependence of the net gain on hole density*

In this section, the net gain spectra were calculated for biaxially tensile strained bulk Ge with the total electron density in the C.B. fixed at $5 \times 10^{19}\,\mathrm{cm}^{-3}$. The injected carriers vary and the hole concentration has values $p = 10^{18}$, 5×10^{18}, 10^{19}, 5×10^{19} and $10^{20}\,\mathrm{cm}^{-3}$.

Figures (5.10) and (5.11) show the calculated net gain spectra for 1 and 2 % biaxial tensile strained Ge for the above mentioned fixed total electron and injected carrier concentrations, respectively. The net gain decreases as the injected carrier density increases generally in this case as the C.B. is heavily populated with electron, and so increasing the injected carriers concentration mainly increases the IVBA.

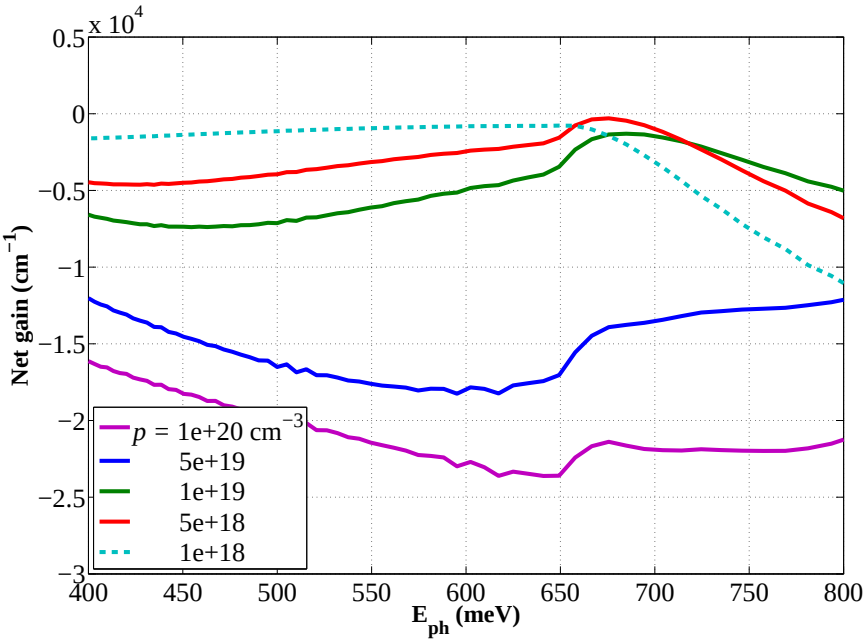

Figure 5.10: The net gain spectra for 1 % tensile strained [001] Ge with $5 \times 10^{19}\,\mathrm{cm}^{-3}$ total electron density, and the injected carriers varying from $n = 10^{18}$ to $10^{20}\,\mathrm{cm}^{-3}$, at room temperature.

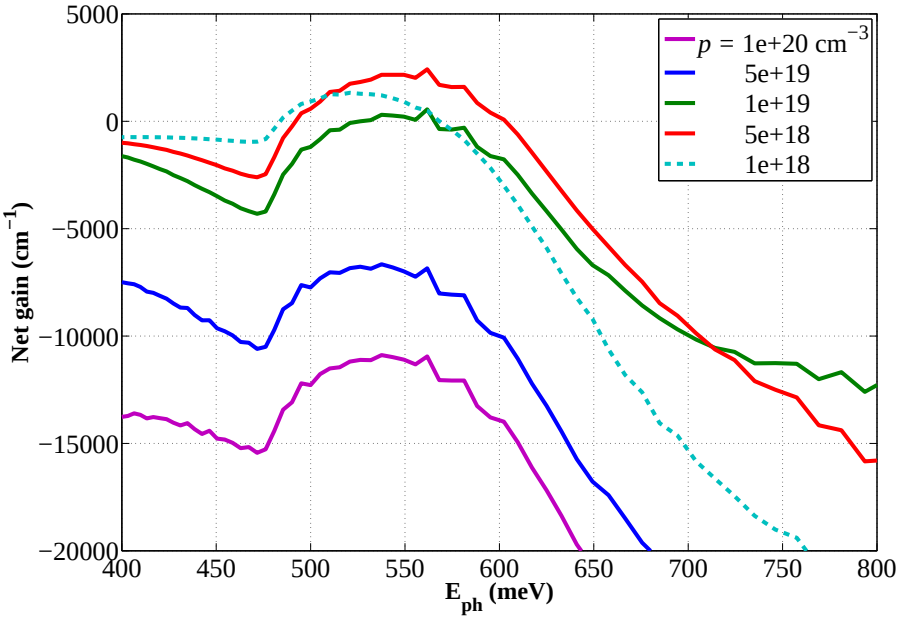

Figure 5.11: The net gain spectra for 2 % tensile strained [001] Ge with 5×10^{19} cm^{-3} total electron density, and the injected carriers varying from $n = 10^{18}$ to 10^{20} cm^{-3}, at room temperature.

5.6.3 *Bulk Ge net gain as a function of the applied tensile strain*

The net gain calculations show that there is no net gain peak for [001] Ge when the total electron and hole concentrations are the same, which is the case of having injected carriers only. In section (5.6.1) and (5.6.2), the net gain appears for controlled, unequal electron and hole concentrations for (1 and) 2 % tensile strain bulk Ge. In order to study the variation of the net gain from the applied strain perspective, the net gain spectra were calculated for a number of strain values, for the same controlled carrier concentrations. The applied biaxial tensile strain has values of $\varepsilon_{||} = 0.0$, 0.5 and 1.5 %, at room temperature.

Figure (5.12) summarizes the peak value of the net gain as a function of the applied tensile strain for [001] Ge, for a low fixed injected carrier concentration (10^{18} cm^{-3}) while the total electron concentration varies. Positive net gain occurs for high electron densities ($\geq 5 \times 10^{19}$ cm^{-3}). Furthermore, the

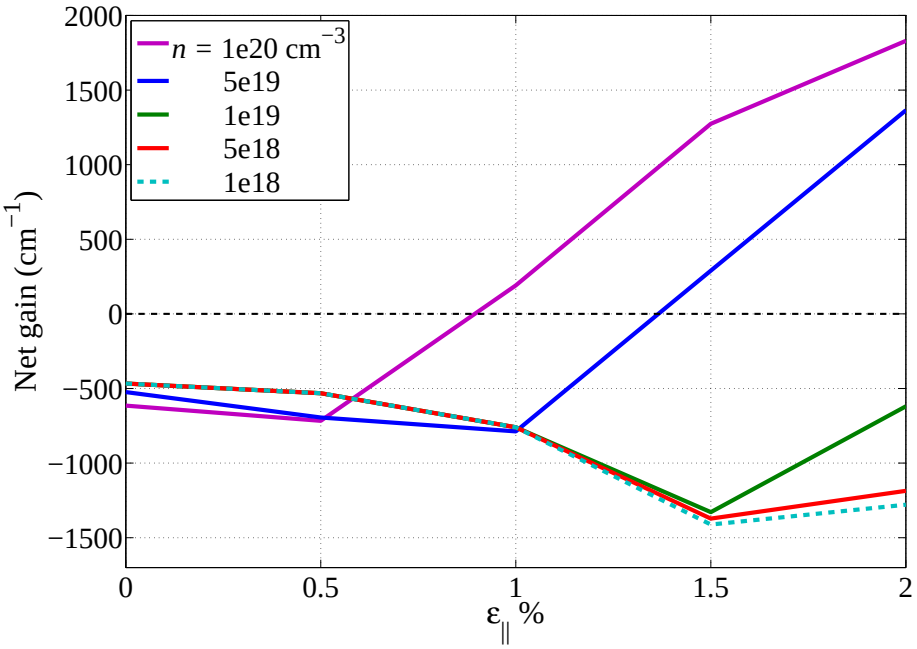

Figure 5.12: The net gain peak for [001] Ge as a function of the applied strain for a total electron varying density from 10^{18} to 10^{20}cm^{-3}, and 10^{18}cm^{-3} injected carriers, at 300 K.

total electron density pushes the net gain to smaller tensile strain values for [001] Ge. In figure (5.13), the net gain is shown as a function of applied strain for [001] Ge with a fixed total electron density ($\geq 5 \times 10^{19}\,\text{cm}^{-3}$) and a varying injected carrier density. Figure (5.13) shows that net gain is impossible for large injected carrier densities, due to the large IVBA.

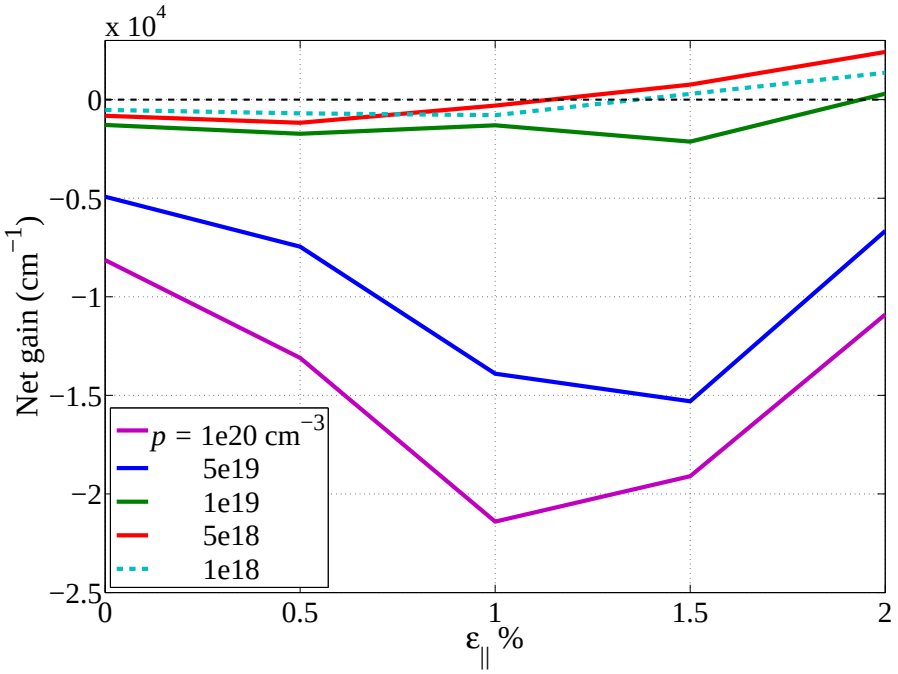

Figure 5.13: The net gain peak for [001] Ge as a function of the applied strain for fixed total electron density at $5 \times 10^{19}\text{cm}^{-3}$, and a hole density varying from 10^{18}-10^{20}cm^{-3} injected carriers, at 300 K.

5.6.4 *Net gain and temperature dependence*

Realistic device temperature (as 353 K) have also been considered in the net gain calculation. Figure (5.14) and (5.15) show the net gain as a function of the applied tensile strain for [001] Ge for the above-mentioned carrier densities. The net gain has an inverse dependence on the temperature. More strain is required to have net gain for [001] Ge under the same conditions, as the direct band gap energy decreases with increasing temperature.

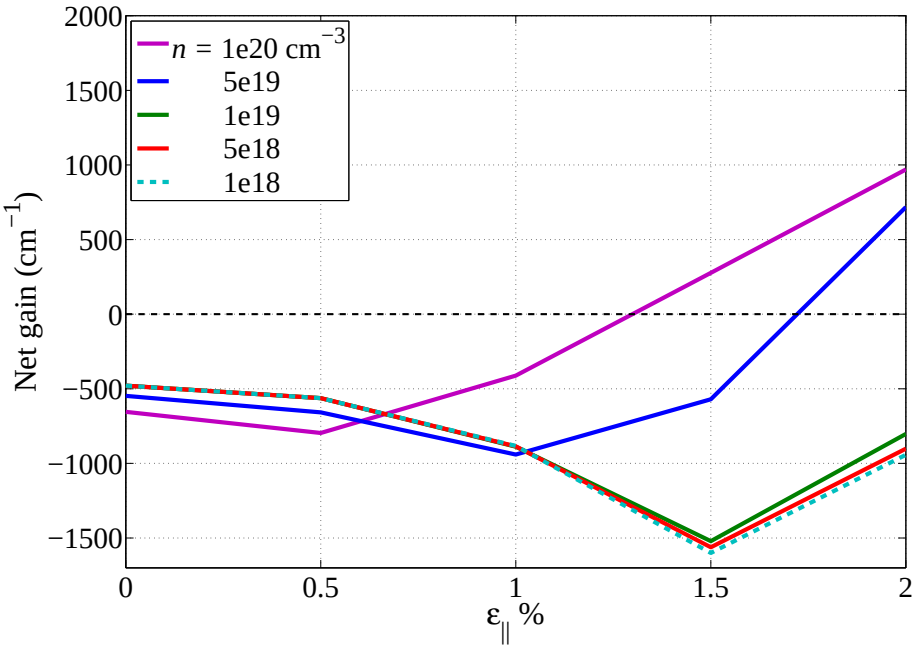

Figure 5.14: The net gain peak for [001] Ge as a function of the applied strain for a total electron density varying from 10^{18} to 10^{20}cm^{-3}, and 10^{18}cm^{-3} injected carriers, at 353 K.

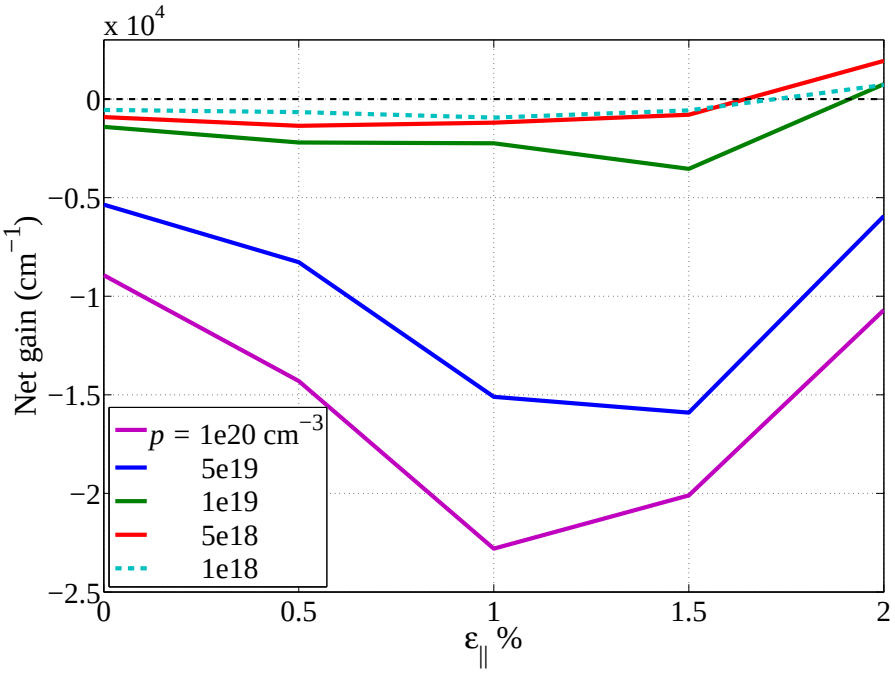

Figure 5.15: The net gain peak for [001] Ge as a function of the applied strain for a fixed total electron density of 5×10^{19}cm^{-3} and a hole density varying from 10^{18}-10^{20}cm^{-3} as injected carriers, at 353 K.

5.7 CONCLUSION

A theory of free carrier absorption in semiconductors has been presented. The methodology of free carrier absorption coefficient calculation for both intervalley and intravalley in [001] Ge has been demonstrated. The intervalley FCA calculation shows the importance of including the X-valleys in FCA at short wavelengths. The charged impurities dominate the FCA spectra in the case of large n-type doping density, and has its minima in the case of carriers in Ge coming from injection only. The intravalley FCA is larger than the intervalley FCA for Ge over the wavelength range considered here. The applied strain engineers the band structure which changes the FCA between different valleys, yet the total FCA for [001] Ge is not affected much by the applied tensile strain. A large total electron density is essential for [001] Ge interband gain for any tensile strain value. There are two ways to obtain such a large electron density: the first one is by n-type doping which has the disadvantage that the FCA increases. The second method is by injected carriers but the IVBA dominates the interband gain spectra for Ge for large injected carrier densities. Both the n-type doping and injected carriers can be varied independently to find the optimum net gain for strained Ge. The net gain calculation shows that a low injected carrier densities (about 10^{18}cm^{-3}) and high n-type doping ($\geq 10^{20}\text{cm}^{-3}$) is required to have net gain for biaxial tensile strain larger than $\varepsilon_{||} = 0.9\,\%$. The FCA is only weakly dependent on temperature. Increasing the temperature leads to larger strain required to obtain the net gain for [001] Ge for any given electron and hole densities.

6

CONCLUSION

Literature review shows that an electrically pumped Ge laser is the missing link in Si technology, where the need exists for optoelectronic integrated circuits. Ge may be used as an optical semiconductor material because of its CMOS compatibility and because it has a fast radiative recombination rate from its direct band transition, with the emitted light wavelength being within the communications band at room temperature. Despite the fact that Ge has an indirect band gap, applying strain can engineer the Ge band structure [8, 12].

The effect of applying biaxial compressive and tensile strain on conduction and valence band edges of Ge grown in different orientations, [001], [110] and [111] has been analysed. The direct band gap energy increases with the applied compressive strain and decreases with tensile strain for bulk Ge grown in all three orientations. The different response of the indirect conduction and the valence band edges and lifting of their degeneracy according to the applied strain conditions can be used to make Ge a direct band gap semiconductor material. The effect of uniaxial compressive and tensile strain on the band structure energy for Ge layers grown on the three orientations has also been addressed. The biaxially strained [100] Ge requires the smallest tensile strain value (about 1.7 %) for achieving a

direct band gap amongst the investigated strain and growth orientation conditions.

An investigation of the combination of the applied strain and doping density to make Ge behave as a direct band gap material, and have a good injection efficiency, was carried out at 0 K, for both bulk like Ge and Ge quantum wells of different widths. Such calculations are essential to establish a background understanding for the behaviour of Ge under different strain and growth orientation conditions. For moderate tensile strain values, bulk Ge and Ge quantum wells on [111] substrates have the advantage over other cases, due to the lifting the degeneracy of the four L-valleys which will pull more quantized states upwards with tensile strain. Applying uniaxial strain for [110] Ge is the best choice for keeping the emitted wavelength within the communications band. The electron injection efficiency into the Γ-valley is much larger for Ge quantum wells than for bulk Ge. Yet, it is not the case at finite temperature, as further calculations, using the same procedure, show that bulk Ge has larger injection efficiency than Ge quantum wells.

At finite temperatures, the 8×8 $\mathbf{k}.\mathbf{p}$ method and effective mass approximation were used to calculate the energy bands for [001] bulk Ge and the quasi-Fermi levels for given values of carrier densities, and then the interband gain and IVBA were calculated for biaxially tensile strained [001] bulk Ge. The effect of unequal electron and hole densities required to achieve the interband gain and reduce the IVBA has been investigated for strained bulk n^+ Ge at room and typical device temperatures.

A detailed description of the free carrier absorption (FCA) coefficient calculation, accounting for both intervalley and intravalley scattering in strained [001] Ge has been given. The dependence of FCA on the biaxial tensile strain, on the electron and hole densities and on temperature has been calculated for [001] Ge. The intervalley FCA calculation shows the importance

of including the *X*-valleys in FCA at short wavelengths. Higher *n*-type doping is not desirable due to the domination of charged impurity mediated absorption in this case.

This work finds that, in order to obtain net gain in [001] bulk Ge subjected to different strain conditions, grown on different substrate orientations and at finite temperatures, the following points must be considered:

1. The degeneracy lifting, partial or full, for indirect valleys which were equivalent under no-strain conditions, depending on their orientation in respect to characteristic directions of the system.
2. Their different energy dependence on the increasing strain.
3. The distribution of electron and hole densities over bands and valleys is found to vary considerably with the value of strain, its type and growth direction.
4. The *L*-valleys will be populated by the majority of electrons.
5. Even with a small occupancy, the *X*-valleys must not be neglected.
6. A large total electron density (via doping and carrier injection) is essential for [001] Ge interband gain for any tensile strain value.
7. A relatively small density of injected (carriers) holes is essential to keep the IVBA low.
8. The FCA may be very large for high values of *n*-type doping.

Positive net gain can be obtained in Ge only if the total electron and hole densities are independently controlled and Ge is under sufficiently large biaxial tensile strain ($\varepsilon_{||} > 1\,\%$), and a suitable combination of these may be used to find the optimum balance of interband gain, IVBA, FCA. A small strain value $\varepsilon_{||} = 0.25\,\%$, which has been reported in ref. [107], is not sufficient to obtain net gain. Such conclusion is consistent with the experimental investigations that have been carried out recently and gives an explanation of their observations [72, 73]. They have reported that the

net gain did not appear in moderately strained (0.25 %) bulk Ge for neither low nor high injected carriers densities [72, 73]. Based on that, Ge laser can be achieve by introducing a suitable combination of a large enough tensile strain and independently controlled large electron and relatively small hole density.

6.1 FURTHER WORK

Knowledge of the effects of various strain conditions on the band structure of Ge, which may be grown in different substrate orientations, enables the model to be used for investigation of practical conditions for growth of Ge on Si, GeSi alloy, GeSn and any III-V alloy buffer layer. Then, this whole method can be implemented on different substrate orientations. Further investigations may be performed for different SiGe alloys (with a small percentage of Si), which should enable achieving somewhat shorter emission wavelengths than pure Ge can provide. This should produce the best alloy designs for a specified emission wavelength.

A further investigation of Auger recombination in Ge under the various carrier densities and strain conditions can be performed. Auger recombination does not have a direct influence on the gain (it depends only on carrier densities), but it affects the injection current required to achieve these densities.

The conditions required to achieve high carrier densities in a Ge pn heterojunction , which has a couple of layers with different doping or different alloy compositions, can be investigated in order to deliver structures with threshold currents as low as possible, find the spatial distribution of gain under non-uniform carrier densities conditions, etc.

In order to find the gain available for lasing (modal gain), waveguide modelling of heterostructure designed for large material gain should also be

performed, to design structures with good mode overlap between the laser optical mode and the active, amplifying part of the structure.

To improve the accuracy of modeling, some secondary effects such as indirect interband absorption/gain can be added.

Part I

APPENDIX

A

UNIAXIAL STRAINED Ge

Bending or stretching a wafer of a semiconductor material along one axis (uniaxial strain) of the in-plane coordinates (x or y), an in-plane strain ($\varepsilon_{||}$) takes place along the axis where the bending is applied (ε'_{xx}or ε'_{yy}), with two unknown strain tensor elements in the layer coordinate system [108]. One is the out-of-plane axis (ε'_{zz}), and the element of the other in-plane axis (ε'_{yy}or ε'_{xx}). Again, there are no shear strain elements (ε'_{xy}, ε'_{yz}, ε'_{xz}). Two of the stress tensor elements equal zero: the other in-plane stress element (σ'_{yy} or σ'_{xx}) and the out-of-plane element (σ'_{zz}), while the other tensor elements can be calculated. As in the case of biaxial strain, the unknown strain tensor diagonal elements can be determined by applying these conditions in different growth directions ($[001]$, $[110]$ and $[111]$) along the x and y axis. The energy shifts of all valleys will be determined.

The strain, in this appendix, was directed along the $[100]$ crystallographic axis for $[001]$ growth, along the $x' = [001]$ and $y' = [\overline{1}10]$ crystallographic axes for $[110]$ growth, and along the $x' = [\overline{1}10]$ or $y' = [11\overline{2}]$ crystallographic directions for $[111]$ growth, see fig. (A.1). The calculation of strain tensors and the energy shifts in the case of uniaxial strain along the x- and y-axes in the three growth directions ($[001]$, $[110]$ and $[111]$) will be summarised next.

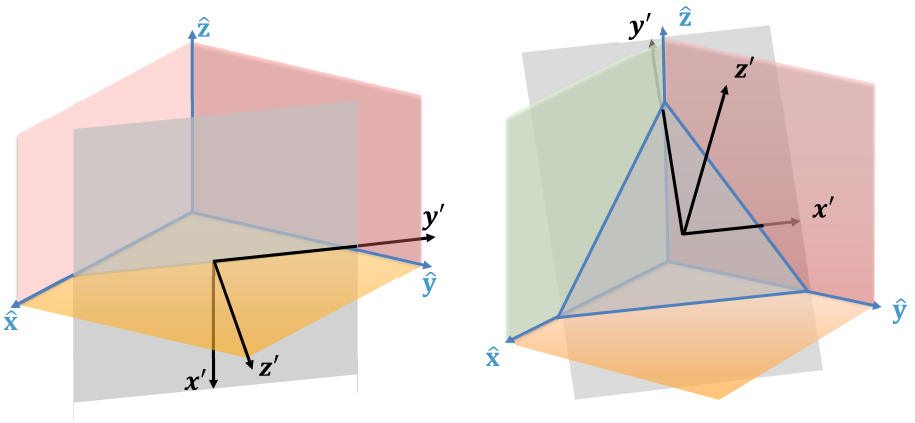

(a) Bending along x′ or y′.z′: [110], y′: [-110], x′: [00-1]

(b) Bending along **x**′ or **y**′.**z**′: [111], **x**′ : $[-110]$, **y**′: $[-1-12]$

Figure A.1: Scheme of the crystal coordinate system and for the new layer coordinate system, for [110] growth (left) and for [111] growth (right) and the bending axis of the applied uniaxial strain [15].

A.1 UNIAXIAL STRAIN ALONG x-AXIS.

The initial conditions of Uniaxial strain (U) and stress along x-axis (Ux) for Ge (or a semiconductor material has the zinc blende structure) $[001]$, $[110]$ and $[111]$ growth directions are:

$$\varepsilon'_{xx} = \varepsilon_{||};\ \varepsilon'_{xy} = \varepsilon'_{xz} = \varepsilon'_{yz} = 0;\ \sigma'_{yy} = \sigma'_{zz} = 0. \tag{A.1}$$

The strain tensor for the $[001]$ growth direction is:

$$\varepsilon_{[001]\mathrm{U}x} = \varepsilon_{||} \begin{bmatrix} 1 & 0 & 0 \\ 0 & -\frac{C_{12}}{C_{11}+C_{12}} & 0 \\ 0 & 0 & -\frac{C_{12}}{C_{11}+C_{12}} \end{bmatrix}, \tag{A.2}$$

for the $[110]$ growth direction is:

$$\varepsilon_{[110]\mathrm{U}x} = \varepsilon_{||} \begin{bmatrix} -\frac{C_{12}}{C_{11}+C_{12}} & 0 & 0 \\ 0 & -\frac{C_{12}}{C_{11}+C_{12}} & 0 \\ 0 & 0 & 1 \end{bmatrix}, \tag{A.3}$$

and for the (111) growth direction:

$$\varepsilon_{[111]\mathrm{U}x} = \frac{\varepsilon_{||}}{\varrho} \begin{bmatrix} \varrho_{xx} & -\varrho_{xi} & \varrho_{xi} \\ -\varrho_{xi} & \varrho_{yy} & \varrho_{xi} \\ \varrho_{xi} & \varrho_{xi} & \varrho_{zz} \end{bmatrix}, \tag{A.4}$$

where

$$\varrho = C_{11}^2 - 2C_{12}^2 + 16C_{44}^2 + 40C_{12}C_{44} + C_{11}\left(C_{12} + 26C_{44}\right), \tag{A.5}$$

$$\varrho_{xx} = \varrho_{yy} = 2C_{44}\left(5C_{11} + 4C_{12} + 8C_{44}\right), \tag{A.6}$$

$$\varrho_{zz} = 4C_{44}\left(2C_{11} + 7C_{12} - 4C_{44}\right), \tag{A.7}$$

$$\varrho_{xi} = \left(C_{11} + 2C_{12}\right)\left(C_{11} - C_{12} + 16C_{44}\right), \tag{A.8}$$

For uniaxial strain along x-axis the energy shift for the growth direction [001] for the Γ-valley is:

$$\Delta E^{\Gamma}_{[001]\mathrm{U}x} = \Xi^{\Gamma}_{d} \frac{C_{11} - C_{12}}{C_{11} + C_{12}} \varepsilon_{||}, \tag{A.9}$$

for the degenerate X-valleys the energy shifts are:

$$\Delta E^{X_1}_{[001]\mathrm{U}x} = \left(\frac{C_{11} - C_{12}}{C_{11} + C_{12}} \Xi^{X}_{d} + \Xi^{X}_{u} \right) \varepsilon_{||}, \tag{A.10}$$

$$\Delta E^{X_{2,3}}_{[001]\mathrm{U}x} = \frac{(C_{11} - C_{12})\,\Xi^X_d - C_{12}\Xi^X_u}{C_{11} + C_{12}}\varepsilon_{||}, \tag{A.11}$$

and for the degenerate L-valleys:

$$\Delta E^{L}_{[001]\mathrm{U}x} = \frac{1}{3}\frac{(C_{11} - C_{12})\,\left(3\Xi^L_d + \Xi^L_u\right)}{C_{11} + C_{12}}\varepsilon_{||}. \tag{A.12}$$

In the case of the [110] growth direction along x-axis, the energy shift of Γ-valley is:

$$\Delta E^{\Gamma}_{[110]\mathrm{U}x} = \Delta E^{\Gamma}_{[001]\mathrm{U}x}, \tag{A.13}$$

for the degenerate X-valleys:

$$\Delta E^{X_{1,2}}_{[110]\mathrm{U}x} = \Delta E^{X_{2,3}}_{[001]\mathrm{U}x}, \tag{A.14}$$

$$\Delta E^{X_3}_{[110]\mathrm{U}x} = \Delta E^{X_1}_{[001]\mathrm{U}x}, \tag{A.15}$$

and for the degenerate L-valleys:

$$\Delta E^{L}_{[001]\mathrm{U}x} = \Delta E^{L}_{[001]\mathrm{U}x}. \tag{A.16}$$

In the case of the [111] growth direction, the energy shift of Γ-valley is:

$$\Delta E^{\Gamma}_{[111]\mathrm{U}x} = 12\Xi^{\Gamma}_d\frac{C_{44}\,(C_{11} - C_{12} + 4C_{44})}{\varrho}\varepsilon_{||}, \tag{A.17}$$

for the degenerate X-valleys:

$$\Delta E^{X_{1,2}}_{[111]\mathrm{U}x} = 2C_{44}\frac{(6C_{11} - 6C_{12} + 24C_{44})\,\Xi^X_d + (5C_{11} + 4C_{12} + 8C_{44})\,\Xi^X_u}{\varrho}\varepsilon_{||}, \tag{A.18}$$

$$\Delta E^{X_3}_{[111]\mathrm{U}x} = 4C_{44}\frac{\left(3C_{11}-3C_{12}+12C_{44}\right)\Xi^X_d + \left(2C_{11}+7C_{12}+4C_{44}\right)\Xi^X_u}{\varrho}\varepsilon_{||}, \tag{A.19}$$

and for the degenerate L-valleys:

$$\Delta E^{L_1}_{[111]\mathrm{U}x} = 2\left(C_{11}-C_{12}+4C_{44}\right)\frac{C_{44}\Xi^L_d - \left(C_{11}+2C_{12}-2C_{44}\right)\Xi^L_u}{\varrho}\varepsilon_{||}, \tag{A.20}$$

$$\Delta E^{L_2}_{[111]\mathrm{U}x} = \left(\frac{2\Xi^L_u}{3} - 4C_{44}\frac{9\left(C_{12}-4C_{44}-C_{11}\right)\Xi^L_d + \left(43C_{12}-4C_{44}+20C_{11}\right)\Xi^L_u}{3\varrho}\right)\varepsilon_{||}, \tag{A.21}$$

$$\Delta E^{L_{3,4}}_{[111]\mathrm{U}x} = \left(\frac{2\Xi^L_u}{3} - 4C_{44}\frac{9\left(C_{12}-4C_{44}-C_{11}\right)\Xi^L_d + \left(7C_{12}-4C_{44}+2C_{11}\right)\Xi^L_u}{3\varrho}\right)\varepsilon_{||}. \tag{A.22}$$

A.2 UNIAXIAL STRAIN ALONG y-AXIS.

The initial conditions of uniaxial strain and stress along y-axis (Uy) in [001], [110] and [111] growth directions are:

$$\varepsilon^{'}_{yy} = \varepsilon_{||};\ \varepsilon^{'}_{xy} = \varepsilon^{'}_{xz} = \varepsilon^{'}_{yz} = 0;\ \sigma^{'}_{xx} = \sigma^{'}_{zz} = 0. \tag{A.23}$$

The strain tensor for the [001] growth direction:

$$\varepsilon_{[001]\mathrm{U}y} = \varepsilon_{||} \begin{bmatrix} -\frac{C_{12}}{C_{11}+C_{12}} & 0 & 0 \\ 0 & 1 & 0 \\ 0 & 0 & -\frac{C_{12}}{C_{11}+C_{12}} \end{bmatrix}, \tag{A.24}$$

and for the [001] growth direction:

$$\varepsilon_{[110]\mathrm{U}y} = \frac{\varepsilon_{||}}{\varsigma} \begin{bmatrix} 2C_{11}C_{44} & \varsigma_{xy} & 0 \\ \varsigma_{xy} & 2C_{11}C_{44} & 0 \\ 0 & 0 & -4C_{11}C_{44} \end{bmatrix}, \tag{A.25}$$

where

$$\varsigma_{xy} = -C_{11}^2 + 2C_{12}^2 - C_{11}C_{12}, \tag{A.26}$$

$$\varsigma = -\varsigma_{xy} + 2C_{11}C_{44}, \tag{A.27}$$

and for the [111] growth direction:

$$\varepsilon_{[111]\mathrm{U}y} = \frac{\varepsilon_{||}}{\iota} \begin{bmatrix} \iota_{xx} & \iota_{xy} & \iota_{iz} \\ \iota_{xy} & \iota_{xx} & \iota_{iz} \\ \iota_{iz} & \iota_{iz} & \iota_{zz} \end{bmatrix}, \tag{A.28}$$

where

$$\iota = C_{11}^2 - 2C_{12}^2 + 16C_{44}^2 + 40C_{12}C_{44} + C_{11}\left(C_{12} + 26C_{44}\right), \tag{A.29}$$

$$\iota_{xx} = -2C_{44}^2\left(C_{11} + 8C_{12} - 8C_{44}\right), \tag{A.30}$$

$$\iota_{zz} = 4C_{44}^2 \left(4C_{11} + 5C_{12} - 4C_{44}\right), \tag{A.31}$$

$$\iota_{xy} = \left(C_{11} + 2C_{12}\right)\left(C_{12} - C_{11} + 8C_{44}\right), \tag{A.32}$$

$$\iota_{iz} = \left(C_{11} + 2C_{12}\right)\left(C_{11} - C_{12} + 10C_{44}\right). \tag{A.33}$$

For uniaxial strain along y-axis the energy shift for the [001] growth direction for the Γ-valley is:

$$\Delta E^{\Gamma}_{[001]\mathrm{U}y} = \Delta E^{\Gamma}_{[110]\mathrm{U}x}, \tag{A.34}$$

for the degenerate X-valleys:

$$\Delta E^{X_{1,3}}_{[001]\mathrm{U}y} = \Delta E^{X_{1,2}}_{[110]\mathrm{U}x}, \tag{A.35}$$

$$\Delta E^{X_2}_{[001]\mathrm{U}y} = \Delta E^{X_3}_{[110]\mathrm{U}x}, \tag{A.36}$$

and for the degenerate L-valleys:

$$\Delta E^{L}_{[001]\mathrm{U}y} = \Delta E^{L}_{[110]\mathrm{U}x}. \tag{A.37}$$

In the case of the [110] growth direction, the energy shift of the Γ-valley is:

$$\Delta E^{\Gamma}_{[110]\mathrm{U}y} = \frac{4C_{44}\left(C_{11} - C_{12}\right)}{\varsigma}\Xi^{\Gamma}_{d}\varepsilon_{||}, \tag{A.38}$$

for the degenerate X-valleys:

$$\Delta E^{X_{1,2}}_{[110]\mathrm{U}x} = 4C_{44}\frac{2\left(C_{11} - C_{12}\right)\Xi^{X}_{d} + C_{11}\Xi^{X}_{u}}{\varsigma}\varepsilon_{||}, \tag{A.39}$$

$$\Delta E^{X_3}_{[110]\mathrm{U}x} = 4C_{44}\frac{\left(C_{11}-C_{12}\right)\Xi^X_d + C_{12}\Xi^X_u}{\varsigma}\varepsilon_{||}, \tag{A.40}$$

and for the degenerate L-valleys:

$$\Delta E^{L_{1,2}}_{[110]\mathrm{U}y} = 2\left(C_{11}-C_{12}\right)\frac{6C_{44}\Xi^L_d - \left(C_{11}+2C_{12}-2C_{44}\right)\Xi^L_u}{3\varsigma}\varepsilon_{||}, \tag{A.41}$$

$$\Delta E^{L_{3,4}}_{[110]\mathrm{U}y} = \frac{2}{3}\frac{\left(\varsigma-2C_{12}C_{44}\right)\Xi^L_d - 6C_{44}\left(C_{11}+C_{12}\right)\Xi^L_u}{3\varsigma}\varepsilon_{||}. \tag{A.42}$$

In the case of the [111] growth direction, the energy shift of the Γ-valley is:

$$\Delta E^{\Gamma}_{[111]\mathrm{U}y} = \Delta E^{\Gamma}_{[111]\mathrm{U}x}, \tag{A.43}$$

for the degenerate X-valleys:

$$\Delta E^{X_{1,2}}_{[111]\mathrm{U}y} = \frac{2C_{44}\left(6C_{11}-6C_{12}+24C_{44}\right)\Xi^X_d + \iota_{xx}\Xi^X_u}{\varsigma}\varepsilon_{||}, \tag{A.44}$$

$$\Delta E^{X_3}_{[111]\mathrm{U}y} = 4C_{44}\frac{\left(3C_{11}-3C_{12}+12C_{44}\right)\Xi^X_d + \left(4C_{11}+5C_{12}+4C_{44}\right)\Xi^X_u}{\varsigma}\varepsilon_{||}, \tag{A.45}$$

and for the degenerate L-valleys:

$$\Delta E^{L_1}_{[111]\mathrm{U}y} = 2\left(C_{11}-C_{12}+4C_{44}\right)\frac{6C_{44}\Xi^L_d - \left(C_{11}+2C_{12}-2C_{44}\right)\Xi^L_u}{\varsigma}\varepsilon_{||}, \tag{A.46}$$

$$\Delta E^{L_2}_{[111]\mathrm{U}y} = \left(\frac{2\Xi^L_u}{3} + 4C_{44} \frac{(5C_{12} + 4C_{44} + 4C_{11})\,\Xi^L_u + (9C_{11} - 9C_{12} + 36C_{44})\,\Xi^L_d}{3\varsigma} \right) \varepsilon_{||}, \tag{A.47}$$

$$\Delta E^{L_{3,4}}_{[111]\mathrm{U}y} = \left(\frac{2\Xi^L_u}{3} - 4C_{44} \frac{(40C_{12} - 36C_{44} - 9C_{11})\,\Xi^L_u + (14C_{12} - 4C_{44})\,\Xi^L_d}{3\varsigma} \right) \varepsilon_{||}. \tag{A.48}$$

A.3 THE C.B. AND V.B. VALLEY EDGES AND UNIAXIAL STRAIN

In the case of applying uniaxial strain along the x-axis of [001], and [110] bulk Ge and along the y-axis of [001] bulk Ge the conduction band behaves in the same way. The conduction band energy at Γ, the fourfold X-valleys, and the eight half L-valleys decrease with tensile and increase with compressive strain. The energy of the fourfold X-valleys is shifted slightly more than the eight half L-valleys, and less than the Γ-valley. On the other hand, the non-degenerate X-valley has a positive slope, which changes significantly with the applied strain. Germanium becomes a direct band gap semiconductor at 4.6% tensile strain in these cases, as shown in fig. (A.2).

They are two main differences between these three cases. Firstly, the twofold X-valleys in case of [001], and [110] Ge uniaxially strained along x-axis and [001] Ge uniaxially along y-axis are X_1, X_3 and X_2 respectively. Secondly, the top of the valence band increases more rapidly in the order of [001] direction along y-axis (compressive strain only), [110] and the [001] growth direction along x-axis for both signs of strain. However, under uniaxial tensile strain in [001] Ge along x-axis the top of the valence band has the

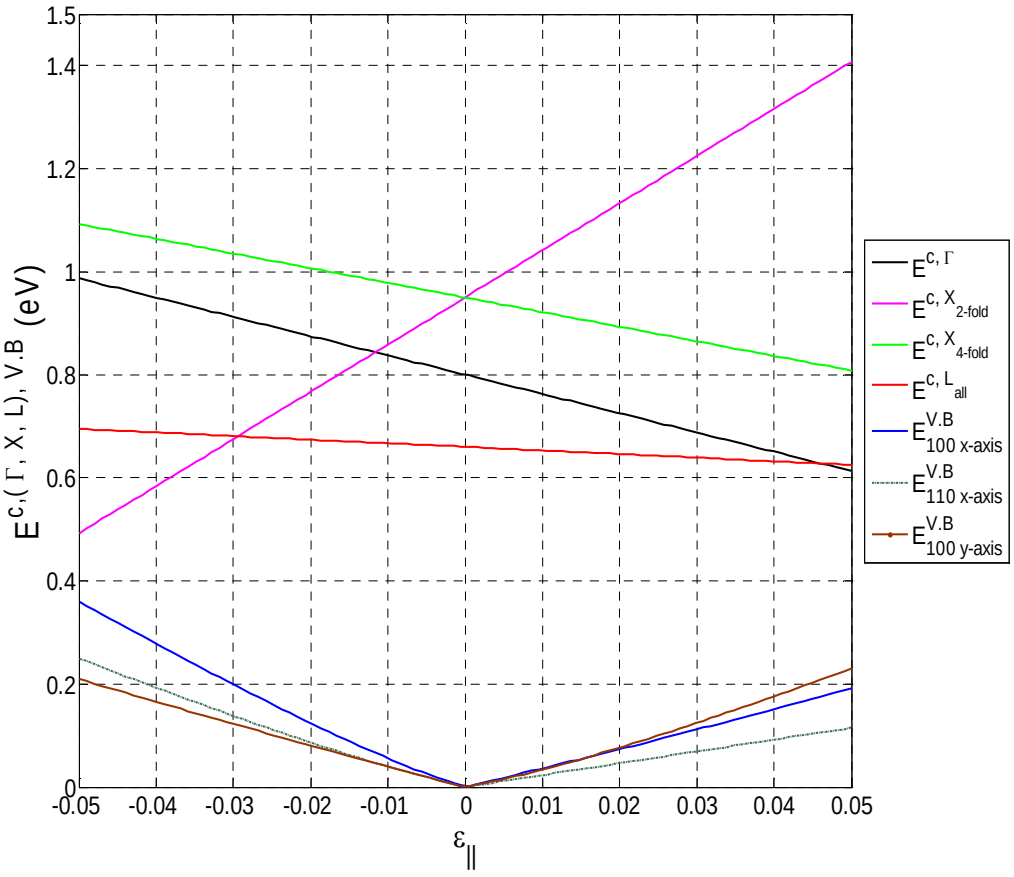

Figure A.2: The energy of the bottom of the conduction bands of k-valley (E^{c,k_i}) and the top of the valence band ($E^{\mathrm{V.B}}$) of uniaxial strain along x-axis for [001] and [110] and along y-axis of [001] bulk Ge.

highest increasing rate among the others. This is the only case that the change rate in the top of the valence band is larger for tensile than for the compressive strain.

In the third case of uniaxial strain along x-axis is for Ge grown on [111] direction, the conduction energy of all X-valleys increase with tensile and decrease with compressive strain, and the same is true for the fourfold L-valleys (L_3 and L_4) but with higher sensitivity to strain. The conduction energy of Γ-valley and the rest of L-valleys, which split into two twofold (L_1 and L_2) valleys, have opposite behaviour. Moreover, the sensitivity of L_1 to strain is larger than that of Γ and less than that of L_2. The valence band energy top increases with both signs of strain, but with a larger rate for compressive strain, fig. (A.3).

The conduction bands and valence band energies in uniaxial strain [001] Ge along y-axis is same as [001], and [110] Ge along y-axis with some differences mentioned before. For uniaxial strain along y-axis of [110] Ge the conduction band energy of fourfold X-valleys (X_1 and X_2) and fourfold L-valleys (L_3 and L_4) increase with tensile and decrease with compressive strain with almost similar rate. In contrast, the bottom energy of the twofold X-valleys (X_3) valleys, Γ-valley, and the fourfold L-valleys (L_1 and L_2), have the opposite behaviour, and the linear change is higher for the Γ-valley than for twofold X-valleys and less than for the fourfold L-valleys. The valence band top increase rate for compressive strain is 2.5 higher than the rate when tensile strain is applied, fig. (A.3).

For the [111] Ge uniaxially strained along y-axis, see fig. (A.4), the conduction band minimum energy of the fourfold L-valleys ($L_{3,4}$) increase and decrease significantly with tensile and compressive strain, respectively, while the fourfold X-valleys (X_1 and X_2) have the same behaviour but with less

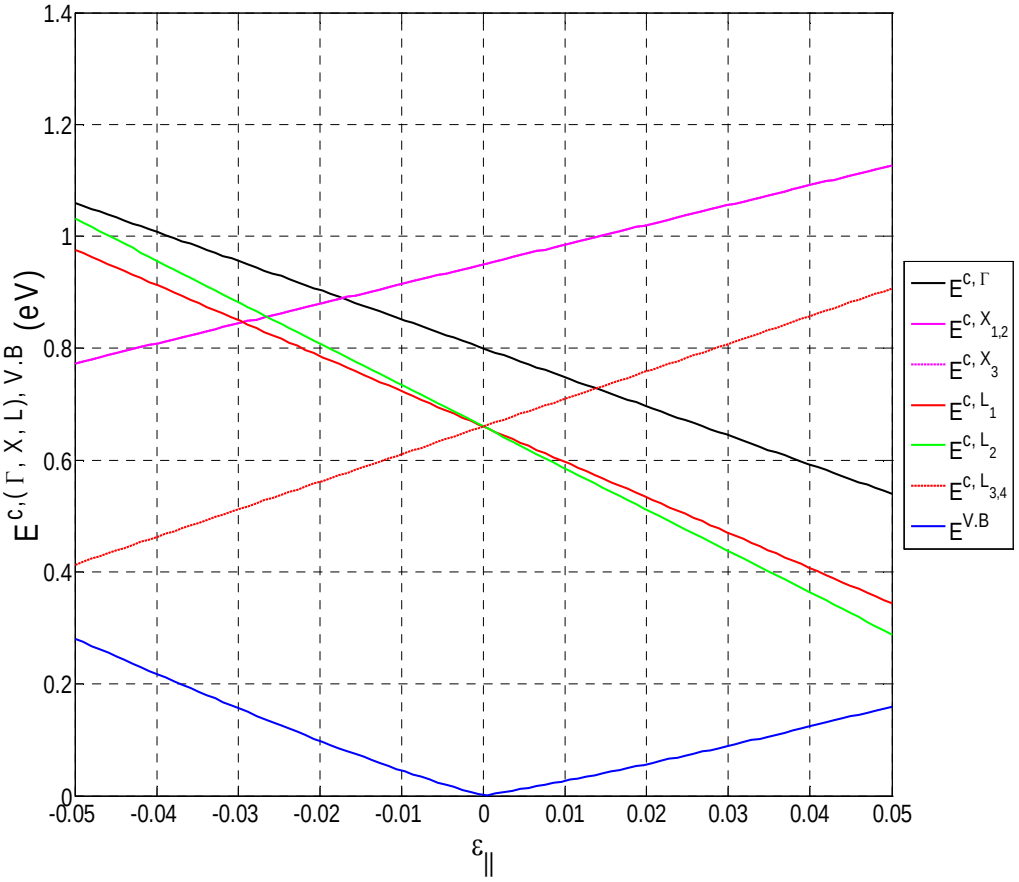

Figure A.3: The energy of the bottom of the conduction bands of k-valley (E^{c,k_i}) and the top of the valence band ($E^{\mathrm{V.B}}$) of uniaxial strain along x-axis for [001] and [110] and along y-axis of [001] bulk Ge.

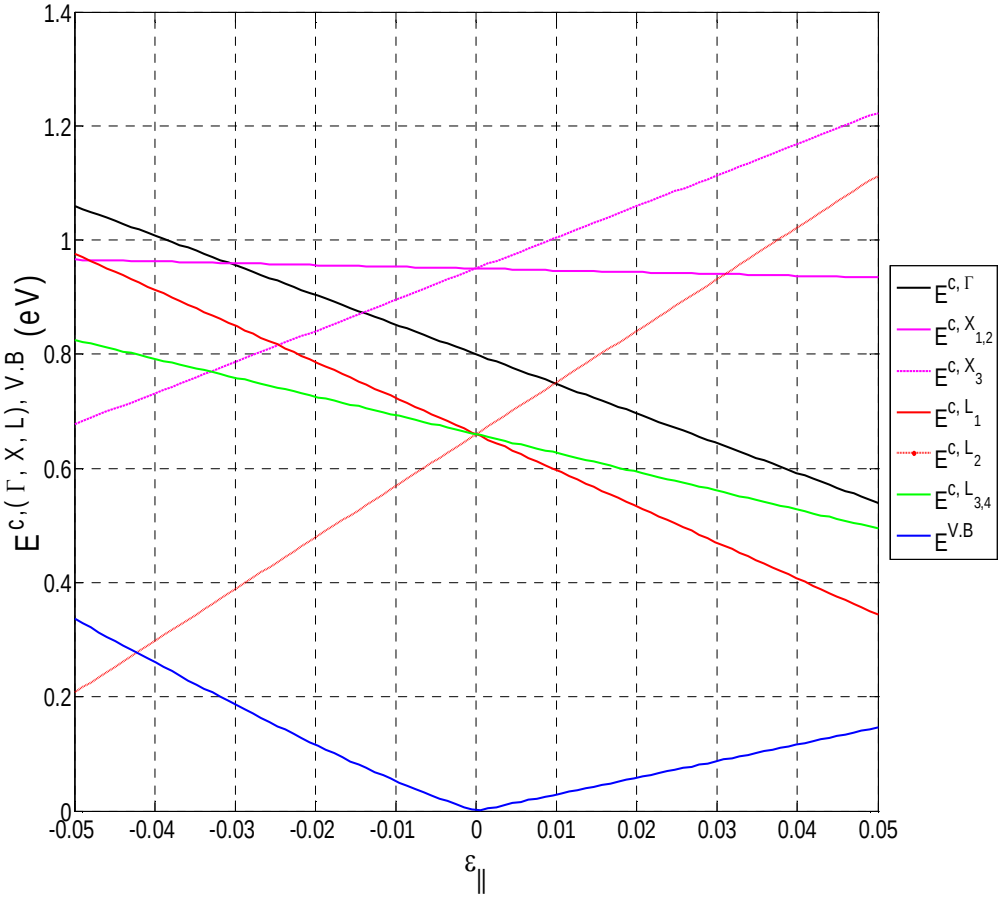

Figure A.4: The energy of the bottom of the conduction bands of k-valley (E^{c,k_i}) and the top of the valence band ($E^{V.B}$) of uniaxial strain along x-axis for [001] and [110] and along y-axis of [001] bulk Ge.

significant change. Conversely, the twofold X-valleys (X_3), Γ-valley, and the fourfold L-valleys (L_3 and L_4) have the opposite behaviour, and show more sensitive change in energy with the applied strain in that order. The maximum valence band energy increases with the two kinds of strain, and the rate for the compressive strain is double the rate in case of tensile strain.

B

EXPRESSION FOR THE MOMENTUM MATRIX ELEMENT USING THE 8-BAND $\mathbf{k}.\mathbf{p}$ METHOD

For an optical transition between two bands (*e.g.* a-band and b-band) the momentum matrix elements ($\langle \psi_a | \hat{p} | \psi_b \rangle$) can be found from the components of $\mathbf{k}.\mathbf{p}$ wavefunctions (eigenvectors) in them

$$\psi_a = \sum \left(\begin{bmatrix} a_1 & a_2 & a_3 & a_4 & a_5 & a_6 & a_7 & a_8 \end{bmatrix} \times \begin{bmatrix} u^{\Gamma_6}_{-\frac{1}{2}} \\ u^{\Gamma_6}_{+\frac{1}{2}} \\ u^{\Gamma_8}_{-\frac{3}{2}} \\ u^{\Gamma_8}_{-\frac{1}{2}} \\ u^{\Gamma_8}_{+\frac{1}{2}} \\ u^{\Gamma_8}_{+\frac{3}{2}} \\ u^{\Gamma_7}_{-\frac{1}{2}} \\ u^{\Gamma_7}_{+\frac{1}{2}} \end{bmatrix} \right) \tag{B.1}$$

where $a_1, a_2 ... a_8$ are the eigenvectors of 8×8 Hamiltonian for state a, and u are basis functions of the Hamiltonian as [18]:

$u^{\Gamma_6}_{-\frac{1}{2}} = |s\rangle \chi_{\downarrow}$,

$$u^{\Gamma_6}_{+\frac{1}{2}} = |s\rangle \chi_\uparrow,$$

$$u^{\Gamma_8}_{-\frac{2}{3}} = -\tfrac{i}{\sqrt{6}}\left(|x\rangle + i|y\rangle\right)\chi_\downarrow + i\sqrt{\tfrac{2}{3}}|z\rangle\chi_\uparrow,$$

$$u^{\Gamma_8}_{-\frac{1}{2}} = \tfrac{i}{\sqrt{2}}\left(|x\rangle + i|y\rangle\right)\chi_\uparrow,$$

$$u^{\Gamma_8}_{+\frac{1}{2}} = -\tfrac{i}{\sqrt{2}}\left(|x\rangle - i|y\rangle\right)\chi_\uparrow,$$

$$u^{\Gamma_8}_{+\frac{2}{3}} = \tfrac{i}{\sqrt{6}}\left(|x\rangle - i|y\rangle\right)\chi_\uparrow + i\sqrt{\tfrac{2}{3}}|z\rangle\chi_\downarrow,$$

$$u^{\Gamma_7}_{-\frac{1}{2}} = -\tfrac{i}{\sqrt{3}}\left(|x\rangle - i|y\rangle\right)\chi_\uparrow + \tfrac{i}{\sqrt{3}}|z\rangle\chi_\downarrow,$$

$$u^{\Gamma_7}_{-\frac{1}{2}} = -\tfrac{i}{\sqrt{3}}\left(|x\rangle + i|y\rangle\right)\chi_\downarrow - \tfrac{i}{\sqrt{3}}|z\rangle\chi_\uparrow.$$

where $\chi_\uparrow = \begin{bmatrix} 1 \\ 0 \end{bmatrix}$ and $\chi_\downarrow = \begin{bmatrix} 0 \\ 1 \end{bmatrix}$ are the eigenspinors, and

$$\chi_\uparrow\chi_\downarrow = \chi_\downarrow\chi_\uparrow = 0,$$

$$\chi_\uparrow\chi_\uparrow = \chi_\downarrow\chi_\downarrow = 0,$$

$$\langle s|p_{x,y,z}|x,y,z\rangle = +i\tfrac{m_0}{\hbar}P_0,$$

$$\langle x,y,z|p_{x,y,z}|s\rangle = \text{conj}\left(\langle s|p_{x,y,z}|x,y,z\rangle\right) = -\tfrac{m_0}{i\hbar}P_0,$$

$$\langle s|p_{x,y,z}|s\rangle = \langle s|p_{x,y,z}|(y,z),(x,z),(x,y)\rangle = \langle (y,z),(x,z),(x,y)|p_{x,y,z}|s\rangle = 0.$$

The following results apply:

$$\langle x|p_x|x\rangle = \langle y|p_y|y\rangle = \langle z|p_z|z\rangle = 0,$$

$$\langle x|p_{y,z}|x\rangle = \langle y|p_{x,z}|y\rangle = \langle z|p_{x,y}|z\rangle = 0,$$

$$\langle x|p_x|y,z\rangle = \langle y,z|p_x|x\rangle = \langle y|p_y|x,z\rangle = \langle x,z|p_y|y\rangle = \langle z|p_z|x,y\rangle = \langle x,y|p_z|z\rangle = 0.$$

See ref. [18] for more details.

The final full expression for matrix elements using 8×8 $\mathbf{k}.\mathbf{p}$ wavefunctions is

$$
\begin{aligned}
\langle \psi_a | \hat{p} | \psi_b \rangle \quad = \quad & P_0 \frac{m_0}{\hbar} \\
& \Bigg(- \quad \overrightarrow{i} \left[\frac{1}{\sqrt{2}} (a_1 b_5 - a_2 b_4 - a_4 b_2 + a_5 b_1) \right. \\
& \qquad + \frac{1}{\sqrt{3}} (a_1 b_8 + a_2 b_7 + a_7 b_2 + a_8 b_1) \\
& \qquad \left. + \frac{1}{\sqrt{6}} (a_1 b_3 + a_3 b_1 - a_2 b_6 - a_6 b_2) \right] \\
& - i \quad \overrightarrow{j} \left[\frac{1}{\sqrt{2}} (a_1 b_5 - a_2 b_4 - a_4 b_2 + a_5 b_1) \right. \\
& \qquad + \frac{1}{\sqrt{3}} (-a_1 b_8 + a_2 b_7 - a_7 b_2 + a_8 b_1) \\
& \qquad \left. + \frac{1}{\sqrt{6}} (-a_1 b_3 + a_3 b_1 - a_2 b_6 + a_6 b_2) \right] \\
& + \quad \overrightarrow{k} \Bigg[\sqrt{3} (a_1 b_7 + a_7 b_1) \\
& \qquad + \frac{1}{\sqrt{3}} (-a_2 b_8 - a_8 b_2) \\
& \qquad \left. + \sqrt{\frac{2}{3}} (a_2 b_3 + a_3 b_2 + a_1 b_6 + a_6 b_1) \right] \Bigg). \qquad \text{(B.2)}
\end{aligned}
$$

BIBLIOGRAPHY

[1] M. Levinshtein, M. S. Shur, and S. Rumyanstev, *Handbook series on semiconductor parameters, v. 1*. World Scientific, 1996.

[2] D. A. Fraser, *The physics of semiconductor devices*. Clarendon Press, 1986.

[3] B. G. Streetman and S. Banerjee, *Solid state electronic devices*. Prentice-Hall, 1972.

[4] J. R. Hook and H. E. Hall, *Solid State Physics*. John Wiley and Sons, 1991.

[5] C. Kittel, *Introduction to solid state physics*. Wiley New York, 1986.

[6] N. Fraj, I. Saïdi, S. Ben Radhia, and K. Boujdaria, "Band parameters of AlAs, Ge and Si in the 34-band k sdot p model," *Semiconductor Science and Technology*, vol. 23, no. 8, p. 085006, Aug. 2008.

[7] W. R. Runyan, *Silicon semiconductor technology*. McGraw-Hill New York, 1965, vol. 203.

[8] J. Liu, X. Sun, D. Pan, X. Wang, L. Kimerling, and T. L. Koch, "Tensile-strained, n-type Ge as a gain medium for monolithic laser integration on Si," *Optics Express*, vol. 15, no. 18, pp. 11 272–11 277, 2007.

[9] O. Aldaghri, Z. Ikonic, and R. W. Kelsall, "The effects of tensile-strain conditions on doping density requirements for Ge-based injection lasers," in *8th IEEE International Conference on Group IV Photonics*. IEEE, 2011, pp. 151–153.

[10] ——, "Optimum strain configurations for carrier injection in near infrared Ge lasers," *Journal of Applied Physics*, vol. 111, pp. 053 106–053 106–5, 2012.

[11] S. L. Chuang, *Physics of optoelectronic devices*. Wiley New York, 1995.

[12] J. Liu, R. Camacho-Aguilera, J. T. Bessette, X. Sun, X. Wang, Y. Cai, L. C. Kimerling, and J. Michel, "Ge-on-Si optoelectronics," *Thin Solid Films*, vol. 520, no. 8, pp. 3354–3360, 2012.

[13] C.-Y. Tsai, C.-Y. Tsai, C.-H. Chen, T.-L. Sung, T.-Y. Wu, and F.-P. Shih, "Theoretical model for intravalley and intervalley free-carrier absorption in semiconductor lasers: beyond the classical Drude model," *IEEE Journal of Quantum Electronics*, vol. 34, no. 3, pp. 552–559, 1998.

[14] C. Y. Tsai, "Theoretical model for the optical gain coefficient of indirect-band-gap semiconductors," *Journal of Applied Physics*, vol. 99, p. 053506, 2006.

[15] M. Grundmann, *The physics of semiconductors*. Springer, 2006.

[16] I. Balslev, "Influence of uniaxial stress on the indirect absorption edge in silicon and germanium," *Physical Review*, vol. 143, no. 2, p. 636, 1966.

[17] H. J. McSkimin and P. Andreatch Jr, "Elastic moduli of silicon vs hydrostatic pressure at 25.0 C and- 195.8 C," *Journal of Applied Physics*, vol. 35, no. 7, pp. 2161–2165, 1964.

[18] T. B. Bahder, "Eight-band k.p model of strained zinc-blende crystals," *Physical Review B*, vol. 41, no. 17, pp. 11 992–12 001, 1990.

[19] C. Y.-P. Chao and S. L. Chuang, "Spin-orbit-coupling effects on the valence-band structure of strained semiconductor quantum wells," *Physical Review B*, vol. 46, no. 7, pp. 4110–4122, 1992.

[20] M. Yang, J. C. Sturm, and J. Prevost, "Calculation of band alignments and quantum confinement effects in zero- and one-dimensional pseudomorphic structures," *Physical Review B*, vol. 56, p. 1973, 1997.

[21] G. Dresselhaus, A. F. Kip, and C. Kittel, "Cyclotron resonance of electrons and holes in silicon and germanium crystals," *Physical Review*, vol. 98, no. 2, pp. 384–368, 1955.

[22] M. M. Rieger and P. Vogl, "Electronic-band parameters in strained Si_{1-x} Ge_x alloys on Si_{1-y} Ge_y substrates," *Physical Review B*, vol. 48, no. 19, pp. 14 276–14 287, 1993.

[23] F. Stern and W. E. Howard, "Properties of semiconductor surface inversion layers in the electric quantum limit," *Physical Review*, vol. 163, no. 3, p. 816, 1967.

[24] T. Ando, A. B. Fowler, and F. Stern, "Electronic properties of two-dimensional systems," *Reviews of Modern Physics*, vol. 54, no. 2, pp. 437–672, 1982.

[25] J. Liu, X. Sun, L. Kimerling, and J. Michel, "Direct-gap optical gain of Ge on Si at room temperature," *Optics Letters*, vol. 34, no. 11, Jun. 2009.

[26] X. Sun, J. Liu, L. Kimerling, and J. Michel, "Direct gap photoluminescence of *n*-type tensile-strained Ge-on-Si," *Applied Physics Letters*, vol. 95, p. 011911, 2009.

[27] D. Ahn, C.-y. Hong, J. Liu, W. Giziewicz, M. Beals, L. C. Kimerling, J. Michel, J. Chen, and F. X. K. a. rtner, "High performance, waveguide integrated Ge photodetectors," *Opt. Express*, vol. 15, no. 7, pp. 3916–3921, Apr. 2007.

[28] M. Morse, O. Dosunmu, G. Sarid, and Y. Chetrit, "Performance of Ge-on-Si p-i-n Photodetectors for Standard Receiver Modules," *Photonics Technology Letters, IEEE*, vol. 18, no. 23, pp. 2442–2444, Dec. 2006.

[29] M. E. Groenert, C. W. Leitz, A. J. Pitera, V. Yang, H. Lee, R. J. Ram, and E. A. Fitzgerald, "Monolithic integration of room-temperature cw GaAs/AlGaAs lasers on Si substrates via relaxed graded GeSi buffer layers," *Journal of Applied Physics*, vol. 93, no. 1, pp. 362–367, Jan. 2003.

[30] C. K. Maiti, N. B. Chakrabarti, and S. K. Ray, *Strained silicon heterostructures: materials and devices*. Institution of Electrical Engineers, 2001.

[31] Q. Xu, B. Schmidt, S. Pradhan, and M. Lipson, "Micrometre-scale silicon electro-optic modulator," *Letters to Nature*, vol. 435, no. 7040, pp. 325–327, May 2005.

[32] A. Liu, R. Jones, L. Liao, D. Samara-Rubio, D. Rubin, O. Cohen, R. Nicolaescu, and M. Paniccia, "A high-speed silicon optical modulator based on a metal-oxide-semiconductor capacitor," *Letters to Nature*, vol. 427, no. 6975, pp. 615–618, Feb. 2004.

[33] M. W. Geis, S. J. Spector, M. E. Grein, R. T. Schulein, J. U. Yoon, D. M. Lennon, S. Deneault, F. Gan, F. X. Kaertner, and T. M. Lyszczarz, "CMOS-Compatible All-Si High-Speed Waveguide Photodiodes With High Responsivity in Near-Infrared Communication Band," *Photonics Technology Letters, IEEE*, vol. 19, no. 3, pp. 152–154, Feb. 2007.

[34] M. W. Geis, S. J. Spector, M. E. Grein, J. U. Yoon, D. M. Lennon, and T. M. Lyszczarz, "Silicon waveguide infrared photodiodes with >35 GHz bandwidth and phototransistors with 50 AW^{-1} response," *Opt. Express*, vol. 17, no. 7, pp. 5193–5204, Mar. 2009.

[35] A. W. Fang, H. Park, O. Cohen, R. Jones, M. J. Paniccia, and J. E. Bowers, "Electrically pumped hybrid AlGaInAs-silicon evanescent laser," *Opt. Express*, vol. 14, no. 20, pp. 9203–9210, Oct. 2006.

[36] D. J. Paul, "Silicon-Germanium Strained Layer Materials in Microelectronics," *Advanced Materials*, vol. 11, no. 3, pp. 191–204, 1999.

[37] L. Pavesi, L. Dal Negro, C. Mazzoleni, G. Franzo, and F. Priolo, "Optical gain in silicon nanocrystals," *Letters to Nature*, vol. 408, no. 6811, pp. 440–444, 2000.

[38] B. Garrido, O. GonzÁlez, S. Cheylan, M. López, A. PÉrez-Rodríguez, C. García, P. Pellegrino, R. Ferrer, J. R. Morante, J. de la Torre, A. Souifi, A. Poncet, C. Busseret, M. Lemiti, G. Bremond, and G. Guillot, "Optical And Electrical Characteristics Of Leds Fabricated From Si-Nanocrystals Embedded In SiO_2," in *Towards the First Silicon Laser*. Dordrecht: Springer Netherlands, Jan. 2003, pp. 45–54.

[39] O. Boyraz and B. Jalali, "Demonstration of a silicon Raman laser," *Opt. Express*, vol. 12, no. 21, pp. 5269–5273, Oct. 2004.

[40] H. Rong, A. Liu, R. Jones, O. Cohen, D. Hak, R. Nicolaescu, A. Fang, and M. Paniccia, "An all-silicon Raman laser," *Letters to Nature*, vol. 433, no. 7023, pp. 292–294, 2005.

[41] T. K. Liang and H. K. Tsang, "Role of free carriers from two-photon absorption in Raman amplification in silicon-on-insulator waveguides," *Applied Physics Letters*, vol. 84, no. 1, p. 2745, Apr. 2004.

[42] D. J. Paul, "Si/SiGe heterostructures: from material and physics to devices and circuits," *Semiconductor Science and Technology*, vol. 19, pp. R75–R108, 2004.

[43] E. Gatti, F. Isa, D. Chrastina, E. M. Gubler, F. Pezzoli, E. Grilli, and G. Isella, "Ge/SiGe quantum wells on Si (111): Growth, structural, and optical properties," *Journal of Applied Physics*, vol. 116, no. 4, p. 043518, 2014.

[44] Y. Ishikawa, K. Wada, D. D. Cannon, J. Liu, H.-C. Luan, and L. Kimerling, "Strain-induced band gap shrinkage in Ge grown on Si substrate," *Applied Physics Letters*, vol. 82, no. 13, pp. 2044–2046, Mar. 2003.

[45] C. G. Van de Walle, "Band lineups and deformation potentials in the model-solid theory," *Physical Review B*, vol. 39, no. 3, pp. 1871–1883, 1989.

[46] P. H. Lim, S. Park, Y. Ishikawa, and K. Wada, "Enhanced direct bandgap emission in germanium by micromechanical strain engineering," *Optics Express*, vol. 17, no. 18, pp. 16 358–16 365, Aug. 2009.

[47] T. H. Cheng, K. L. Peng, C. Y. Ko, C. Y. Chen, H. S. Lan, Y. R. Wu, C. W. Liu, and H. H. Tseng, "Strain-enhanced photoluminescence from Ge direct transition," *Applied Physics Letters*, vol. 96, no. 21, p. 211108, 2010.

[48] M. V. Fischetti and S. E. Laux, "Band structure, deformation potentials, and carrier mobility in strained Si, Ge, and SiGe alloys," *Journal of Applied Physics*, vol. 80, 1996.

[49] M. El Kurdi, T. P. Ngo, X. Checoury, S. Sauvage, G. Fishman, T. Kociniewski, D. Debarre, J. Boulmer, P. Boucaud, J. F. Damlencourt, O. Kermarrec, D. Bensahel, R. Jakomin, and I. Sagnes, "Tensile-strain and *n*-type doping of germanium-on-insulator : Towards a Ge laser," in *6th IEEE International Conference on Group IV Photonics*. IEEE, 2009, pp. 259–261.

[50] C. Boztug, F. Chen, J. R. Sanchez-Perez, F. F. Sudradjat, D. M. Paskiewicz, R. B. Jacobson, M. G. Lagally, and R. Paiella, "Direct-bandgap Germanium active layers pumped above transparency based on tensily strained nanomembranes," in *Optical society of America*, 2011.

[51] K. Uchida, R. Zednik, L. Ching-Huang, H. Jagannathan, J. McVittie, McIntyre, P. C., and Y. Nishi, "Experimental study of biaxial and uniaxial strain effects on carrier mobility in bulk and ultrathin-body SOI MOSFETs," in *IEEE International Electron Devices Meeting (IEDM) Technical Digest.*, 13 2004, pp. 229–232.

[52] K. Sawano, Y. Hoshi, A. Yamada, and Y. Hiraoka, "Introduction of Uniaxial Strain into Si/Ge Heterostructures by Selective Ion Implantation," *Applied Physics Express*, vol. 1, p. 121404, 2008.

[53] H.-Y. Yu, D. Kim, S. Ren, M. Kobayashi, D. A. B. Miller, Y. Nishi, and K. C. Saraswat, "Effect of uniaxial-strain on Ge p-i-n photodiodes integrated on Si," *Applied Physics Letters*, vol. 95, no. 16, pp. 161 106–161 103, 2009.

[54] A. L. Ruoff, "On the ultimate yield strength of solids," *Journal of Applied Physics*, vol. 49, pp. 197–200, 1978.

[55] D. Roundy and M. L. Cohen, "Ideal strength of diamond, Si, and Ge," *Physical Review B*, vol. 64, no. 21, p. 212103, 2001.

[56] G. He and H. A. Atwater, "Interband transitions in Sn_x Ge_{1-x} alloys," *Physical Review Letters*, pp. 1937–1940, 1997.

[57] M. J. Süess, R. Geiger, R. A. Minamisawa, G. Schiefler, J. Frigerio, D. Chrastina, G. Isella, R. Spolenak, J. Faist, and H. Sigg, "Analysis of enhanced light emission from highly strained germanium microbridges," *Nature Photonics*, vol. 7, no. 6, pp. 466–472, 2013.

[58] M. de Kersauson, M. El Kurdi, S. David, X. Checoury, G. Fishman, S. Sauvage, R. Jakomin, G. Beaudoin, I. Sagnes, and P. Boucaud, "Optical gain in single tensile-strained germanium photonic wire," *Optics Express*, vol. 19, no. 19, pp. 17 925–17 934, Sep. 2011.

[59] D. Nam, A. Roy, K. Huang, M. Brongersma, and K. Saraswat, "Strained Germanium Membrane using Thin Film Stressor for High Efficiency Laser," in *CLEO:2011 - Laser Applications to Photonic Applications*. Optical Society of America, 2011, p. JTuI85.

[60] D. Nam, D. Sukhdeo, A. Roy, K. Balram, S.-L. Cheng, K. C.-Y. Huang, Z. Yuan, M. Brongersma, Y. Nishi, D. Miller, and K. Saraswat, "Strained germanium thin film membrane on silicon substrate for

optoelectronics," *Opt. Express*, vol. 19, no. 27, pp. 25 866–25 872, Dec. 2011.

[61] A. Ghrib, M. El Kurdi, M. de Kersauson, M. Prost, S. Sauvage, X. Checoury, G. Beaudoin, I. Sagnes, and P. Boucaud, "Tensile-strained germanium microdisks," *Applied Physics Letters*, vol. 102, no. 22, p. 221112, 2013.

[62] A. Ghrib, M. El Kurdi, M. Prost, S. Sauvage, G. Baudoin, L. Largeau, M. Chaigneau, R. Ossikovski, I. Sagnes, and P. Boucaud, "High Tensile Strain Transfer into Germanium Microdisks UsingAll-Around Strained Si3N4," in *2014 IEEE 11th International Conference on Group IV Photonics (GFP)*, 2014.

[63] X. Sun, J. Liu, L. Kimerling, and J. Michel, "Room-temperature direct bandgap electroluminesence from Ge-on-Si light-emitting diodes," *Optics Letters*, vol. 34, no. 8, 2009.

[64] X. Sun, J. Liu, L. C. Kimerling, and J. Michel, "A Ge-on-Si laser for electronic-photonic integration," in *Conference on Lasers and Electro-Optics*. Optical Society of America, 2009, p. CTuY1.

[65] Y. Hoshina, K. Iwasaki, A. Yamada, and M. Konagai, "First-Principles Analysis of Indirect-to-Direct Band Gap Transition of Ge under Tensile Strain," *Japanese Journal of Applied Physics*, vol. 48, no. 4, p. 04C125, 2009.

[66] X. Sun, L. Jifeng, L. Kimerling, and J. Michel, "Toward a Germanium Laser for Integrated Silicon Photonics," *IEEE JOURNAL OF SELECTED TOPICS IN QUANTUM ELECTRONICS*, vol. 16, pp. 124–131, 2010.

[67] J. Liu, X. Sun, R. Camacho-Aguilera, and L. Kimerling, "Ge-on-Si laser operating at room temperature," *Optics Letters*, vol. 35, no. 5, pp. 679–681, 2010.

[68] H. S. Lan, S. T. Chan, T. H. Cheng, and C. Y. Chen, "Biaxial tensile strain effects on photoluminescence of different orientated Ge wafers," *Applied Physics Letters*, 2011.

[69] M. El Kurdi, T. Kociniewski, T. P. Ngo, J. Boulmer, D. Debarre, P. Boucaud, J. F. Damlencourt, O. Kermarrec, and D. Bensahel, "Enhanced photoluminescence of heavily n-doped germanium," *Applied Physics Letters*, vol. 94, no. 19, pp. 191 107–191 107–3, May 2009.

[70] T. H. Cheng, C. Y. Ko, C. Y. Chen, K. L. Peng, G. L. Luo, C. W. Liu, and H. H. Tseng, "Competitiveness between direct and indirect radiative transitions of Ge," *Applied Physics Letters*, vol. 96, no. 9, p. 091105, 2010.

[71] Y. Huo, H. Lin, Y. Rong, M. Makarova, M. Li, R. Chen, T. I. Kamins, J. Vuckovic, and J. S. Harris, "Efficient luminescence in highly tensile-strained germanium," in *6th IEEE International Conference on Group IV Photonics*. IEEE, 2009, pp. 265–267.

[72] L. Carroll, P. Friedli, S. Neuenschwander, H. Sigg, S. Cecchi, F. Isa, D. Chrastina, G. Isella, Y. Fedoryshyn, and J. e. o. Faist, "Direct-Gap Gain and Optical Absorption in Germanium Correlated to the Density of Photoexcited Carriers, Doping, and Strain," *Physical Review Letters*, vol. 109, p. 057402, Aug. 2012.

[73] R. Geiger, J. Frigerio, M. J. Süess, D. Chrastina, G. Isella, R. Spolenak, J. Faist, and H. Sigg, "Excess carrier lifetimes in Ge layers on Si," *Applied Physics Letters*, vol. 104, no. 6, p. 062106, 2014.

[74] S.-L. Cheng, J. Lu, G. Shambat, H.-Y. Yu, K. Saraswat, J. Vuckovic, and Y. Nishi, "Room temperature 1.6 μm electroluminescence from Ge light emitting diode on Si substrate," *Opt. Express*, vol. 17, no. 12, pp. 10 019–10 024, Jun. 2009.

[75] M. H. Liao, M. J. Chen, T. C. Chen, and P. L. Wang, "Electroluminescence from metal/oxide/strained-Si tunneling diodes," *Applied Physics Letters*, vol. 86, p. 223502, 2005.

[76] M. Oehme, M. Gollhofer, D. Widmann, M. Schmid, M. Kaschel, E. Kasper, and J. Schulze, "Direct bandgap narrowing in Ge LED's on Si substrates," *Optics express*, vol. 21, no. 2, pp. 2206–2211, 2013.

[77] J. Liu, X. Sun, R. Camacho-Aguilera, Y. Cai, L. Kimerling, and J. Michel, "Optical gain and lasing from band-engineered Ge-on-Si at room temperature," in *15th OptoeElectronics and Communications Conference*. IEEE, 2010, pp. 520–521.

[78] T. H. Cheng, P. S. Kuo, C. T. Lee, M. Liao, T. A. Hung, and C. W. Liu, "Electrically pumped Ge Laser at room temperature," *IEEE International Electron Devices Meeting*, pp. 659–662, 2007.

[79] J. Michel, R. E. Camacho-Aguilera, Y. Cai, N. Patel, J. T. Bessette, M. Romagnoli, R. Dutt, and L. Kimerling, "An Electrically Pumped Ge-on-Si Laser," *National Fiber Optic Engineers Conference (2012), paper PDP5A.6*, p. PDP5A.6, Mar. 2012.

[80] R. Camacho-Aguilera, Z. Han, Y. Cai, L. C. Kimerling, and J. Michel, "Direct band gap narrowing in highly doped Ge," *Applied Physics Letters*, vol. 102, no. 15, pp. 152 106–152 106–3, Apr. 2013.

[81] Y. Cai, Z. Han, X. Wang, R. E. Camacho-Aguilera, L. C. Kimerling, J. Michel, and J. Liu, "Analysis of Threshold Current Behavior for Bulk and Quantum-Well Germanium Laser Structures," *Selected Topics in Quantum Electronics, IEEE Journal of*, vol. 19, no. 4, pp. 1 901 009–1 901 009, 2013.

[82] S. M. Sze and K. K. Ng, *Physics of semiconductor devices*. Wiley-Blackwell, 2007.

[83] J. R. Chelikowsky and M. L. Cohen, "Nonlocal pseudopotential calculations for the electronic structure of eleven diamond and zinc-blende semiconductors," *Physical Review B*, vol. 14, no. 2, pp. 556–582, 1976.

[84] S. L. Chuang, *Physics of photonic devices*. John Wiley & Sons, 2012, vol. 80.

[85] M. Bescond, N. Cavassilas, and M. Lannoo, "Effective-mass approach for n-type semiconductor nanowire MOSFETs arbitrarily oriented," *Nanotechnology*, vol. 18, no. 25, p. 255201, Jun. 2007.

[86] L. C. L. Y. Voon and M. Willatzen, *The kp method: electronic properties of semiconductors*. Springer, 2009.

[87] N. W. Ashcroft and N. D. Mermin, *Solid State Physics*. Holt, Rinehart and Winston, New York, 1976.

[88] http://www.iue.tuwien.ac.at/phd/dhar/node17.html.

[89] S. Smirnov and H. Kosina, "Monte Carlo modeling of the electron mobility in strained $Si_{1-x}Ge_x$ layers on arbitrarily oriented $Si_{1-y}Ge_y$ substrates," *Solid-State Electronics*, vol. 48, no. 8, pp. 1325–1335, 2004.

[90] P. Harrison, *Quantum wells, wires, and dots: theoretical and computational physics of semiconductor nanostructures*. Wiley London, 2005.

[91] C. G. Van de Walle and R. M. Martin, "Theoretical calculations of heterojunction discontinuities in the Si/Ge system," *Physical Review B*, vol. 34, no. 8, p. 5621, 1986.

[92] P. Y. Yu and M. Cardona, *Fundamentals of Semiconductors*, ser. Graduate Texts in Physics. Berlin, Heidelberg: Springer, 2010.

[93] Y. Yin, D. Yan, F. Pollak, M. Hybertsen, J. Vandenberg, and J. Bean, "Temperature dependence of the fundamental direct transitions of bulk Ge and two Ge/SiGe multiple-quantum-well structures," *Physical Review B*, vol. 52, pp. 8951–8958, Sep. 1995.

[94] R. K. Schaevitz, D. S. Ly-Gagnon, J. E. Roth, E. H. Edwards, and D. A. B. Miller, "Indirect absorption in germanium quantum wells," *AIP Advances*, vol. 1, no. 3, p. 2164, 2011.

[95] K. Seeger, *Semiconductor physics: an introduction*. Springer, 2004.

[96] B. K. Ridley, *Quantum Processes in Semiconductors*. Oxford University Press, 2013.

[97] X. Wang, H. Li, R. Camacho-Aguilera, Y. Cai, L. C. Kimerling, J. Michel, and J. Liu, "Infrared absorption of *n*-type tensile-strained Ge-on-Si," *Optics Letters*, vol. 38, no. 5, pp. 652–654, Mar. 2013.

[98] J. Taylor and V. Tolstikhin, "Intervalence band absorption in InP and related materials for optoelectronic device modeling," *Journal of Applied Physics*, vol. 87, no. 3, pp. 1054–1059, Feb. 2000.

[99] W. H. Press, S. A. Teukolsky, W. T. Vetterling, and B. P. Flannery, *Numerical recipes in C*. Citeseer, 1996, vol. 2.

[100] J. McDougall and E. C. Stoner, "The computation of Fermi-Dirac functions," *Philosophical Transactions of the Royal Society of London. Series A, Mathematical and Physical Sciences*, vol. 237, no. 773, pp. 67–104, 1938.

[101] J. S. Blakemore, "Approximations for Fermi-Dirac integrals, especially the function F12 (η) used to describe electron density in a semiconductor," *Solid-State Electronics*, vol. 25, no. 11, pp. 1067–1076, 1982.

[102] P. Van Halen and D. L. Pulfrey, "Accurate, short series approximations to Fermi–Dirac integrals of order- 1/2, 1/2, 1, 3/2, 2, 5/2, 3, and 7/2," *Journal of Applied Physics*, vol. 57, no. 12, pp. 5271–5274, 1985.

[103] C. Jacoboni and L. Reggiani, "The Monte Carlo method for the solution of charge transport in semiconductors with applications to covalent materials," *Reviews of Modern Physics*, vol. 55, no. 3, pp. 645–705, Jul. 1983.

[104] M. V. Fischetti, "Monte Carlo simulation of transport in technologically significant semiconductors of the diamond and zinc-blende structures. I. Homogeneous transport," *Electron Devices, IEEE Transactions on*, vol. 38, no. 3, pp. 634–649, 1991.

[105] H. Y. Fan, "Chapter 9 Effects of Free Carriers on the Optical Properties," R. K. Willardson and A. C. Beer, Eds. Elsevier, 1967, pp. 405–419.

[106] B. K. Ridley, *Electrons and Phonons in Semiconductor Multilayers*. Cambridge University Press, Apr. 2009.

[107] R. E. Camacho-Aguilera, Y. Cai, N. Patel, J. T. Bessette, M. Romagnoli, L. C. Kimerling, and J. Michel, "An electrically pumped germanium laser," *Opt. Express*, vol. 20, no. 10, pp. 11 316–11 320, May 2012.

[108] D. Y. Fu, R. Zhang, B. G. Wang, B. Liu, Z. L. Xie, X. Q. Xiu, H. Lu, Y. D. Zheng, and G. Edwards, "Biaxial and uniaxial strain effects on the ultraviolet emission efficiencies of $Al_xGa_{1-x}N$ films with different Al concentrations," *Journal of Applied Physics*, vol. 108, pp. 103 107–103 107–5, Nov. 2010.